Non-Intrusive Nonlinear Reduced-Order Model Identification and Substructuring of Geometrically Nonlinear Structures

Jordan Seawright

A dissertation
submitted in partial fulfillment of the
requirements for the degree of

Doctor of Philosophy

University of Washington

2023

Reading Committee:
Richard Wiebe, Chair
Ricardo Perez, Chair
Peter Mackenzie-Helnwein

Program Authorized to Offer Degree:
Civil Engineering

©Copyright 2023
Jordan Seawright

University of Washington

Abstract

Non-Intrusive Nonlinear Reduced-Order Model Identification and Substructuring of Geometrically Nonlinear Structures

Jordan Seawright

Chair of the Supervisory Committee:
Richard Wiebe
Department of Civil and Environmental Engineering

A reduction in the number of Degrees Of Freedom (DOFs) of a nonlinear structural model can significantly decrease the computational time of dynamic analyses, especially in problems where long analyses are required. A Reduced-Order Model (ROM) of a structural system can be generated using some combination of dimensionality reduction techniques, such as substitution of a modal basis or static condensation of membrane DOFs. Perhaps the most common and widespread framework for developing low-order models of continuous systems is the Ritz method in conjunction with a smooth modal basis. The Ritz method requires access to the closed form governing differential equations and is difficult to implement for problems with complex boundary conditions. In recent decades, an alternative framework that instead constructs a low-order model from an existing Finite Element Model (FEM) has been developed. Such models are typically known as NonLinear Reduced-Order Models (NLROMs). Such NLROMs can be used to handle complex boundary conditions so long as the FEM can do the same, and they allow the analyst to start from an existing finite element package as opposed to directly working with the governing differential equations. The form of the NLROM restoring force function is assumed by the analyst prior to identifying the model, and the parameters of the function are identified to achieve a high-quality fit to the FEM load-displacement data.

This research aims in part to use Ritz method approximations to analytically predict the model parameters of identified NLROMs. Specifically, the shallow von Kármán beam equation is used as a basis for the study of geometrically nonlinear beams. An approximate form of the statically Condensed Von Kármán (CVK) beam equation is attained using the Ritz method, and the equivalence between the CVK coefficients and the NLROM coefficients is shown. In another study, the matrix and vector parameters of the CVK beam equation are treated as parameters to be identified from an FEM rather than being derived analytically using the properties of the structure. A simplified identification procedure is proposed which requires only two static solutions of an FEM, regardless of the number of modes included in the reduced-order basis. An arc-length continuation algorithm is used to predict the static load-displacement response of the models studied and to assess the accuracy of the ROMs. In the case of initially straight, post-buckled beams, the proposed identification procedure is shown to generate a model that generally outperforms a corresponding NLROM identified using conventional parameter identification techniques.

Identifying NLROMs from beams with large initial curvature has frequently been accompanied by numerical stability issues. This work implements a displacement-based implicit condensation approach to the reduced-order model identification of curved beams that allows for the precise specification of transverse displacements in mid- and post-snap-through configurations. The configurations used to generate training data are extracted from points of interest on the static equilibrium path, which is determined using an arc-length method. The error in the reduced-order model approximation is characterized and plotted versus the arc-length step, and the improvements in targeted areas of the response are demonstrated. It is determined that specifying additional training data around mid- and post-snap-through configurations significantly improves the accuracy of the large-deformation response and model stability. It is shown that the simplified restoring force template provides comparable results to the full restoring force in a form with significantly fewer parameters.

As a third application, a substructuring approach is used to reduce the order of a plane stress FEM of a deep planar beam. The model is divided into two substructures—one modeled with a full-order FEM and one modeled with an NLROM. The coupling between the NLROM substructure and the FEM substructure is accomplished using interface modes which represent the characteristic response of the structure at the interface. Directly coupling the NLROM and FEM substructures results in elevated errors in the stresses at the interface. A transition zone is added between the NLROM and FEM substructures, whereby certain DOFs that were expanded as a function of the NLROM DOFs are instead modeled as full-order finite element DOFs. Using a transition zone of approximately one beam depth proved to be effective in reducing the stress errors to acceptable levels. A multi-layer beam was successfully modeled using an identified interface mode that reflected the thickness-varying material properties of the beam.

TABLE OF CONTENTS

LIST OF FIGURES

LIST OF TABLES

ACKNOWLEDGMENTS

First, I would like to thank my advisor, Professor Richard Wiebe, for his skillful mentorship throughout my time at the University of Washington. Being of like mind, we took numerous creative detours during our research, and his wisdom in "zooming out" to view the whole picture taught me to focus that creative energy into a work product. I am grateful for our discussions in and out of the office over the past four years and for the friendship we have developed.

I would also like to thank Dr. Ricardo Perez for his time and expertise during this process. His guidance in the area of reduced-order modeling has been invaluable.

I want to express my thanks to Professor Peter Mackenzie-Helnwein for offering his wisdom and experience. His gift for teaching has led to some of the the most formative and surprising entrees into mechanics of my academic career. I am immensely grateful for the time he has dedicated my growth as an engineer.

Thank you to my Graduate School Representative, Professor Ed Habtour, for serving on my committee and bringing his skillset to the discussion. Finally, I want to thank my fellow PhD students, Tatsu Sweet and Bill Galik, for helping to create a critical mass of interest in some of the "less traveled" subjects in mechanics.

It is the glory of God to conceal a matter,
But the glory of kings is to search out a matter.
-Proverbs 25:2 (NKJV)

DEDICATION

to my wife, Noelle

Chapter 1

INTRODUCTION

1.1 Background

Recent developments in aerospace design have emphasized the need for fast structural simulation tools. A pressing example is the prediction of the nonlinear dynamics and life-cycle of thermally-buckled skin panels on high-speed aircraft, which has gathered significant interest [6, 44]. Simulations of fatigue life-cycle for responses with snap-through require long simulations of a nonlinear process, leading to computationally intensive simulations [38]. Thus, there is a need for models with fewer Degrees-Of-Freedom (DOFs) that accurately predict the important aspects of the response.

Numerous methods for reducing model dimension of continuous dynamical systems have been developed. Within the study of slender beams and shells, there are two especially common approaches which will be the focus of this thesis. The first, and older of the two, is the Ritz family of methods, which includes the Ritz-Galerkin method. Ritz-Galerkin approximations have been applied to large-deformation beam and plate theories, such as the the von Kármán beam and plate theories, using smooth interpolation functions that each span the entire physical domain of the problem [22,23,45]. This approach is limited to simpler problems where explicit definitions of the governing differential equations and boundary conditions are available [25]. More recently, a different approach has been taken to construct a NonLinear Reduced-Order Model (NLROM) from an existing Finite Element Model (FEM). An NLROM uses a discrete modal basis, which often consists of a subset of the vibration mode shapes of the associated FEM. The form of the restoring force function is assumed, and the parameters of the restoring force function are identified using load displacement data from test cases applied to the FEM. These test cases can be generated by applying forces

or displacements to the FEM, since either approach generates load-displacement pairs. The FEM used to construct the NLROM need only be analyzed during the identification phase, as the identified coefficients of the NLROM are used to compute the restoring force and the tangent stiffness once the model is identified. Normally, the identification process only requires access to the Finite Element (FE) force and displacement vectors, both of which can be queried in a commercial FE program. This process is known as "non-intrusive", because it can be used to construct an NLROM without having access to the source code of the FE implementation [26]. Most commonly, an NLROM assumes a restoring force that is a cubic polynomial function with respect to the modal displacements [6, 24, 26, 28].

In [29], the equation of motion from an FEM was projected directly onto a modal basis, but the assembly of the restoring force and tangent stiffness still relied on an element-level assembly procedure. In [42], coefficeints of a reduced-order model were computed directly using the isotropic von Kármán plate equations, in a procedure commonly referred to as "direct" identification. In [24, 28], an "indirect" or "non-intrusive" approach was employed, wherein the coefficients of a reduced-order model were identified by applying a series of static test cases to an FEM and querying the load-displacement data. In thin structures that consider geometric nonlinearity, membrane stretching effects can contribute significantly to the structural stiffness as the transverse deflections become large. In order to account for membrane effects, membrane DOFs can be directly included in the model using dual modes [15], or the membrane DOFs can be condensed into the transverse DOFs, yielding a governing equation that contains only transverse DOFs. Condensing the membrane DOFs in this way is appropriate where the in-plane inertia can reasonably be neglected. Full NLROMs have generally been identified using Displacement-Based (DB) techniques, wherein displacements are prescribed to the FEM, and either reaction forces [15, 26, 28] or structural stiffness matrices [34] are queried. A condensed NLROM can be constructed from a full NLROM by applying von Kármán assumptions to the full NLROM and writing the membrane DOFs as a function of the transverse DOFs, in a process known as explicit condensation [7, 36]. Alternatively, a condensed NLROM can be identified directly by querying the transverse

load-displacement data while the membrane DOFs are left unrestrained and unobserved. This has most commonly been accomplished using a force-based Implicit Condensation (IC) procedure, during which transverse forces are applied to the structure as linear combinations of the modal basis vectors [12, 24]. Membrane displacements of IC models have be recovered using a process termed Implicit Condensation with Expansion (ICE) [5, 10, 11]. One alternative approach that applies only transverse displacements while leaving the membrane DOFs unrestrained is used successfully in [49]. This idea was generalized and extended to FEMs with solid elements in [48]. The influence of temperature change has been considered in [25, 33].

1.2 Overview

This dissertation is primarily the conglomeration of three research papers, whose main contents are contained in Chapters 3, 4, and 5. This research has focused on developing new modeling approaches and gaining insight within the field of non-intrusive reduced-order modeling of geometrically nonlinear structures. Chapter 3, based on the journal article [41], establishes a connection between Ritz method solutions of geometrically nonlinear beams and non-intrusive NLROMs. In the course of that study, a shallow von Kármán beam theory is derived, and the approximate form attained using the Ritz method is used to (i) predict the value of NLROM parameters attained using non-intrusive methods and (ii) establish a new form of the restoring force used in the non-intrusive identification. Identified models using this new form of the restoring force are generated and validated. Chapter 2 discusses the theoretical foundations for non-intrusive NLROMs, including Galerkin projection, parameter identification procedures, and treatment of membrane displacements. The chapter also gives a brief introduction to static equilibrium paths, and examples are provided for two typical beam models.

Chapter 4 investigates challenges associated with identifying and analyzing NLROMs generated for curved beams, several of which challenges have been observed in the literature. High sensitivity of the large deformation behavior of curved beam NLROMs to small

changes in the model training data is first demonstrated using numerical examples of identified NLROMs. Even using the same training data, the updated form of the restoring force introduced in Chapter 3 yields a model that is significantly less sensitive to changes in the training data. A Taylor expansion of the restoring force of a curved beam FEM is used to demonstrate the insufficiency of using only configurations in the vicinity of the undeformed configuration for model training. Training data is then enriched by superimposing test cases on additional "base" configurations, giving rise to a significantly improved model fit. The quality of the fit is assessed for all configurations encountered on the static equilibrium path, allowing for the determination of which base configurations are most beneficial.

Chapter 5 addresses the need for NLROMs to consider local effects and structural damage via a substructuring approach. Rather than modifying an NLROM to account for local effects, the study couples an NLROM to an FEM, with the intention that local features and damage can be added to the FEM substructure. This approach is developed and tested on an FEM of a planar beam modeled with plane stress finite elements. Thickness-varying interface modes are used to handle the coupling between the NLROM and the FEM subdomains, and the modal DOFs governing the amplitudes of the interface modes are included in the NLROM. Both the displacements and stresses of the substructured models are validated under static loading by comparing results to the corresponding truth model FEM.

Chapter 6 summarizes the findings of this dissertation and proposes future work inspired during the process of the research.

Chapter 2

THEORETICAL FOUNDATIONS

2.1 Nonlinear reduced-order models

2.1.1 The projected finite element model

The equation of motion for an N-DOF structural finite element model with a nonlinear elastic restoring force and linear damping can be written as

$$\mathbf{M}\ddot{\mathbf{u}}(t) + \mathbf{C}\dot{\mathbf{u}}(t) + \mathbf{R}(\mathbf{u}(t)) = \mathbf{F}(t) \tag{2.1}$$

where $\mathbf{u}(t) \in \mathbb{R}^N$ is the vector of generalized nodal displacements, $\mathbf{M} \in \mathbb{R}^{N\times N}$ is the mass matrix, $\mathbf{C} \in \mathbb{R}^{N\times N}$ is the damping matrix, $\mathbf{R}(\mathbf{u}) : \mathbb{R}^N \mapsto \mathbb{R}^N$ is the restoring force vector, $\mathbf{F}(t) \in \mathbb{R}^N$ is the external force vector, and $t \in \mathbb{R}$ is time. The restoring force in Eq. (2.1) would typically be constructed using a finite element assembly procedure, wherein the contributions from each element are added to $\mathbf{R}(\mathbf{u})$ given the current displacements $\mathbf{u}(t)$. The reduced-order modeling strategy is to transform the vector of full-order DOFs $\mathbf{u}(t)$ to a much smaller vector of reduced-order displacements $\mathbf{q}(t) \in \mathbb{R}^M$, where $M \ll N$. Time dependency is hereinafter omitted for brevity. This change of coordinates can be accomplished by approximating $\mathbf{u}$ as a linear combination of modes $\boldsymbol{\phi}_1$, $\boldsymbol{\phi}_2$, $\boldsymbol{\phi}_3$, ... , $\boldsymbol{\phi}_M \in \mathbb{R}^N$ as

$$\mathbf{u} \approx \boldsymbol{\phi}_1 q_1 + \boldsymbol{\phi}_2 q_2 + \boldsymbol{\phi}_3 q_3 + ... + \boldsymbol{\phi}_M q_M = \boldsymbol{\Phi}\mathbf{q}\,, \tag{2.2}$$

where $\boldsymbol{\Phi} = [\boldsymbol{\phi}_1, \boldsymbol{\phi}_2, ... \boldsymbol{\phi}_M] \in \mathbb{R}^{N\times M}$ is a matrix whose columns contain M modes, each with N DOFs. Solving Eq. (2.1) for zero and computing the dot product with an arbitrary vector of weights $\delta\mathbf{u} \in \mathbb{R}^N$ yields the weak form of the equation of motion [14, 40]

$$\delta\mathbf{u} \cdot (\mathbf{M}\ddot{\mathbf{u}} + \mathbf{C}\dot{\mathbf{u}} + \mathbf{R}(\mathbf{u}) - \mathbf{F}) = 0 \quad \forall\ \delta\mathbf{u} \in \mathbb{R}^N\,. \tag{2.3}$$

Because Eq. (2.3) must be true for all possible values of $\delta\mathbf{u}$, the contents within the parentheses are still required to equal the zero vector. A Galerkin projection technique can then be applied using $\mathbf{u} \approx \mathbf{\Phi q}$ and $\delta\mathbf{u} \approx \mathbf{\Phi}\,\delta\mathbf{q}$ in Eq. (2.3), yielding

$$\delta\mathbf{q} \cdot \left(\mathbf{\Phi}^T\mathbf{M}\mathbf{\Phi}\ddot{\mathbf{q}} + \mathbf{\Phi}^T\mathbf{C}\mathbf{\Phi}\dot{\mathbf{q}} + \mathbf{\Phi}^T\mathbf{R}(\mathbf{\Phi q}) - \mathbf{\Phi}^T\mathbf{F}\right) = 0 \quad \forall\ \delta\mathbf{q} \in \mathbb{R}^N\,. \tag{2.4}$$

Since equation (2.4) must hold true for all values of $\delta\mathbf{q}$, the projected equation of motion can be extracted as

$$\tilde{\mathbf{M}}\ddot{\mathbf{q}} + \tilde{\mathbf{C}}\dot{\mathbf{q}} + \tilde{\mathbf{R}}(\mathbf{q}) - \tilde{\mathbf{F}} = \mathbf{0}\,, \tag{2.5}$$

where $\tilde{\mathbf{M}} = \mathbf{\Phi}^T\mathbf{M}\mathbf{\Phi}$, $\tilde{\mathbf{C}} = \mathbf{\Phi}^T\mathbf{C}\mathbf{\Phi}$, $\tilde{\mathbf{R}}(\mathbf{q}) = \mathbf{\Phi}^T\mathbf{R}(\mathbf{\Phi q})$, and $\tilde{\mathbf{F}} = \mathbf{\Phi}^T\mathbf{F}$.

Note that the projected restoring force vector $\tilde{\mathbf{R}}(\mathbf{q})$ can be constructed directly from a finite element assembly process by first computing the finite element displacements of the current state as $\mathbf{\Phi q}$. Once the restoring force vector $\mathbf{R}(\mathbf{\Phi q})$ is obtained from the assembly process, it can be pre-multiplied by $\mathbf{\Phi}^T$ to yield the projected restoring force vector. This is the procedure used in [29].

Rather than relying on finite element assembly, NLROM formulations assume that the restoring force $\tilde{\mathbf{R}}(\mathbf{q})$ is some function of the reduced-order DOFs $\mathbf{q}$, and the parameters of that function are identified from an FEM [26]. The form that is most commonly assumed for the restoring force is a cubic polynomial

$$\tilde{R}_i \approx \sum_{j=1}^{M} \tilde{K}_{ij}^{(1)} q_j + \sum_{j=1}^{M}\sum_{k=1}^{M} \tilde{K}_{ijk}^{(2)} q_k q_j + \sum_{j=1}^{M}\sum_{k=1}^{M}\sum_{l=1}^{M} \tilde{K}_{ijkl}^{(3)} q_l q_k q_j\,, \tag{2.6}$$

where $\tilde{K}_{ij}^{(1)}$, $\tilde{K}_{ijk}^{(2)}$, and $\tilde{K}_{ijkl}^{(3)}$ are parameters that determine the force-displacement response. This form of the NLROM restoring force function was derived using 3-D elasticity in [27]. When thermal effects are considered, the restoring force can be modified to be [25, 33]

$$\tilde{R}_i = \tilde{F}_i^{\Delta} + \sum_{j=1}^{M} \left(\tilde{K}_{ij}^{(1)} + \tilde{K}_{ij}^{\Delta}\right) q_j + \sum_{j=1}^{M}\sum_{k=1}^{M} \tilde{K}_{ijk}^{(2)} q_k q_j + \sum_{j=1}^{M}\sum_{k=1}^{M}\sum_{l=1}^{M} \tilde{K}_{ijkl}^{(3)} q_l q_k q_j\,, \tag{2.7}$$

where the parameters $\tilde{F}_i^{\Delta}$ and $\tilde{K}_{ij}^{\Delta}$ are the additional force and linear stiffness that result from temperature change. While these terms have primarily been used to account for thermal

effects, they can also apply to other misfit strains, such as those resulting from creep. The components of the stiffness coefficients in Eq. (2.6) or Eq. (2.7) are selected such that the projected force-displacement behavior of the NLROM best resembles that of the FEM used for the identification. This calibration has been achieved using a variety of methods. The full-order, N-DOF linear, quadratic, and cubic coefficients are not generally available from commercial finite element packages, but such coefficients could theoretically be generated by approximating the cubic restoring force behavior of the elements with respect to the nodal displacements. For even moderately complex models, such a task would prove prohibitively computationally expensive. Rather than projecting these coefficients directly, a restoring force function of the form in Eq. (2.6) is usually assumed, and the components of the stiffness coefficients are estimated numerically by applying test cases to the FEM and querying its response quantities.

2.1.2 Displacement-based non-intrusive identification

While FEMs are generated using the governing equations of the physical system, NLROMs are generated by testing an existing FEM and identifying parameters of an assumed restoring force function. This framework is often labeled as "non-intrusive" because it only requires access to the FEM displacements and forces, both of which can be queried in most commercial finite element programs. The governing equation of an NLROM, given in Eq. (2.5), relates the modal displacements of the model to the external modal forces of the model. Thus, if the number of known force-displacement pairs is equal to the number of independent unknown coefficients of the restoring force, a system of equations can be formed to solve for the unknown coefficients. If additional test cases are applied, an overdetermined system is formed that can be solved using a least-squares approach. In either case, the fitting method will determine a restoring force in the form of Eq. (2.6) that best (in some sense) fits the nonlinear behavior of the FEM, which may be of higher order. For this reason, the selection of test cases can affect the model identification, unless the FEM itself is a cubic system, which would be the case if elements were constructed from von Kármán beam theory.

Several approaches have been used to identify the restoring force parameters in Eq. (2.6), and most of them involve generating pairs of nodal displacements and forces. Additional approaches have been used to identify NLROM parameters from the tangent stiffness matrix of an FEM, as seen in [34]. These approaches reduce the number of required nonlinear analyses, but they are limited to finite element programs which make the stiffness matrix available to the analyst. This subsection will review one approach that constructs a model from force-displacement data.

Force-displacement pairs can be attained by (i) applying displacements to the FEM and querying the reaction forces (force-based) or (ii) applying forces to the FEM and querying the displacements (displacement-based). This research relied exclusively the displacement-based approach, which is summarized here. Each static solution of the FEM used in the identification of the NLROM will be referred to as a "test case", and the set of all test cases used for the identification of a single NLROM is the "training data". If a set of n_s test cases are applied, with test case p applying a modal displacement of $\mathbf{q}^p$, then the prescribed FEM displacement $\mathbf{u}^p$ for test p is

$$\mathbf{u}^p = \mathbf{\Phi}\,\mathbf{q}^p, \qquad p \in \{1, n_s\}\,. \tag{2.8}$$

The modal displacements $\mathbf{q}^p$ are selected to facilitate a unique solution for the stiffness coefficients in Eq. (2.6). Accounting for the symmetries $\tilde{K}^{(2)}_{ijk} \equiv \tilde{K}^{(2)}_{ikj}$ in the quadratic coefficients and $\tilde{K}^{(3)}_{ijkl} \equiv \tilde{K}^{(3)}_{ijlk} \equiv \tilde{K}^{(3)}_{ikjl} \equiv \tilde{K}^{(3)}_{iklj} \equiv \tilde{K}^{(3)}_{iljk} \equiv \tilde{K}^{(3)}_{ilkj}$ in the cubic coefficients, a minimum $\frac{11}{6}M + M^2 + \frac{1}{6}M^3$ test cases are required to solve for the parameters of the restoring force.

A displacement-based identification procedure named the STiffness Evaluation Procedure (STEP), originally proposed in [28], has been used frequently in the literature and is presented well in [26]. In the STEP, enforced displacements computed as a linear combination of one, two, or three modes are applied to the FEM. These combinations are chosen systematically to eliminate certain coefficients from the restoring force function, allowing coefficients to be solved for sequentially, instead of as a single system of equations. This reduces the computational effort of solving for the coefficients. Applying displacements to the FEM

in the shape of a single mode $\boldsymbol{\phi}_n$ with amplitudes q_n^a, q_n^b, and q_n^c yields a system of three equations (no summation on n)

$$\tilde{K}_{in}^{(1)} q_n^a + \tilde{K}_{inn}^{(2)} (q_n^a)^2 + \tilde{K}_{innn}^{(3)} (q_n^a)^3 = \tilde{F}_i^a \tag{2.9a}$$

$$\tilde{K}_{in}^{(1)} q_n^b + \tilde{K}_{inn}^{(2)} (q_n^b)^2 + \tilde{K}_{innn}^{(3)} (q_n^b)^3 = \tilde{F}_i^b \tag{2.9b}$$

$$\tilde{K}_{in}^{(1)} q_n^c + \tilde{K}_{inn}^{(2)} (q_n^c)^2 + \tilde{K}_{innn}^{(3)} (q_n^c)^3 = \tilde{F}_i^c \,, \tag{2.9c}$$

which can be used to solve for parameters $\tilde{K}_{in}^{(1)}$, $\tilde{K}_{inn}^{(2)}$, and $\tilde{K}_{innn}^{(3)}$. In total, $3M$ single-mode test cases are required. In like manner, applying displacements to the FEM as a linear combination of two modes $\boldsymbol{\phi}_n$ and $\boldsymbol{\phi}_m$ for all $n < m$ allows for the solution of $\tilde{K}_{inm}^{(2)}$, $\tilde{K}_{innm}^{(3)}$, and $\tilde{K}_{inmm}^{(3)}$, given the availability of $\tilde{K}_{in}^{(1)}$, $\tilde{K}_{im}^{(1)}$, $\tilde{K}_{inn}^{(2)}$, $\tilde{K}_{imm}^{(2)}$, $\tilde{K}_{innn}^{(3)}$, and $\tilde{K}_{immm}^{(3)}$. A total of $\frac{3}{2}M(M-1)$ two-mode test cases are required. Finally, displacements can be applied to the FEM as a linear combination of three modes $\boldsymbol{\phi}_n$, $\boldsymbol{\phi}_m$, and $\boldsymbol{\phi}_r$ for all $n < m < r$ to solve for $\tilde{K}_{inmr}^{(3)}$, given the availability of all previously solved parameters. A total of $\frac{1}{6}M(M-1)(M-2)$ three-mode test cases are required [26]. While the modal displacement $\mathbf{q}^p$ for test p in Eq. (2.8) can be chosen in a variety of ways, the modal displacement chosen using the STEP will be specifically referred to as $\mathbf{q}_s^p$ in this dissertation. The amplitudes of the applied displacement shapes should be large enough to encounter the nonlinearity, however [6] and [26] point out that parameters determined using a displacement-based procedure are not sensitive to the amplitude selection.

2.1.3 Displacement-based implicit condensation

A "full" NLROM that contains both transverse and membrane DOFs can be generated by including test cases that involve membrane modes in the identification procedure. Though such a model can be analyzed in its complete form, the membrane component of the inertial term is often small compared to the transverse component in shallow structures. Partitioning the equation of motion into transverse and membrane DOFs and neglecting the membrane component of the inertia allows for the membrane displacements to be written in terms of the

transverse displacements. Substituting this result back into the transverse component of the equation of motion yields a new equation containing only transverse displacements. This is known as an explicit condensation approach because a complete model is identified, and the membrane DOFs are explicitly condensed into the transverse DOFs. Because the expression for the membrane displacements in terms of the transverse displacements is available, the full displacement field can be recovered at any time step, allowing for the computation of stresses [7, 36].

In the IC approach, test cases are applied to the FEM with the membrane DOFs unloaded and unrestrained. Because the test cases in this approach have no net external force in the membrane component, the load-displacement information extracted from the test cases implicitly contains the membrane effects [12, 24]. Because the membrane response is not directly observed in the identification procedure, the IC approach does not allow for the explicit recovery of the membrane displacements. The ICE approach in [5, 10, 11], which reconstructs the membrane displacements using the membrane response from the test cases, has been implemented successfully and shown to produce a high-quality membrane displacement field. The membrane displacements are required if stresses are to be computed using the associated finite element model.

The STEP described in Subsection 2.1.2 is a displacement-based approach, wherein displacements are applied to the FEM during the identification phase and reaction forces are queried. The resulting NLROM is not condensed, because displacements are enforced to all DOFs. An alternative to the displacement-based approach, which will be referred to herein as the Displacement-Based Implicit Condensation (DBIC) approach, applies displacements to some of the DOFs of the FEM while the remaining DOFs are left unrestrained. This approach has been used in [49], and more recently in [48], where the approach was termed the Modified Stiffness Evaluation Procedure (M-STEP). In this study, the DBIC approach is specifically applied by prescribing displacements only to the transverse displacement DOFs. The rotation and membrane displacement DOFs are both left unrestrained, and they are allowed to resolve equilibrium in response to the applied transverse displacements. Because

the membrane DOFs are released, the transverse reaction forces obtained from the test cases are consistent with a condensed model. For a given test case p, the vector of transverse displacements $\mathbf{w}^p$ applied to the FEM is computed as

$$\mathbf{w}^p = \mathbf{\Phi}_b \, \mathbf{q}^p, \qquad p \in \{1, n_s\}, \tag{2.10}$$

where $\mathbf{q}^p$ is the vector of modal displacements, and $\mathbf{\Phi}_b \in \mathbb{R}^{N_b \times M}$ contains transverse component of the mode shapes. The rotation and axial displacement DOFs are not considered in the identification process, and the parameters $\tilde{K}_{ij}^{(1)}$, $\tilde{K}_{ijk}^{(2)}$, $\tilde{K}_{ijkl}^{(3)}$ of Eq. (2.6) reflect the behavior of the statically condensed model. The DBIC concept is illustrated in Fig. 2.1. This approach has several notable features that are potentially advantageous for identifying

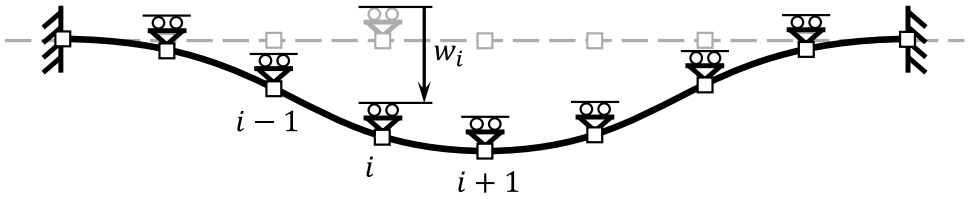

Figure 2.1: The DBIC concept

ROMs for curved beams, as compared with a force-based IC approach. First, as with a full or explicitly-condensed ROM constructed using a traditional displacement-based approach, the displacements that are prescribed to the FEM do not need to be solved for, thus reducing the problem size and with it the computational effort associated with compiling the training data. Second, specific displacement configurations can be more easily specified during the identification phase. In [46], one of the curved beam NLROMs studied was identified using the IC approach and training data in both the snapped and unsnapped positions because the scaling factors on the force-based test cases were sufficient to push the model into the snap-down position. The DBIC method allows for the snap-down position to be specifically targeted in the creation of the training data set. Furthermore, also in [46], several of the models were unable to be generated due to convergence issues in the FEM solver, and

the author concluded that the issue was more prevalent with intermediate-level loading. The DBIC method used herein is able to capture mid-snap-through configurations in the unstable region between the snapped and unsnapped configurations.

2.2 Static equilibrium paths

This dissertation makes frequent use of Static Equilibrium Paths (SEPs) to verify the quasi-static force-displacement response of structural models. A static equilibrium path can be defined as the set of all static equilibrium configurations encountered by a structural model under a fixed load pattern as the load factor is modulated, together with the load factor required to maintain each configuration. Static equilibrium paths have been used to validate NLROMs in [46], where they helped to assess the stability of curved beam NLROMs in the post-snap-through regime. The arc-length family of methods first proposed by Riks [39] is able to compute static equilbrium configurations of geometrically nonlinear structural systems where load-controlled static analysis fails. Chapters 3 and 4 make use of the arc-length method to compute SEPs for the beam models studied. Plots of the SEPs for both types of structures will be discussed in detail here to aid in the interpretation of results.

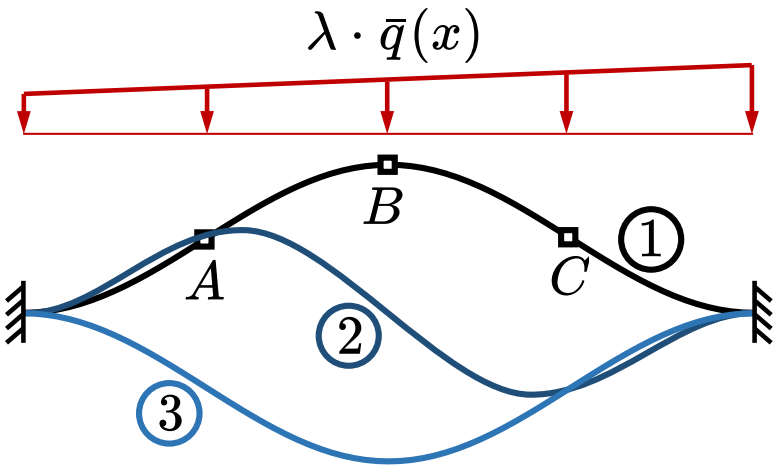

Figure 2.2: Three sample configurations on the SEP of the straight buckled beam

This subsection will discuss the typical SEPs for two distinct beam structure types that will be seen frequently in this dissertation. The first type, studied in Chapter 3, is an initially straight beam that has been mechanically buckled by shortening the distance between the supports. The second type, studied in Chapter 4, is a curved beam with a circular arc profile and no support movement. Both beam types are loaded transversely with a nearly-uniform distributed load that has a slight asymmetry in order to induce asymmetric snap-through of the beam.

Consider a horizontal fixed-fixed beam that is straight in its undeformed configuration. The supports are moved closer together to induce a compressive axial force that exceeds the critical buckling load of the beam. The beam is then allowed to snap into the upward post-buckled configuration, designated as configuration (1) in Fig. 2.2. A distributed reference load $\bar{q}(x)$ scaled by a load factor λ is applied transversely to the beam. As the load factor λ is increased, the beam begins to transition from the "snap-up" configuration to the "snap-

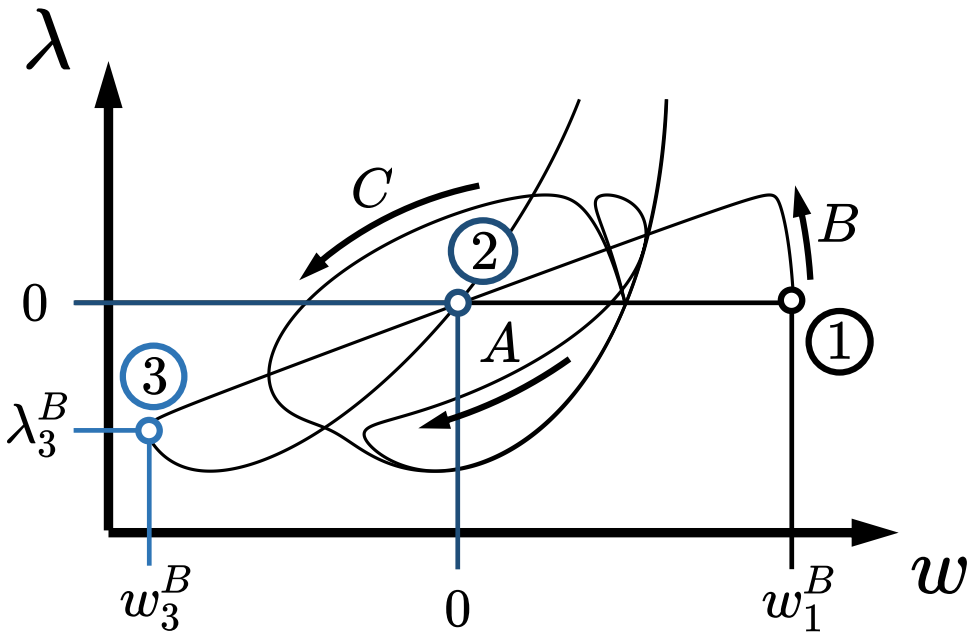

Figure 2.3: Typical SEP of a straight post-buckled beam under nearly uniform loading

down" configuration. The beam encounters configuration (2) when the load factor decreases back to zero. The beam then transitions to configuration (3) as the load factor becomes more negative.

Static equilibrium paths can be shown graphically by plotting the load factor on the vertical axis versus certain characteristic displacements on the horizontal axis. Figure 2.3 shows a typical plot of the SEP of the straight beam in Fig. 2.2. The displacements plotted are the transverse displacements (deflections) of the points A, B, and C in Fig. 2.2 corresponding to the 1/4, 1/2, and 3/4 points of the beam, respectively. Let the deflection of the beam (upward positive) be represented by $w(x)$. The query location is indicated on each curve, along with the direction that the arc-length method progresses. Note that for this beam, all three deflections start with a nonzero value when the load factor is zero. This is due to the buckled configuration being maintained by the axial load in the absence of any transverse loading. Figure 2.3 also shows the three points on the curve for location B (the midpoint) corresponding to the three configurations (1), (2), and (3).

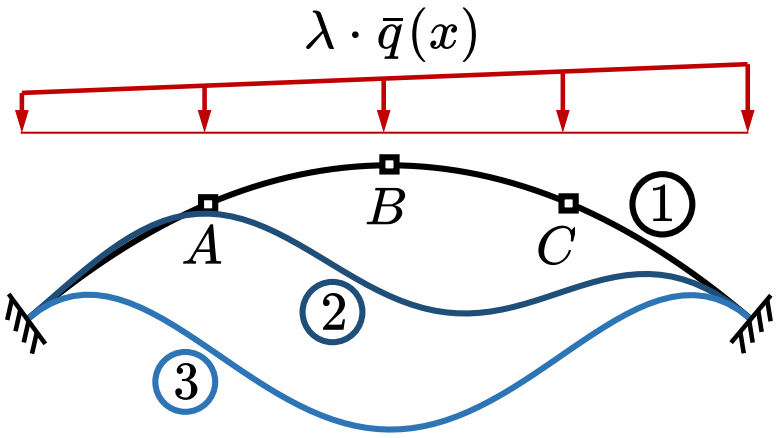

Figure 2.4: Three sample configurations on the SEP of the curved beam

Figure 2.4 illustrates the typical curved beam studied in Chapter 4. The undeformed profile of the beam is that of a circular arc. The ends of the beam are fixed, and the supports do not displace. The same reference load $\bar{q}(x)$ is used for the curved beam as was

used for the straight beam in Fig. 2.2. As the load factor is increased, the beam begins to transition from the undeformed configuration to the snap-down configuration. The beam encounters configuration (2) after the load factor reaches its maximum pre-snap-through value and begins to decrease again. After the load factor reaches its minimum post-snap-through value, which can be positive, it begins increasing again until configuration (3) is reached.

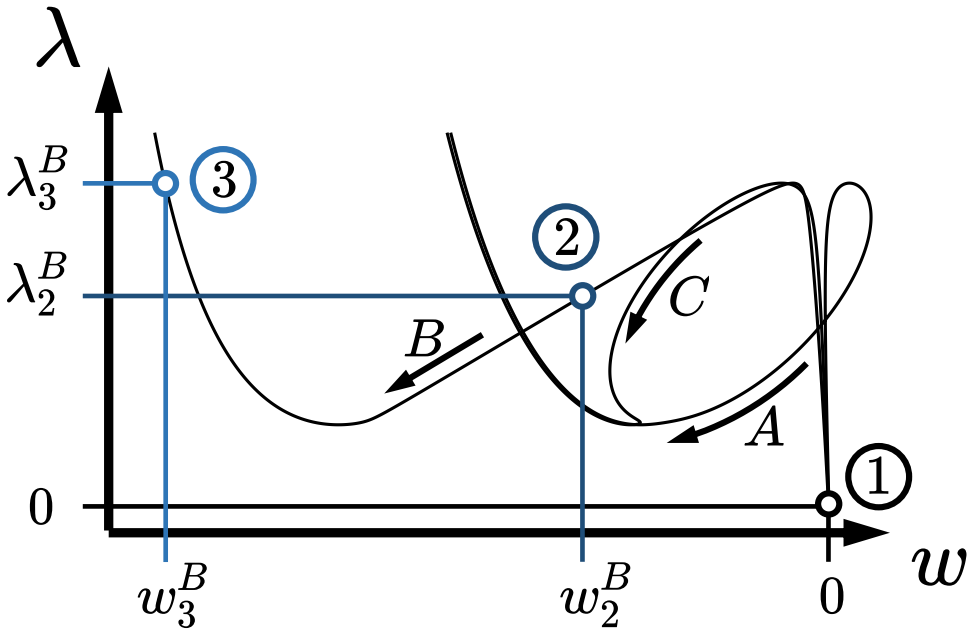

Figure 2.5: Typical SEP of a curved beam under nearly uniform loading

Figure 2.5 shows the plot of the SEP for the curved beam, showing the same three query locations of A, B, and C. Note that, unlike in Fig. 2.3, all three deflections begin at zero when the beam is unloaded. This is because there is no axial load creating an initial deflection. The three configurations from Fig. 2.4 are plotted on the curve for location B.

Chapter 3

GUIDED IDENTIFICATION OF NONLINEAR REDUCED-ORDER MODELS VIA THE INCORPORATION OF VON KÁRMÁN BEAM THEORY

3.1 Introduction

3.1.1 Overview

This chapter investigates the differences and similarities between Ritz-Galerkin formulations and identified NLROMs. The primary focus of the chapter is on initially-straight, post-buckled beams. Initial curvature in beams is considered in the nonlinear beam derivation, and its anticipated effects on the structure of NLROMs are described. Extensions to curved beams are studied in Chapter 4.

The work relies on several modeling approaches. First, a condensed Von Kármán beam is used as the base theory to which the Ritz-Galerkin method is applied. Models are generated for the CVK theory using both a continuous modal basis and a nodal FE basis. Second, an FEM composed of Co-RoTational (CRT) beam elements is used as both the "truth model" by which other models are evaluated and as the FE tool from which the NLROMs are identified. The models studied are analyzed using the arc-length method, similar to that used in [46], and the SEPs of the different models are compared. An error metric is developed and used to evaluate the relative error in the SEP of the model of interest versus that of the truth model. A derivation of the static equilibrium equations for the shallow von Kármán beam model is provided, and the analytical condensation of the axial displacements is shown. The matrix form of the Condensed Von Kármán (CVK) beam model is expanded in index notation, and the correlation between the CVK beam equations and the NLROM equations is demonstrated. The matrix form of the CVK beam model is used to develop a simplified,

tangent stiffness-based procedure for identifying a reduced-order model of a beam. This will be referred to as the "guided" identification procedure, and models generated from the procedure will be called Guided Reduced-Order Models (GROMs).

Using a displacement-based identification approach, the identification of an M-mode NLROM requires $O(M^3)$ static solutions of the FEM used for the identification. Taking advantage of the availability of the tangent stiffness matrix allows for an M-mode NLROM to be identified using $O(M^2)$ static solutions [34]. Thus, the NLROM identification process becomes rapidly more computationally expensive as the modal basis is enriched. The guided identification procedure proposed in this work allows for the identification of a condensed beam model using only two static solutions of the FEM, regardless of the number of modes. This provides significant value to analysts, as the computational effort of identifying a reduced-order structural model is greatly reduced and independent of modal enrichment. Furthermore, the number of unique parameters required to be stored for the guided model is $O(M^2)$, a notable reduction from the $O(M^4)$ parameters required for an NLROM. As an additional benefit of this method, no transverse displacement test cases need to be applied to the FEM, thus eliminating the possibility of modal amplitude selection impacting the error of the parameter fit. The current work validates the guided identification procedure for straight, prismatic beams experiencing an axial misfit by verifying post-buckling load-displacement response. While the numerical studies in this work focus on straight, prismatic beams, the guided identification procedure is extensible to non-prismatic beams with shallow curvature.

While the motivation for developing reduced-order structural models is often the simulation of dynamic response, the most complex aspect of the models is the restoring force term. Indeed, the two modeling approaches herein have identical inertial terms. Hence, this paper focuses on a comparison of quasi-static force-displacement response, and the dynamic response of the models is not directly computed. Though arguments could be made that models should be compared via their dynamic simulation results, the approach used herein allows for a more direct comparison of the terms of the governing equations without the

challenges posed by nonlinear dynamics (for which even two identical models may appear very different due to sensitivity to initial conditions).

3.1.2 Chapter outline

Section 3.2 provides a derivation for a shallow-curvature von Kármán beam model, which is used extensively in this work. Section 3.3 investigates the connection between the CVK beam equations and NLROMs. Subsection 3.3.1 illustrates how the cubic NLROM structure can be extracted analytically from the CVK beam equations. Subsection 3.3.2 presents a simplified identification procedure for a reduced-order model that utilizes the CVK beam restoring force. Section 3.4 presents a numerical case study used to compare several modeling techniques. Subsection 3.4.1 introduces the physical and loading parameters of the test problem used in the numerical case study. Subsection 3.4.2 outlines the development of the numerical models. Subsection 3.4.3 presents the modal basis used for modal solutions in this study. Subsection 3.4.4 presents the results of the numerical analyses and provides an error analysis. Section 3.5 states the conclusions of the study.

3.2 Shallow von Kármán beam theory

This work directly uses terms of the shallow curved von Kármán beam equations to provide insight into NLROM coefficients for beams. Thus, this section briefly summarizes the derivation and frames the equations in a form that can be compared with NLROMs. The derivation is primarily an adaptation of W.T. Koiter's shallow shell theory in [9] to beams, but it is presented here for convenience and to provide consistent notation. The beam geometry, kinematics, and internal forces are shown in Fig. 3.1, where $u(x)$ and $w(x)$ are the horizontal and vertical displacements of the centroid, respectively, and $h(x)$ is the unstressed vertical position of the centroid. The vertical load $q(x)$, internal forces on deformed system ($V(x)$, $N(x)$, and $M(x)$), and internal forces on the undeformed system ($Q(x)$, $H(x)$, and $M(x)$) are also shown. The right end of the beam has an applied moment M_L, an applied vertical force Q_L, and an applied horizontal force H_L. The beam has non-homogeneous bending and

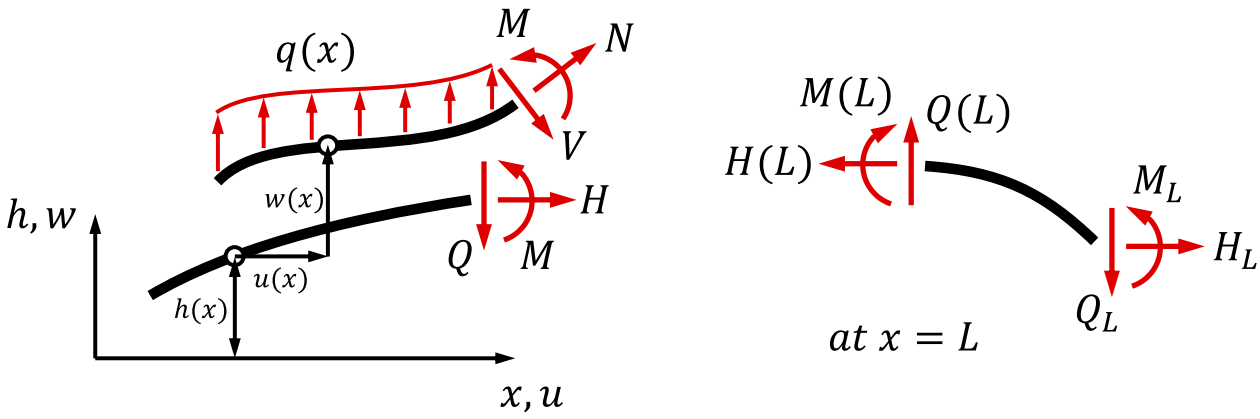

Figure 3.1: Beam kinematics, internal forces, and boundary conditions

axial stiffnesses of $EI(x)$ and $EA(x)$, respectively. The length Δs of the centroidal axis at over a small interval $[x, x+\Delta x]$ in the deformed configuration is

$$\begin{aligned}\Delta s &= \left[(\Delta x + u(x+\Delta x) - u(x))^2 + (h(x+\Delta x) - h(x) + w(x+\Delta x) - w(x))^2\right]^{\frac{1}{2}} \\ &= \Delta x\Big[\left(1 + \tfrac{1}{\Delta x}\left[u(x+\Delta x) - u(x)\right]\right)^2 \\ &\qquad + \left(\tfrac{1}{\Delta x}\left[h(x+\Delta x) - h(x)\right] + \tfrac{1}{\Delta x}\left[w(x+\Delta x) - w(x)\right]\right)^2\Big]^{\frac{1}{2}}\end{aligned} \tag{3.1}$$

Computing the limit of Δs as Δx goes to zero yields

$$ds = \lim_{\Delta x \to 0} \Delta s = dx\sqrt{(1+u')^2 + (h'+w')^2} \tag{3.2}$$

Evaluating this for the undeformed configuration with $u(x) = 0$ and $w(x) = 0$ yields the undeformed length ds_0.

$$ds_0 = dx\sqrt{1 + (h')^2} \tag{3.3}$$

The Green-Lagrange strain of the centroidal axis can be computed as

$$\begin{aligned}\varepsilon &= \frac{1}{2}\left(\frac{ds^2}{ds_0^2} - 1\right) = \frac{1}{2}\left(\frac{(1+u')^2 + (h'+w')^2}{1 + (h')^2} - 1\right) \\ &\approx u' + h'\,w' + \frac{1}{2}(w')^2\end{aligned} \tag{3.4}$$

neglecting $(h')^2 \approx 0$ (limited to shallow arches) and $(u')^2 \approx 0$ (horizontal displacements much smaller than transverse displacements). The rotation of the cross-section will be approximated as $w'(x)$, allowing the curvature change φ to be computed as

$$\varphi \approx w'' \tag{3.5}$$

Let ε_0 represent an axial misfit strain, which can result from a temperature change or other causes such as creep. Assuming a linear elastic material model, the potential energy of the system can be expressed as

$$\Pi = \int_0^L \left(\tfrac{1}{2}EA(\varepsilon - \varepsilon_0)^2 + \tfrac{1}{2}EI\varphi^2 - q\,w\right) dx - \overline{H}_L u_L + \overline{Q}_L w_L - \overline{M}_L w'_L \tag{3.6}$$

where $\overline{Q}_L$ is the vertical end force at $x = L$, $\overline{H}_L$ is the horizontal end force at $x = L$, and $\overline{M}_L$ is the end moment at $x = L$. The overline designates a prescribed value. Setting the variation of the potential energy function equal to zero yields

$$\begin{aligned} \delta\,\Pi(u, w, \delta u, \delta w) = \int_0^L &(H\,\delta\varepsilon + M\,\delta\varphi - q\,\delta w)\,dx \\ &- \overline{H}_L \delta u(L) + \overline{Q}_L \delta w(L) - \overline{M}_L \delta w'(L) \end{aligned} \tag{3.7}$$

where M and H are obtained as

$$M = EI\varphi \tag{3.8a}$$

$$H = EA(\varepsilon - \varepsilon_0)\,. \tag{3.8b}$$

The variations of the strains, $\delta\varepsilon$ and $\delta\varphi$, must be expressed in terms of the variations of the primary variables, δu and δw. This can be accomplished by computing the variations of the results in Eqs. (3.4) and (3.5) as

$$\delta\varepsilon = \delta u' + (h' + w')\,\delta w' \qquad\qquad \delta\varphi = \delta w'' \tag{3.9a,b}$$

The terms of Eq. (3.7) are integrated by parts until the variations of the primary variables (δu, δw) within the integrals have no derivatives.

$$\begin{aligned}\delta\,\Pi(u,w,\delta u,\delta w) = &\int_0^L \left(M'' - \left(H(h'+w')\right)' - q\right)\,\delta w\,dx - \int_0^L H'\,\delta u\,dx \\ &+ \left(H(h'+w')|_L - M'|_L + Q_L\right)\delta w(L) \\ &+ \left(H|_L - \overline{H}_L\right)\delta u(L) + \left(M|_L - \overline{M}_L\right)\delta w'(L) \\ &- H|_0\,\delta u(0) + \left(M'|_0 - H(h'+w')|_0\right)\delta w(0) - M|_0\,\delta w'(0) = 0\end{aligned} \tag{3.10}$$

Using the Fundamental Lemma of the Calculus of Variations (FLCV) [3], the strong form equations can be extracted from the independent weighted residual terms. The governing differential equations are

$$M'' - \left(H(h'+w')\right)' - q = 0 \qquad \forall x \in [x, L] \tag{3.11a}$$

$$H' = 0 \qquad \forall x \in [x, L] \tag{3.11b}$$

and the natural boundary conditions are

$$H|_L - \overline{H}_L = 0 \tag{3.12a}$$

$$H(h'+w')|_L - M'|_L + \overline{Q}_L = 0 \tag{3.12b}$$

$$M|_L - \overline{M}_L = 0 \tag{3.12c}$$

Equation (3.11b) indicates that $H(x)$ is constant. Note that $H(x)$ represents the horizontal force in the beam and not the normal force, as indicated by the boundary condition in Eq. (3.12a). Substituting Eq. (3.11b) into Eq. (3.11a) yields a simplified governing equation.

$$M'' - H\left(h'' + w''\right) - q = 0 \qquad \forall x \in [0, L] \tag{3.13}$$

Integrating Eq. (3.11b) and using the boundary condition from Eq. (3.12a) to solve for the constant of integration yields

$$H(x) = \overline{H}_L = \text{const}\,. \tag{3.14}$$

Substituting Eq. (3.14) equal into Eq. (3.8b) and solving for $u'(x)$ yields

$$u'(x) = \frac{\overline{H}_L}{EA} + \varepsilon_0 - \left(h'w' + \tfrac{1}{2}(w')^2\right) \tag{3.15}$$

This equation can be integrated between the bounds of $\xi = 0$ and $\xi = x$ to yield the solution for $u(x)$.

$$u(x) = u(0) + \overline{H}_L \int_0^x \frac{d\xi}{EA(\xi)} + \varepsilon_0 x - \int_0^x \left(h'(\xi)w'(\xi) + \tfrac{1}{2}(w'(\xi))^2\right)\, d\xi \tag{3.16}$$

In the case both ends of the beam being horizontally restrained, the horizontal force H_L can be solved for in terms of the horizontal end displacements by evaluating the previous equation at $x = L$.

$$\begin{aligned} \overline{H}_L &= \frac{1}{\int_0^L \frac{1}{EA}\, dx} \left(u(L) - u(0) - \varepsilon_0 L + \int_0^L \left(h'w' + \tfrac{1}{2}(w')^2\right)\, dx \right) \\ &= \overline{k}_a \left(\delta_u - \varepsilon_0 L + \int_0^L \left(h'w' + \tfrac{1}{2}(w')^2\right)\, dx \right) \end{aligned} \tag{3.17}$$

where δ_u is the difference in the horizontal end displacements, $u(L) - u(0)$, and $\overline{k}_a$ is defined as

$$\overline{k}_a = \frac{1}{\int_0^L \frac{1}{EA}\, dx} \tag{3.18}$$

This represents the resultant axial stiffness of the beam, which can be non-prismatic. In the case of a prismatic beam with constant EA, the value of $\overline{k}_a$ evaluates to $\frac{EA}{L}$. The result in Eq. (3.17) can be substituted into Eq. (3.13), yielding the strong form of the condensed von Kármán beam equation.

$$(EIw'')'' - \overline{k}_a \left(\delta_u - \varepsilon_0 L + \int_0^L \left(h'\, w' + \frac{1}{2}(w')^2 \right) dx \right) (h'' + w'') - q = 0 \tag{3.19}$$

Multiplying this equation by a virtual displacement δw and integrating over the domain yields the weak form of the differential equation. Using the Ritz-Galerkin method with interpolation functions $\phi_i(x)$ for the transverse displacement $w(x)$ and $\phi_i^h(x)$ for the imperfection $h(x)$ yields the matrix form of the equilibrium expression [53]

$$\mathbf{K}\mathbf{w} + \overline{k}_a \left(\delta_u - \varepsilon_0 L + \mathbf{w}^T \mathbf{G}_{wh} \mathbf{h} + \tfrac{1}{2}\mathbf{w}^T \mathbf{G} \mathbf{w}\right) (\mathbf{G}\mathbf{w} + \mathbf{G}_{wh}\mathbf{h}) - \mathbf{F} = \mathbf{0}\,, \tag{3.20}$$

where the vector $\mathbf{w}$ contains the transverse displacement and rotation degrees of freedom and the vector $\mathbf{h}$ contains the general coordinates describing the shape of the initial curvature.

The transverse displacement is approximated as $w(x) \approx \sum_i \phi_i(x) w_i$, and the imperfection is approximated as $h(x) \approx \sum_i \phi_i^h(x) h_i$. The elements of the matrices $\mathbf{K}$, $\mathbf{G}$, and $\mathbf{G}_{wh}$ and the vector $\mathbf{F}$ are defined as

$$K_{ij} = \int_0^L EI\, \phi_i''(x)\phi_j''(x)\, dx \qquad F_i = \int_0^L \phi_i(x) q(x)\, dx \tag{3.21a,b}$$

$$G_{ij} = \int_0^L \phi_i'(x)\phi_j'(x)\, dx \qquad (G_{wh})_{ij} = \int_0^L \phi_i'(x)(\phi_j^h)'(x)\, dx\,. \tag{3.21c,d}$$

The imperfection vector $\mathbf{h}$ only appears in the governing equation in the form of the product $\mathbf{G}_{wh}\mathbf{h}$. To simplify notation, this product will be replaced by an equivalent vector $\boldsymbol{\gamma} \equiv \mathbf{G}_{wh}\mathbf{h}$. The tangent stiffness matrix for the equilibrium expression in Eq. (3.20) can be computed as

$$\mathbf{K}_{_{CVK}} = \mathbf{K} + \overline{k}_a \left(\delta_u + \mathbf{w}^T\boldsymbol{\gamma} + \tfrac{1}{2}\mathbf{w}^T\mathbf{G}\mathbf{w}\right)\mathbf{G} + \overline{k}_a(\mathbf{G}\mathbf{w}+\boldsymbol{\gamma})(\mathbf{G}\mathbf{w}+\boldsymbol{\gamma})^T. \tag{3.22}$$

The tangent stiffness will be required for the Newton-Raphson algorithm, as well as for the identification procedure to be introduced in the upcoming Section 3.3.

3.3 Extracting the NLROM Structure from the CVK theory

3.3.1 The structure of the condensed von Kármán model

The matrix form of the CVK equilibrium equations, as given in Eq. (3.20), can be expressed in index notation to identify the components of the cubic coefficients, as shown in Eq. (3.23).

$$\begin{aligned} g_i(\mathbf{w}) = \left(K_{ij} + \overline{k}_a\delta_u G_{ij} + \overline{k}_a\gamma_i\gamma_j\right) w_j + \overline{k}_a\left(G_{ij}\gamma_k + \tfrac{1}{2}\gamma_i G_{jk}\right) w_k w_j \\ + \tfrac{1}{2}\overline{k}_a\left(G_{ij}G_{kl}\right) w_l w_k w_j - \left(F_i - \overline{k}_a\delta_u\gamma_i\right) = 0 \end{aligned} \tag{3.23}$$

The coefficients of the cubic polynomial in Eq. (2.7) can then be computed as the coefficients of the cubic Taylor expansion of $g_i(\mathbf{w})$ about the undeformed configuration $\mathbf{w} = \mathbf{0}$. The terms containing δ_u are included as part of the misfit force and stiffness.

$$\tilde{K}_{ij}^{(1)} = K_{ij} + \overline{k}_a\gamma_i\gamma_j \qquad \tilde{K}_{ij}^{\Delta} = \overline{k}_a\delta_u G_{ij} \qquad \tilde{F}_i^{\Delta} = -\overline{k}_a\delta_u\gamma_i \tag{3.24a,b,c}$$

$$\tilde{K}_{ijk}^{(2)} = \frac{1}{2}\frac{\partial^2 g_i}{\partial w_j \partial w_k}\bigg|_{\mathbf{w}=\mathbf{0}} = \tfrac{1}{2}\,\overline{k}_a\left(G_{ij}\gamma_k + G_{ik}\gamma_j + G_{jk}\gamma_i\right) \tag{3.24d}$$

$$\tilde{K}^{(3)}_{ijkl} = \frac{1}{6}\frac{\partial^3 g_i}{\partial w_j \partial w_k \partial w_l}\bigg|_{\mathbf{w}=\mathbf{0}} = \tfrac{1}{6}\,\overline{k}_a\,(G_{ij}G_{kl} + G_{ik}G_{jl} + G_{il}G_{jk}) \tag{3.24e}$$

Equation (3.24c) shows that the δ_u term, which represents the difference in the horizontal end displacements, gives rise to an additional constant term. This represents the "misfit force" on the system that can induce a transverse displacement without external transverse forcing. Note that this term is only nonzero when both $\boldsymbol{\gamma}$ and δ_u are nonzero. Physically, this means that an axial support displacement will only result in an unloaded transverse displacement when there is some curvature in the beam. In a straight beam, an axial shortening will result in an unstable system if the buckling load is exceeded, but the straight configuration remains an unstable equilibrium configuration with no transverse load applied. In the presence of any curve, the undeformed configuration for the non-transversely loaded beam disappears for nonzero axial loads.

The linear stiffness is comprised of the linear stiffness of the flat beam, the "mistfit stiffness" containing δ_u, and the imperfection term containing $\boldsymbol{\gamma}$. This means that changes to the linear stiffness resulting from a horizontal support displacement are proportional to $\mathbf{G}$. Because $\boldsymbol{\gamma}$ is directly proportional to the height of the imperfection, the linear stiffness is proportional to the square of the imperfection height. Each term of the quadratic stiffness contains $\boldsymbol{\gamma}$, so the quadratic terms vanish in the case of a flat beam. The cubic term remains the same regardless of the imperfection shape or axial elongation. The invariance of the cubic term with respect to the imperfection shape and amplitude is, of course, contingent on the shallow arch assumptions in the CVK derivation in Section 3.2. The assumption of $h'(x) \ll 1$ was used in the formulation of the strain, and this model should only be used where that assumption is reasonable.

3.3.2 Guided identification using the condensed von Kármán formulation

Inspection of Eq. (3.24a-e) reveals that the NLROM parameters of a beam model constructed from the CVK theory are functions of a smaller set of parameters—two matrices $\mathbf{K}$ and $\mathbf{G}$, a vector $\boldsymbol{\gamma}$, and a scalar $\overline{k}_a$. If, instead of being derived analytically using Eq. (3.21a-d),

these parameters are identified using static solutions of an FEM, the equivalent NLROM parameters in Eqs. (3.24a-e) can be computed. It it observed that specifying zero transverse displacement, i.e. $\mathbf{w} = \mathbf{0}$, in Eqs. (3.17), (3.20), and (3.22) yields a simplified set of equations involving $\mathbf{K}$, $\mathbf{G}$, $\boldsymbol{\gamma}$, $\overline{k}_a$, and δ_u, of which the first four are unknown and δ_u is prescribed.

$$H_L = \overline{k}_a \delta_u \tag{3.25a}$$

$$\overline{k}_a \delta_u \boldsymbol{\gamma} = \mathbf{F} \tag{3.25b}$$

$$\mathbf{K}_{CVK}\big|_{\mathbf{w}=\mathbf{0}} = \mathbf{K} + \overline{k}_a \delta_u \mathbf{G} + \overline{k}_a \boldsymbol{\gamma}\boldsymbol{\gamma}^T \tag{3.25c}$$

Evaluating Eq. (3.25a-c) with two trial values of δ_u yields four nontrivial equations to solve for the four unknowns. Specifically, trial values of $\delta_u = 0$ and $\delta_u = \delta_u^{tr}$ are used, where δ_u^{tr} is a small, nonzero elongation or shortening of the beam. A non-intrusive approach will be employed in which response quantities of an FEM are used to solve for the parameters of the CVK governing equation, rather than solving for the parameters of Eq. (2.7) as is done for NLROMs. Specifically, the equivalent values of H_L, $\mathbf{F}$, and $\mathbf{K}_{CVK}$ must be determined from the FEM. While this process may be extensible to more general FEMs, the identification procedure described here will be assumed to use a CRT FEM as the basis for the identification.

Recall that $\mathbf{F}$ and $\mathbf{K}_{CVK}$ in Eq. (3.25a-c) are purely transverse, as the axial DOFs are condensed into the transverse DOFs. In the CRT FEM solution, the horizontal force H_L can be taken to be the horizontal reaction force at the beam support (for example, where the end displacement is applied). The vector $\mathbf{F}$ and matrix $\mathbf{K}_{CVK}$ can be approximated by the transverse component of the CRT FEM force vector and condensed CRT FEM tangent stiffness matrix, respectively. Because the CVK model is statically condensed, the FEM must have the axial DOFs unloaded and unrestrained during the static solutions to be consistent with Eq. (3.25a-c). Additionally, the tangent stiffness matrix from the CRT FEM must be condensed as follows. If the transverse components are denoted by the subscript w and the axial components by the subscript u, the stiffness matrix of the FEM $\mathbf{K}_{\text{FEM}}$ can be

partitioned into its transverse and axial components as

$$\mathbf{K}_{\text{FEM}} = \begin{bmatrix} \mathbf{K}_{ww} & \mathbf{K}_{wu} \\ \mathbf{K}_{uw} & \mathbf{K}_{uu} \end{bmatrix} , \tag{3.26}$$

and the condensed transverse stiffness matrix $\overline{\mathbf{K}}$ can be computed as

$$\overline{\mathbf{K}} = \mathbf{K}_{ww} - \mathbf{K}_{wu}\mathbf{K}_{uu}^{-1}\mathbf{K}_{uw} \, . \tag{3.27}$$

The two previously mentioned trial states, with $\delta_u = 0$ and $\delta_u = \delta_u^{tr}$, are applied to the CRT FEM by prescribing a horizontal end displacement of δ_u to the end node. The unrestrained axial displacements must be allowed to find equilibrium prior to querying H_L, $\mathbf{F}$, and $\mathbf{K}_{_{CVK}}$. Recall that Eq. (3.25a-c) is for the case of $\mathbf{w} = \mathbf{0}$, so the CRT FEM solutions must be attained with the transverse displacements restrained.

Examination of Eq. (3.25c) reveals that setting $\delta_u = 0$ eliminates $\mathbf{G}$ from the equation, making the system of equations simpler to solve. In the first analysis with $\delta_u = 0$, the tangent stiffness matrix of the CRT FEM is queried in the unloaded, undeformed configuration. Because no external loads or displacements are applied, this analysis is trivial. In the second analysis, a trial axial end displacement of δ_u^{tr} is applied to the beam while the transverse displacements (and rotations, if considered) are restrained. The axial displacements are unrestrained and must be allowed to resolve equilibrium. Once the solution is converged for the trial δ_u^{tr}, the tangent stiffness matrix, the transverse component of the reaction force vector $\mathbf{F}_P$, the horizontal end reaction force H_P, and the tangent stiffness matrix are queried.

The tangent stiffness matrices of the two analyses are condensed using Eq. (3.27), and the resulting condensed matrices are denoted $\mathbf{K}_0$ and $\mathbf{K}_P$ for $\delta_u = 0$ and $\delta_u = \delta_u^{tr}$, respectively. If each of these stiffness matrices is substituted for $\mathbf{K}_{_{CVK}}\big|_{\mathbf{w}=\mathbf{0}}$ in Eq. (3.25c), and the transverse reaction force $\mathbf{F}_P$ is substituted for $\mathbf{F}$ in Eq. (3.25b), a system of four equations is generated.

$$H_P = \overline{k}_a \delta_u^{tr} \tag{3.28a}$$

$$\mathbf{K}_0 = \mathbf{K} + \overline{k}_a \boldsymbol{\gamma}\boldsymbol{\gamma}^T \tag{3.28b}$$

$$\mathbf{K}_P = \mathbf{K} + \overline{k}_a \delta_u^{tr} \mathbf{G} + \overline{k}_a \boldsymbol{\gamma}\boldsymbol{\gamma}^T \tag{3.28c}$$

$$\mathbf{F}_P = \overline{k}_a \delta_u^{tr} \boldsymbol{\gamma} \tag{3.28d}$$

These four equations contain the unknown parameters $\mathbf{K}$, $\mathbf{G}$, $\boldsymbol{\gamma}$, and $\overline{k}_a$, and the prescribed parameter δ_u^{tr}. Equation (3.28a) can be easily solved for the resultant axial stiffness $\overline{k}_a$.

$$\overline{k}_a = \frac{H_P}{\delta_u^{tr}} \tag{3.29}$$

For relatively small initial curvatures, the value of $\overline{k}_a$ attained using Eq. (3.29) is close to the actual axial stiffness $\frac{EA}{L}$ used in the FEM. As the imperfection height becomes large, this identification technique begins to underestimate the axial stiffness. It has been observed that this procedure yields a high-quality model for circular imperfections of up to about 2% of the beam length. Once the axial stiffness is identified, Eq. (3.28d) can be used to solve for the imperfection term $\boldsymbol{\gamma}$, yielding

$$\boldsymbol{\gamma} = \frac{1}{\overline{k}_a \delta_u^{tr}} \mathbf{F}_P \,. \tag{3.30}$$

If the beam represented in the FEM is perfectly flat and lacking any support eccentricity, $\boldsymbol{\gamma}$ is equal to zero and does not need to be identified. Subtracting Eq. (3.28b) from Eq. (3.28c) and solving for $\mathbf{G}$ yields

$$\mathbf{G} = \frac{1}{\overline{k}_a \delta_u^{tr}} (\mathbf{K}_P - \mathbf{K}_0) \,. \tag{3.31}$$

Once the imperfection term is identified, Eq. (3.28b) can be used to solve for $\mathbf{K}$. Again, if there is no imperfection, then $\mathbf{K}$ is simply equal to $\mathbf{K}_0$.

$$\mathbf{K} = \mathbf{K}_0 - \overline{k}_a \boldsymbol{\gamma}\boldsymbol{\gamma}^T \tag{3.32}$$

This implies that the full cubic behavior, according to the assumptions behind the CVK theory, can be constructed using only linear tangent stiffness evaluations in the zero-transverse deflection configuration. In the numerical investigation, the tangent stiffness matrices and reaction forces of a CRT model were used in this procedure to identify the equivalent CVK parameters. Equations (3.24a-e) were then used to construct the equivalent NLROM coefficients. A ROM identified using this procedure will be referred to as a Guided Reduced-Order Model (GROM).

During preliminary numerical studies, it was observed that the model parameters were not sensitive to the choice of δ_u^{tr}. No significant difference was observed between models generated in axial tension, compression less than the buckling load, and compression greater than the buckling load. The GROMs in the upcoming numerical studies were generated using a shortening end displacement of 0.1% of the beam length. Furthermore, δ_u^{tr} used for the identification need not be equal to the value of δ_u used in the subsequent analysis of the GROM.

3.4 Numerical case study

3.4.1 Test problem

Buckling of the beam is achieved by prescribing a horizontal end displacement of δ_u. The initial strain ε_0 is equal to zero. The beam used for study has a thickness $t = 0.787$ mm, cross-sectional width $b = 12.7$ mm, length $L = 228.6$ mm, Young's modulus $E = 153.4$ GPa, and density $\rho = 7567$ kg-m^{-3}. These physical parameters have been used in the literature [53]. The beam is loaded with a nearly uniform, downward load, with a small eccentricity to induce asymmetric snap-through. The mean intensity of the reference load is 0.015 N/mm downward, and it has an intensity of 5% less than the mean at the left end and 5% greater than the mean at the right end. The model geometry is shown in Fig. 3.2, and the model loading is shown in Fig. 3.3.

The arc-length method will be used as a tool to study the load-displacement response of the structural models studied herein by computing the SEPs of the models. The SEP of

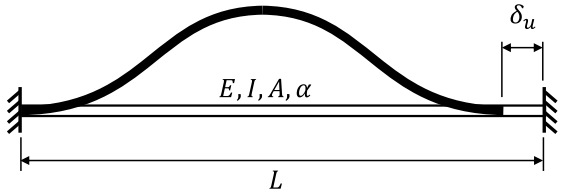

Figure 3.2: Model geometry

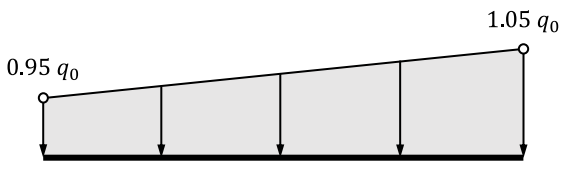

Figure 3.3: Model loading

a structural model contains the set of static equilibrium configurations encountered by the structure for a given load pattern, as well as the load factors necessary to maintain those equilibrium configurations. The arc-length method allows for equilibrium configurations to be computed in unstable regions of the response that a load-controlled quasi-static geometrically nonlinear analysis would fail to capture [46]. The SEPs computed using the arc-length method will be used to assess the quality of the fit of the reduced-order models to the truth model, which is introduced in the upcoming section.

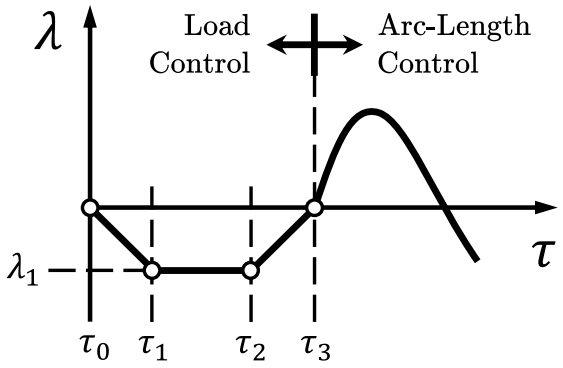

Figure 3.4: End displacement phases

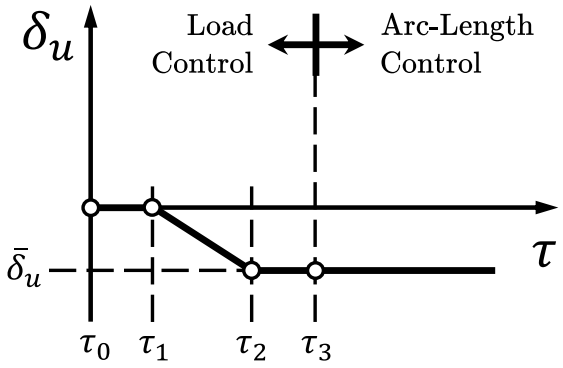

Figure 3.5: Load factor phases

Prior to analyzing the structure using the arc-length method, several load-controlled steps are used to induce a post-buckled configuration with zero transverse load and are illustrated in Figs. 3.4-3.5. The beam model begins unloaded with $\delta_u = 0$. The load factor λ is linearly ramped to a value λ_1 while δ_u remains zero. Then with λ held constant at λ_1, δ_u is ramped to a value of $\overline{\delta}_u$. Holding $\delta_u = \overline{\delta}_u$, the load factor λ is ramped back down to zero. Then, the arc-length analysis begins. These phases are illustrated graphically in Figs. 3.4-3.5, which show the values of δ_u and λ with respect to pseudo-time τ. The pseudo-time values τ_0, τ_1, τ_2, and τ_3 represent the boundaries between the load steps. All SEPs shown in the results section begin after τ_3.

3.4.2 Model development

The FEM (CRT64E) is a Co-RoTational (CRT) frame model with 64 equal-length elements consistent with the formulation in [21]. Linear Euler-Bernoulli beam elements were used as the local elements embedded in the , and shear deformations are assumed to be negligible. The axial displacements, transverse displacements, and rotations of the two end nodes are restrained to represent clamped boundary conditions. The horizontal displacement of the right-end node can be prescribed to induce buckling. This model is used as the primary base model for the identification of NLROM stiffness coefficients, and it is treated as the truth model for large-deformation physics.

The CVK model is implemented using both a 64-element FEM mesh (CVK64E) and a 10-mode continuous basis (CVK10M). The choice of a continuous basis will be explained in the upcoming Subsection 3.4.3, and the integrals of Eq. (3.21a-d) are evaluated numerically. A 10-mode projected CRT model (PRCRT10M), which is a CRT FEM with its residual vector and tangent stiffness matrix reassembled and projected onto the modal basis during each iteration step, as described in Eq. (2.5) and the associated paragraph, is analyzed. A 10-mode GROM (GROM10M) and a 10-mode NLROM (NLROM10M) are also analyzed. The PRCRT10M, GROM10M, and NLROM10M all use the first 10 linear vibration mode shapes of the CRT FEM as a transverse basis. The GROM10M was constructed using a compressive δ_u^{tr} of 0.1% of the beam length, though as stated in Subsection 3.3.2, the GROM parameters are not highly sensitive to the choice of δ_u^{tr}. The coefficients of the NLROM were determined using the procedure outlined in Subsection 3.3.1. Each applied displacement shape, derived from a combination of the mode shapes, was scaled to a maximum transverse displacement of one beam thickness (0.787 mm). For the single-mode tests, the modal amplitudes q_n^b and q_n^c were determined such that $q_n^b = -q_n^a$ and $q_n^c = 0.5q_n^a$. It is the authors' observation that the NLROM parameters are not highly sensitive to scaling of the applied shapes in the case of flat beams but that amplitudes on the order of one beam thickness is suitable for thin structures.

3.4.3 Modal basis

In this study, both the condensed von Kármán smooth Ritz model and the NLROM will use the linear Euler-Bernoulli vibration mode shapes as the basis for the transverse motion. The analytical Ritz solutions will use the smooth functions, while the NLROMs will use the Eigenvectors of the CRT FEM, which closely approximate the values of the smooth mode shapes at the nodal locations. It is more common to use the mode shapes of the discretized finite element model as a basis for the NLROM than it is to use a prescribed analytical shape, though both methods are acceptable. The linear vibration mode shapes $\phi_n(x)$ can be written as [53]

$$\phi_n = \alpha_n \left[\sinh\left(\beta_n x\right) - \sin\left(\beta_n x\right) - \zeta_n \left(\cosh\left(\beta_n x\right) - \cos\left(\beta_n x\right)\right)\right] \tag{3.33}$$

with

$$\zeta_n = \frac{\cosh\left(\beta_n x\right) - \cos\left(\beta_n x\right)}{\sinh\left(\beta_n x\right) + \sin\left(\beta_n x\right)} \tag{3.34}$$

and $\beta_n L$ the roots of

$$\cos\left(\beta_n L\right)\cosh\left(\beta_n L\right) = 1\,. \tag{3.35}$$

The parameter α_n is an artificially-imposed scaling factor so that the maximum absolute value of the function on the domain is one. The finite element mode shapes were similarly normalized by the maximum absolute transverse nodal displacement. The relatively large values attained from the hyperbolic sine and cosine functions as β_n increases make it difficult to evaluate the analytical functions. Therefore, in this study, all integrals involving the vibration mode shapes are evaluated numerically.

3.4.4 Results of the post-buckled beam analyses

For context, the SEPs attained for the models using the arc-length method are presented in the following way. The vertical axis represents the load factor, which scales the reference load vector $\overline{\mathbf{F}}$ applied to the models. This reference load is the asymmetric distributed load defined in Subsection 3.4.1 with a mean intensity of 0.015 N/mm downward. The horizontal

axis represents the transverse displacements of the models at the midpoint and the quarter points of the beam. All displacements of a given model are plotted with a common line style, with the exception of Fig. 3.6, which provides a distinction between the 1/4 point, midpoint, and 3/4 point. After achieving the first limit load, which is the first local maximum of the load value encountered on the SEP, the load factor decreases along with the midpoint deflection, and the load-displacement curve for the midpoint of the beam passes through the origin. Each time the load factor turns from negative to positive, a new "cycle" begins. In other words, the load factor initially increases to the limit load and then decreases to a negative value. Once the load factor crosses zero again, the first cycle is complete.

Prior to assessing the quality of the GROM, the range of applicability of the CVK theory with respect to post-buckling rise was explored numerically by examining the behavior of

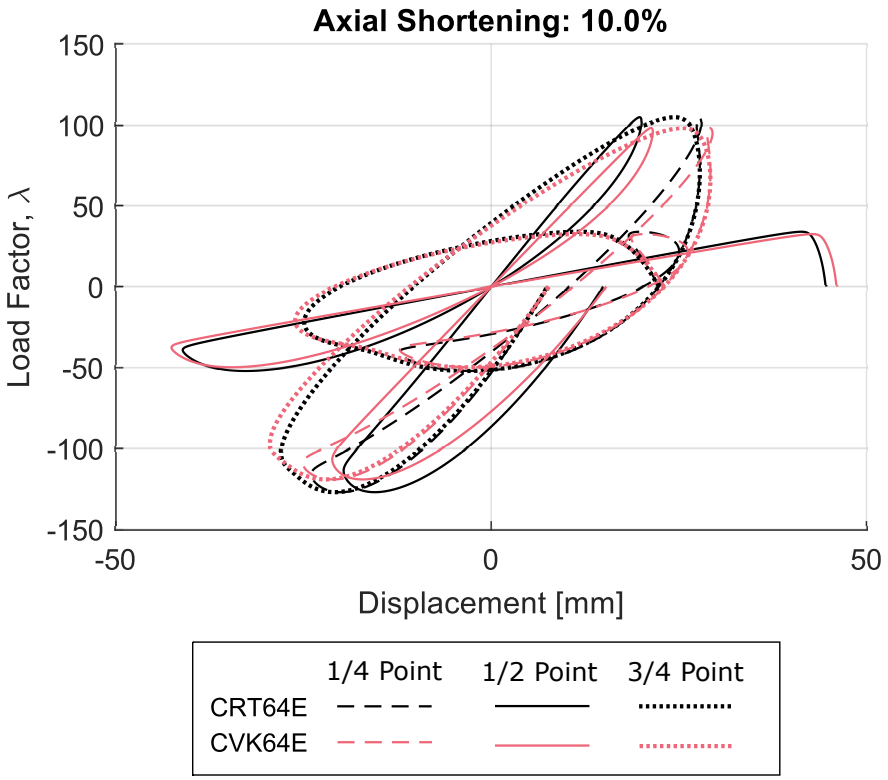

Figure 3.6: Condensed von Kármán model response at large 10.0% axial shortening.

the model at increasing end shortening values. In this specific application, increasing the end shortening magnitude resulted in a CVK model that was generally softer than the truth model by small amounts, leading to slightly lower load factors and larger deflections. This indicates that the CVK model may begin to underestimate the load required to induce snap-through if it is pushed to a very large post-buckled rise. Figure 3.6 shows the response of a 64-element CVK model plotted with the response of the truth model for a large end shortening of 10% of the beam length. This end shortening value is large, and it leads to an unloaded post-buckled rise of 19.5% of the beam length. This shows the CVK theory to be stable up to very large end shortening values.

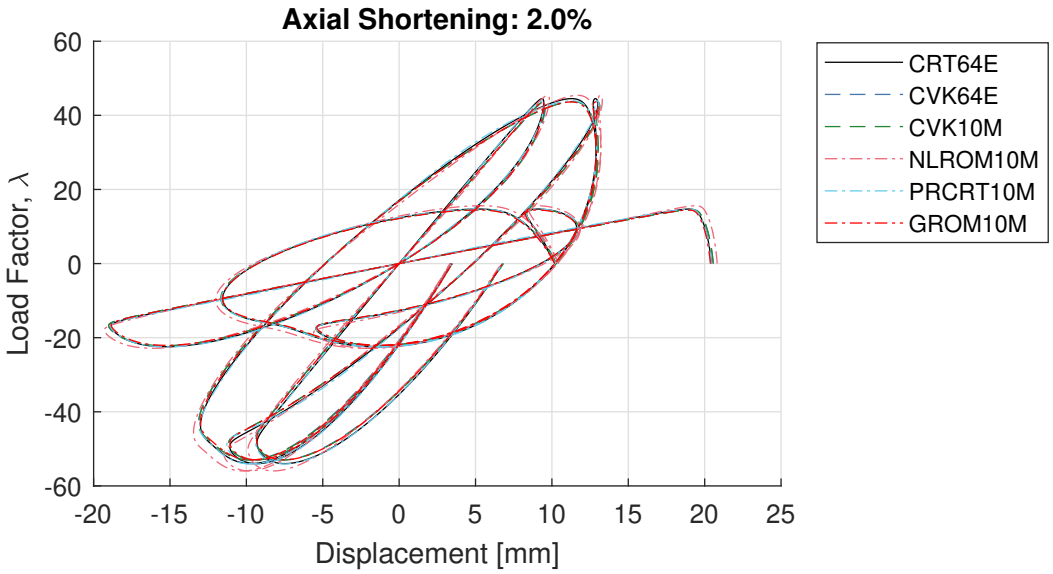

Figure 3.7: Comparison of the SEPs of all models.

Figure 3.7 shows the response of all models at an end shortening of 2%. The 10-mode projected CRT FEM has the closest fit and is nearly indistinguishable from the truth model through the initial asymmetric snap-through. The other models approximated the SEP of the truth model with varying degrees of accuracy, but the quality of the fit depended on the specific displacement configuration. Qualitatively, it appears that the GROM and

both CVK models produced similar accuracy, having slightly underestimated the initial limit load. The GROM provided a marginally better approximation of the unloaded, post-buckled displacement field than either of the CVK models, though the models are comparable. In contrast, the NLROM provided a notable overestimate of both the initial limit load and the unloaded, post-buckled displacements.

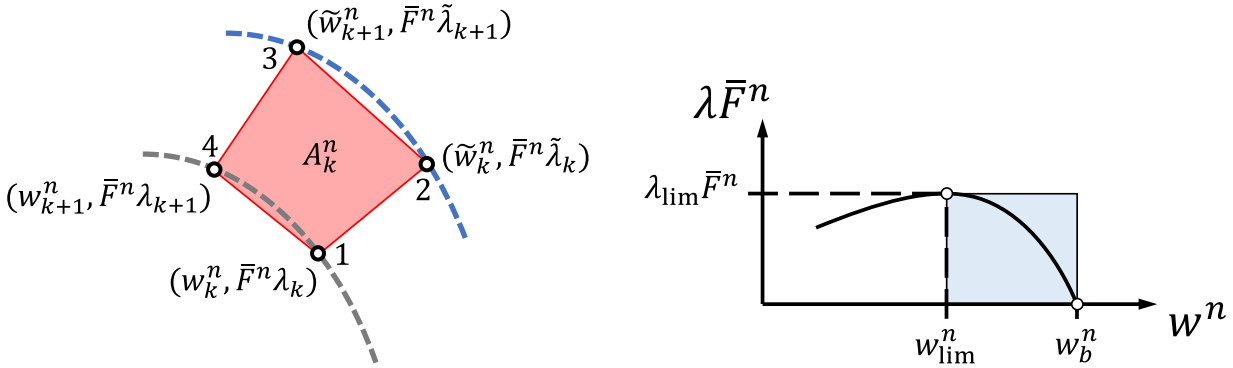

(a) Error metric illustration

(b) Error metric normalization

Figure 3.8: Error metric and normalization

An error metric was needed to adequately characterize the goodness of fit of the ROMs relative to the truth model. Comparing the stiffness coefficients term-by-term can be problematic, since the effects of individual terms on the resulting restoring force are highly variable and dependent on the mode of excitation. Instead, accuracy of a ROM can be interpreted as the closeness with which the ROM reproduces the SEP. A ROM with zero error would exactly reproduce every load-displacement pair in the SEP of the truth model. Any deviation in either the force or the displacement at a given arc-length step should contribute some error. The "average" error was described by evaluating the area between the SEP of each ROM and that of the truth model. The arc-length analysis computes discrete steps, and a contribution to the total error is computed for each step. The error metric concept is illustrated in Fig. 3.8a. Let k and $k+1$ represent two adjacent steps in the arc-length

analysis. Let w_k^n and λ_k be the node n deflection and load factor for the truth model, and let $\tilde{w}_k^n$ and $\tilde{\lambda}_k$ be the node n deflection and load factor for the approximate model. The vector component $\overline{F}^n$ is the transverse reference load at node n. The error accumulated between steps k and $k+1$ is the area of the quadrilateral formed between the four points shown in Fig. 3.8a. The total area has units of work and can be computed as

$$A_k^n = \tfrac{1}{2}\|\mathbf{v}_{12} \times \mathbf{v}_{13}\| + \tfrac{1}{2}\|\mathbf{v}_{13} \times \mathbf{v}_{14}\| \,. \tag{3.36}$$

where $\mathbf{v}_{12}$, $\mathbf{v}_{13}$, and $\mathbf{v}_{14}$ are vectors connecting the two points (from Fig. 3.8a) denoted in the subscript. Note that the total error accumulated between steps k and $k+1$ is the sum of all the nodal contributions n, and not just the midpoint and quarter-points.

Due to the scale of the SEP increasing on both axes (displacement and load factor) with increasing end-shortening values, a normalization technique was desired to make the error unitless. Because the area between the SEPs has units of work, a "characteristic work" was computed for each end shortening value, equal to $\lambda_{\text{lim}}\,\overline{\mathbf{F}} \cdot (\mathbf{u}_{\text{lim}} - \mathbf{u}_b)$, where λ_{lim} is the load factor of the CRT FEM at the first limit point, $\overline{\mathbf{F}}$ is the reference load vector, $\mathbf{u}_{\text{lim}}$ is the vector of nodal displacements of the CRT FEM at the first limit point, and $\mathbf{u}_b$ is the vector of nodal displacements of the CRT FEM in the unloaded, post-buckled configuration (at time $\tau = \tau_3$). The total area accumulated for each ROM was divided by this characteristic value, which represents the work done by the limit load at the limit point. The shaded area in Fig. 3.8b is the contribution to the characteristic work from node n.

Figure 3.9 shows the error trends of the models with respect to end shortening. The end shortening values were sampled between 0.1% and 2.0%. The projected CRT FEM (PRCRT10M) theoretically provides a lower bound on the ROM error, due to it being the exact restoring force of the CRT FEM projected onto the modal basis. The error in the PRCRT10M response reflects the ability of the modal basis to span the solution space. The 10-mode Ritz solution to the CVK model slightly outperformed its 64-element counterpart by a small, consistent margin. At small end shortening values, the PRCRT10M model and the GROM10M model had approximately the same error, both in the case of one cycle and

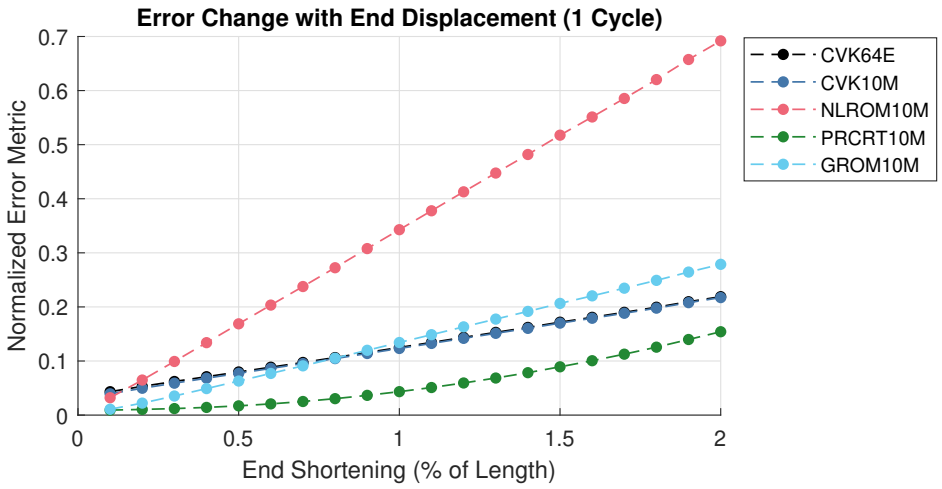

(a) Total error, 1 cycle

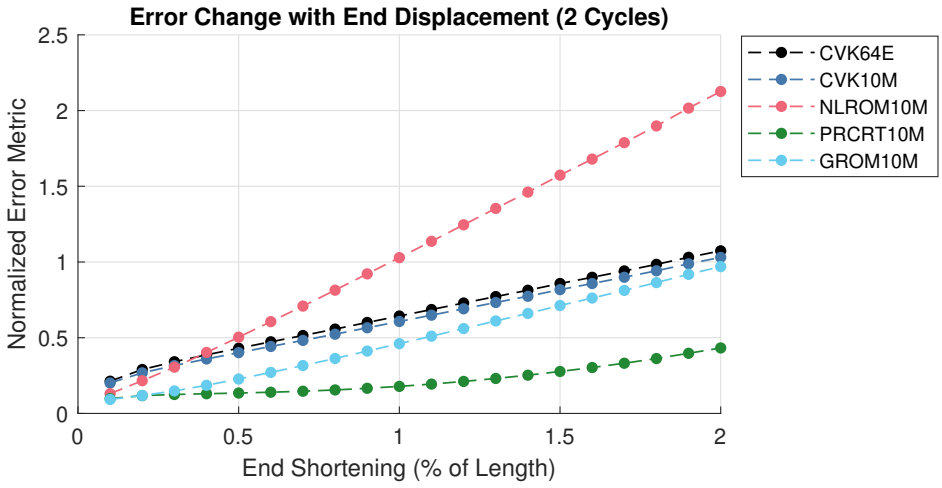

(b) Total error, 2 cycles

Figure 3.9: Error values over 1 and 2 cycles

two cycles. The GROM10M error gradually diverged from that of the PRCRT10M model, slightly exceeding the error of the CVK models over one cycle and approaching the error of the CVK models over two cycles. The NLROM error, while being slightly lower than that of the CVK models at the smallest end shortening value, increased rapidly relative to the other models as the magnitude of the end displacement increased.

An intriguing observation is that the GROM, while built from the CRT FEM using observations from the CVK theory, outperformed the corresponding CVK models by some metrics. Namely, for end displacements less then 0.8% of the length, the GROM had less error than the CVK models over one cycle, and over two cycles, the GROM had lower error than the CVK models for all studied end displacements. This suggests that the tangent stiffness matrices generated by the CRT FEM may provide higher quality information for the identification of a cubic model than the analytically derived matrices. Additionally, for relatively small end shortening values (less than approximately 0.3%-0.4%), the GROM nearly matches the accuracy of the PRCRT10M model over two cycles. So, the two-step identification process used to compute the GROM coefficients is computationally inexpensive, and the accuracy of the resulting model exceeds that of the analytically-derived CVK models in certain situations.

A valid concern in such an error analysis involving models with identified parameters such as the GROM and NLROM is the potential for error in the identification process. Recall that the GROM parameters are not sensitive to the selection of δ_u^{tr} in the identification, and that the NLROM parameters are not sensitive to the selection of modal amplitudes during the identification phase when the STEP is utilized [6, 26]. Due to these factors, this error analysis should provide a fair comparison between the considered reduced-order modeling techniques.

3.5 Conclusions

This chapter presented an overview of reduced order modeling techniques used in the structural mechanics community. The equivalence between the condensed von Kármán model and the NLROM was demonstrated, and the equivalent NLROM coefficients were solved for from the condensed von Kármán model. A procedure was developed for identifying the equivalent CVK matrix and vector parameters from a general finite element beam model, and the resulting model was shown to be more accurate than the condensed von Kármán model with the same number of modes, for end shortening values less than 0.8% of the beam length. The error metric developed for the study provided an estimate of the goodness-of-fit that matched the qualitative assessment of the SEP accuracy. The GROM appeared to outperform the NLROM for all end displacement magnitudes studied, suggesting that for the specific case of initially straight, post-buckled beams, the generality of the NLROM restoring force function may not provide significant benefit over the simpler GROM restoring force.

Chapter 4

ADDRESSING STABILITY ISSUES IN THE IDENTIFICATION OF NONLINEAR REDUCED-ORDER MODELS FOR SNAP-THROUGH OF CURVED BEAMS

4.1 Introduction

4.1.1 Overview

There is a limited body of research on reduced-order modeling of curved beams [5, 37, 43], and an even smaller body of work on reduced-order modeling of snap-through in curved beams [2,46,50]. In [50], the post-snap-through center displacement was accurately captured with a 13-transverse mode IC model. That study found that modal enrichment aided in the convergence to the correct snap-down center displacement, but few details were provided on the training data generation. In [2], a model was identified by superimposing displacement test cases on top of the snap-down configuration in addition to the undeformed configuration. This model was able to accurately capture the displacement field after snap-through for several load levels. However, the numerical validation study was limited to verifying the snap-down displacement configuration using static analysis under several load levels, and only symmetric modes were used in the construction of the NLROM. Consequently, the accuracy of the NLROM during the snap-through process was not investigated. The authors of [2] point out that the quadratic and cubic stiffness coefficients are highly sensitive in the vicinity of the undeformed configurations. In [46], a similar improvement in the snap-through response was achieved with an IC model by scaling the applied forces during identification such that the FEM was forced into the snap-down configuration in some test cases. This resulted in a training data set that included both snapped and unsnapped configurations. The models generated in that study were validated by computing the Static Equilibrium

Path (SEP) using the arc-length method, and so the mid-snap-through load-displacment response was able to be validated.

While properly implemented NLROMs can be very efficient due to the small number of DOFs and the simplicity of the restoring force function, the number of parameters in the NLROM restoring force function increases quartically with the number of modes. This leads to an increase in both the storage space required for the parameters and the number of test cases required for identification. In [47], the authors implement the Least Absolute Selection and Shrinkage Operator (LASSO) method to simultaneously identify restoring force parameters and eliminate coefficients with low participation. The approach was able to significantly reduce the number of ROM parameters while maintaining acceptable model accuracy.

4.1.2 Study framework

This chapter aims to diagnose the challenges associated with identifying non-intrusive NLROMs of beams with shallow curvature and address those challenges by expanding on the idea of enriching training data with additional displacement configurations. The concept introduced in [2] of identifying NLROMs using additional base configurations is expanded upon by (i) considering a wider array of configurations, including mid-snap-through configurations, (ii) generating an implicitly condensed model, and (iii) validating the improved ROMs by looking at the SEP determined using the arc-length method. Specifically, seven base configurations are used for ROM identification in various combinations, including those before, during, and after snap-through. The fit quality of each ROM is characterized for every configuration along the SEP using an error metric, so improvements in the fit quality local to a specific configuration can be observed.

In addition to identifying NLROMs using these techniques, a new approach is proposed which uses the functional form of the restoring force of a Condensed Von Kármán (CVK) beam model as the basis for a non-intrusive identification. The matrix form of the CVK governing equation is presented, and a fitting procedure is proposed by which the parameters

that have traditionally been derived analytically using the physical parameters of the beam are instead identified from an FEM. A model identified in this way is referred to as a Guided Reduced-Order Model (GROM). The GROM restoring force contains fewer parameters than that of an NLROM for a model with the same number of DOFs. For the purposes of this article, the term ROM will be used to refer to both NLROMs and GROMs.

Several limitations are placed on the scope of this work. First, the ROMs considered in the study use a modal basis constructed from the linear vibration mode shapes of a flat beam. This same approach was used successfully for curved beams in [50], and the flat basis provides satisfactory displacement convergence for the initial beam curvatures considered herein. This research will not compare the rate of convergence of the flat versus curved bases with respect to modal enrichment. Second, statically condensed models in the literature have been used to model curved beams with initial curvatures comparable to those studied herein [5]. Therefore, this article will not investigate the applicability of static condensation assumptions, and the axial component of the inertia will be neglected. Third, the most complex aspect of non-intrusive ROMs is the restoring force identification, as the projected mass and damping matrices should not vary for a given structural model and modal basis. Consequently, this study will limit its model validations to quasi-static arc-length analysis, and the fit quality of the ROMs will be assessed by computing the error in the restoring force along the SEP.

4.1.3 Chapter outline

Section 4.2 extends the guided identification concept introduced in 3.3.2 to allow for the least-squares identification of parameters.

Section 4.3 describes the models used in the study. Subsection 4.3.1 presents the structural model and its geometry, material parameters, and loading. Subsection 4.3.2 describes the numerical models used to solve the structural problem, including details about the FEMs and the ROMs. Subsection 4.3.3 explains the modal basis used for the ROMs.

Section 4.4 discusses the generation and analysis of ROMs of curved beams. Subsec-

tion 4.4.1 reviews some of the common issues encountered when identifying ROMs of curved beams, and numerical examples are provided. Subsection 4.4.2 investigates the source of identification issues using a Taylor series expansion of the FEM restoring force function. Subsection 4.4.3 discusses the concept of additional base configurations during ROM identification. Subsection 4.4.4 reports the results of the numerical studies on curved beam ROMs and presents an error analysis.

Section 4.5 states the conclusions of the study.

4.2 Guided identification via von Kármán restoring force format

An M-mode NLROM with a full cubic polynomial restoring force of the form of Eq. (2.6) contains $O(M^4)$ unique parameters, making modal enrichment costly both in terms of storage space and the required number of tests per training set. Thus, there exists an incentive to decrease the number of parameters in a ROM that need to be identified. Shallow von Kármán beam and shell theory has been used successfully for thin structures with shallow curvature [8, 9].

Referring to Section 3.2, by setting the initial axial strain $\varepsilon_0 = 0$ in Eq. (3.19), the governing equation of the condensed shallow von Kármán beam can be written as

$$(EIw'')'' - \overline{k}_a \left(\delta_u + \int_0^L \left(h'\, w' + \tfrac{1}{2}(w')^2 \right) dx \right) (h'' + w'') - q = 0\,. \tag{4.1}$$

The Galerkin method can be applied, interpolating the transverse displacement as $w \approx \sum_i \phi_i(x)\, q_i$, where $i \in \{1,\, M\}$, q_i is the i-th element of the vector of modal displacements $\mathbf{q}$, and $\phi_i(x)$ is the i-th interpolation function. This yields the governing equation of the approximation

$$\mathbf{Kq} + \left(\sqrt{\overline{k}_a}\, \delta_u + \mathbf{c} \cdot \mathbf{q} + \tfrac{1}{2}\mathbf{q} \cdot (\mathbf{Bq}) \right) (\mathbf{c} + \mathbf{Bq}) - \mathbf{f} = \mathbf{0}\,, \tag{4.2}$$

where the parameters $\mathbf{K} \in \mathbb{R}^{N \times N}$, $\mathbf{B} \in \mathbb{R}^{N \times N}$, $\mathbf{c} \in \mathbb{R}^N$, and $\mathbf{F} \in \mathbb{R}^N$ are defined as

$$K_{ij} = \int_0^L EI(x)\, \phi_i''(x) \phi_j''(x)\, dx \qquad\qquad f_i = \int_0^L \phi_i(x) q(x)\, dx \tag{4.3a,b}$$

$$B_{ij} = \sqrt{\overline{k}_a} \int_0^L \phi_i'(x)\phi_j'(x)\,dx \qquad\qquad c_i = \sqrt{\overline{k}_a} \int_0^L h'(x)\phi_i'(x)\,dx\,. \tag{4.3c,d}$$

Equation (4.2) contains just $O(M^2)$ unique parameters, which is a significant reduction from the $O(M^4)$ parameters required for the traditional NLROM restoring force.

This beam model accounts for non-prismatic cross-sectional profiles, post-buckling effects, and shallow initial curvatures. This provides a framework that can theoretically model a wide array of thin structures that can be approximated as a beam. As presented in Eq. (4.3), the parameters $\mathbf{K}$, $\mathbf{B}$, $\mathbf{c}$, and $\overline{k}_a$ can computed analytically provided $EI(x)$, $EA(x)$, and $h(x)$ are all known. It is here proposed that a restoring force of this form can be used as the basis of a non-intrusive ROM identification. Rather than being computed analytically, these parameters are identified from a series of static solutions of an FEM, as is done to identify NLROMs. Because this restoring force function is built upon the governing equations of a curved von Kármán beam instead of general 3D elasticity, the problem is more heavily constrained, and there are fewer total parameters than in an NLROM for the same number of DOFs. Recall that a ROM identified in this way will be called a guided reduced-order model (GROM).

The GROM restoring force is linear with respect to $\mathbf{K}$, as it is with $\mathbf{K}^{(1)}$, $\mathbf{K}^{(2)}$, and $\mathbf{K}^{(3)}$ in the traditional NLROM restoring force. However, the GROM restoring force is also quadratic with respect to $\mathbf{B}$ and $\mathbf{c}$, meaning that a least-squares minimization of the error in the restoring force is no longer a quadratic problem. Nonlinear optimization methods must be applied in order to solve for the GROM parameters. In this study, the GROM parameters will be identified using a least-squares minimization of the error in the modal restoring force. For a test case p, the residual term $\mathbf{r}^p$ is equal to

$$\mathbf{r}^p = \mathbf{K}\mathbf{q}^p + \left(\sqrt{\overline{k}_a}\,\delta_u + \mathbf{c}\cdot\mathbf{q}^p + \tfrac{1}{2}\mathbf{q}^p\cdot(\mathbf{B}\mathbf{q}^p)\right)(\mathbf{c} + \mathbf{B}\mathbf{q}^p) - \tilde{\mathbf{F}}^p\,, \tag{4.4}$$

and the parameters $\mathbf{K}$, $\mathbf{B}$, and $\mathbf{c}$ are selected to minimize the objective function $\sum_p \mathbf{r}^p\cdot\mathbf{r}^p$, subject to the symmetry constraints $K_{ji} \equiv K_{ij}$ and $G_{ji} \equiv G_{ij}$.

It is proposed that the identification procedure proceed using two separate least-squares solutions. In the first solution, the value of δ_u is set to zero in Eq. (4.4). This will eliminate

$\overline{k}_a$ from the equation, allowing for the identification of $\mathbf{K}$, $\mathbf{B}$, and $\mathbf{c}$. Even though $\overline{k}_a$ is still unknown after this step, the effects of the axial stiffness are implicitly included in $\mathbf{B}$ and $\mathbf{c}$ (see Eq. (4.3c,d)). The resulting model is sufficient to represent a curved beam with fixed supports and no horizontal end displacement, and $\overline{k}_a$ does not need to be determined if post-buckled response is not desired.

Once $\mathbf{K}$, $\mathbf{B}$, and $\mathbf{c}$ are determined from the test cases with $\delta_u = 0$, a trial value of δ_u, termed δ_u^{tr}, is applied to the model, and an additional set of test cases is applied to the FEM. Because δ_u^{tr} is nonzero, $\overline{k}_a$ reenters the equation and can be solved for. While no numerical studies are reported with a nonzero value of δ_u, models were successfully generated with a small negative value of δ_u^{tr} on the order of 0.1% of L. Due to the initial curvature in the beam, applying δ_u^{tr} to the model results in some transverse deflection, even though the beam is not loaded transversely. In the generation of these models, it was observed that centering the test cases about the unloaded configuration resulting from the application of δ_u^{tr} generally provided the best results (as opposed to the undeformed configuration). The unloaded, post-buckled equilibrium configuration was computed using the FEM, and then the transverse displacements of that configuration were projected onto the modal basis. Finally, the displacement test cases described in Subsection 2.1.2 were superimposed upon that post-buckled configuration.

Given the new training set with $\delta_u = \delta_u^{tr}$, a second least-squares solution can be used to solve for $\overline{k}_a$, using the now known parameters $\mathbf{K}$, $\mathbf{B}$, and $\mathbf{c}$. The value of $\overline{k}_a$ that minimizes the objective function $\sum_p \mathbf{r}^p \cdot \mathbf{r}^p$ can be solved for analytically as

$$\overline{k}_a = \left(\frac{\sum_p (\mathbf{B}\mathbf{q}^p + \mathbf{c}) \cdot \mathbf{R}^p}{\delta_u^{tr} \sum_p (\mathbf{B}\mathbf{u}^p + \mathbf{c}) \cdot (\mathbf{B}\mathbf{u}^p + \mathbf{c})} \right)^2 \tag{4.5}$$

This step completes the identification of the GROM parameters.

4.3 Model details

4.3.1 Structural model

The physical model studied is a thin beam with a uniform initial curvature corresponding to a radius R. The value of R is varied during the study. The beam has a projected length L of 457.2 mm (18.0 in), which is the distance between the supports, and a maximum rise h_0 consistent with the radius of curvature. The cross-section is rectangular with a width of 25.4 mm (1.0 in) and a thickness of 2.286 mm (0.09 in). The material of the beam has an elastic modulus of 73.08 GPa (10.6×10^6 psi), a shear modulus of 27.58 GPa (4.0×10^6 psi), and a density of 2765.8 kg/m^3 (2.588×10^{-4} lb-s^2/in^4). The properties are summarized in Table 4.1, and the problem geometry is presented in Fig. 4.1. This structure has been well-studied in the literature [2, 5, 37, 43, 50]. Two separate structural models will be studied

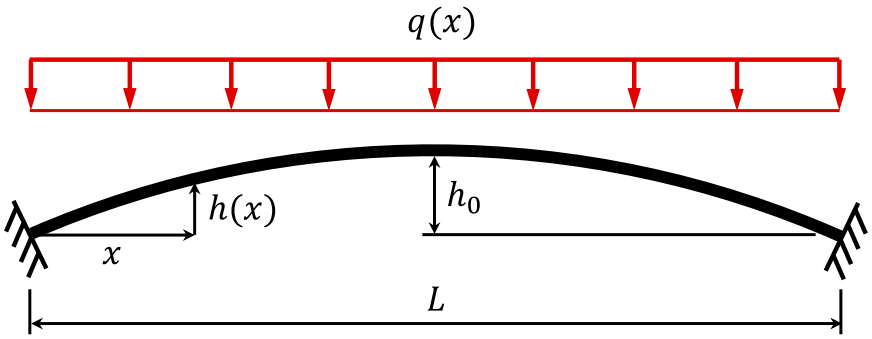

Figure 4.1: Test problem geometry for numerical studies

in this article, differing only in their radii of initial curvature (or arch heights). Model A has a radius of 2063.75 mm (81.25 in), corresponding to an arch height of 12.7 mm (0.5 in), or $L/36$. This is the most common radius of curvature in the literature to be paired with the previously state problem parameters. Model B has a radius of 1154.43 mm (45.45 in), corresponding to an arch height of 22.86 mm (0.9 in), or $L/20$.

The reference load is a linearly-distributed load with a mean intensity of 0.1751 N/mm (1.0 lb/in) downward. The intensity is per unit projected length. The load is given a slight

asymmetry to induce asymmetric snap-through, having 95% of the mean intensity at the left end and 105% of the mean intensity at the right end. The load factor, λ, depicted in upcoming load-displacement plots, is a scaling factor on this reference load.

Table 4.1: Physical properties of the curved beam

Length	Section Width	Thickness	Young's Modulus	Density
457.2 mm	25.4 mm	2.286 mm	73.08 GPa	2765.8 kg / m^3

4.3.2 Numerical models

Finite Element Models (FEMs) consisting of 2-D co-rotational beam elements after the formulation in [21] were used (i) as the truth models for the static load-displacement response and (ii) as the models from which the ROMs were identified. The beam elements within each co-rotational frame were straight, linear Euler-Bernoulli beam elements. The FEM had 64 straight elements of equal projected length, and thus the nodes had equidistant spacing in the x-direction. The y-coordinates of the nodes were specified to achieve the initial curvature. The x-displacement, y-displacement, and rotation DOFs of the end nodes were restrained to represent clamped boundary conditions. Two FEMs were constructed, with FEM_A corresponding to Model A and FEM_B corresponding to Model B.

4.3.3 Modal basis

All ROMs in this study (NLROM and GROM) use the linear vibration mode shapes from a flat Euler-Bernoulli beam. The discrete mode shapes were attained by computing the Eigenvectors of a 64-element beam model constructed from linear, Euler-Bernoulli beam elements and normalizing the mode shapes by the maximum absolute displacement. The transverse basis included the first six vibration mode shapes, shown in Fig. 4.2, including three symmetric modes and three asymmetric modes. Because an implicit condensation

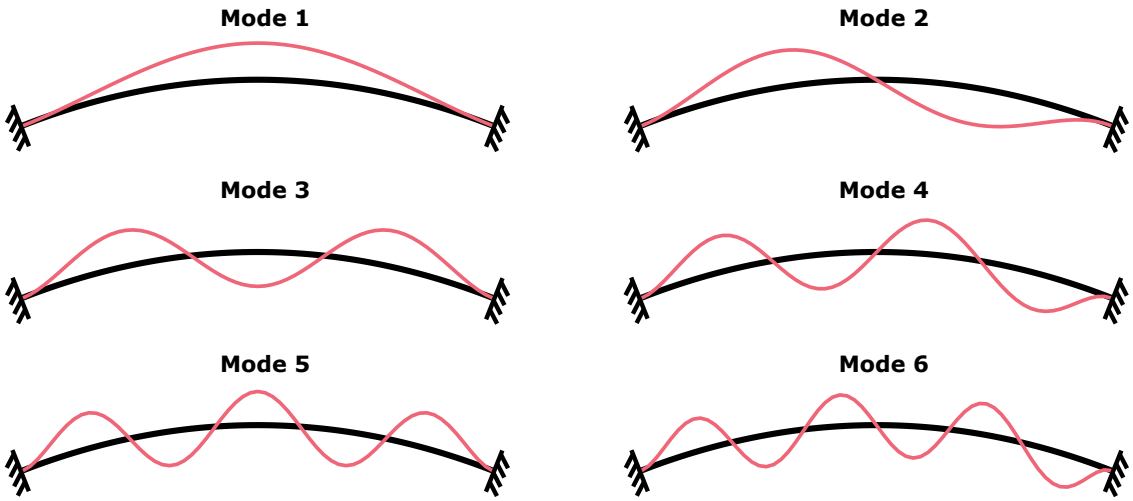

Figure 4.2: ROM mode shapes for curved beam models

approach was used, no membrane basis was needed. It was observed that the mode shapes of the flat beam model provided a satisfactory basis for the displacements of the curved beam. The flat beam modes were also used to construct NLROMs of a curved beam in [50] and [2]. Using the mode shapes of the flat beam also allowed a single basis to be used for the identification of both Model A and Model B.

4.4 Curved beam identification

4.4.1 Common challenges in identification

It has been suggested that in the case of beams with significant initial curvature, NLROMs have often failed to accurately capture snap-through behavior and sometimes lack numerical stability [46, 50]. This observation was confirmed in preliminary studies as part of this investigation. It was observed that generating training sets by applying displacements about the undeformed configuration commonly results in models that are inaccurate beyond the first limit point that immediately precedes snap-through. It has also been observed that in these models, the large-deformation behavior is extremely sensitive to small modifications to the test cases contained in the training sets, confirming the findings in [2].

To illustrate the sensitivity of NLROM large-deformation behavior to variations in test cases about the undeformed configuration, six training data sets were generated using random scaling factors for the modes. To create a single test case within a training set, a displacement field was generated by multipling each mode in the basis by a random number in the range $[-1, 1]$, and the resulting displacement field was scaled to yield a maximum transverse displacement of one-half a beam thickness (1.143 mm). Each training set contained the same number of test cases as the minimum number required by the STEP, and the NLROM and GROM parameters were solved for using least-squares. The SEP was computed for each of the 12 ROMs (6 NLROMs and 6 GROMs), and the load factor was plotted versus the transverse deflections of the quarter points and midpoint of the beam in Figs. 4.3a (NLROM) and 4.3b (GROM).

The plots reveal that the behavior of the NLROMs beyond the first limit point is highly variable between training sets, and all of the models generated diverged rapidly from the truth model beyond the first limit point. The GROMs, which were generated using the same six training sets used to generate the NLROMs, had far more consistent behavior in the large-deformation regime. While significantly improved, there remained some inconsistency in the load-displacement behavior of the GROMs after snap-through, where the GROMs tended to slightly underestimate the load factor in comparison with the truth model.

4.4.2 Taylor series expansion investigation

The restoring force function of an NLROM is identified to best approximate the restoring force of an FEM using the available NLROM parameters. If a cubic restoring force function is assumed, as it generally is, the NLROM restoring force is a cubic approximation of the FEM restoring force. The NLROM parameters are selected to provide the closest fit to the provided training data, so if test cases are clustered around a single displacement configuration, that configuration will be prioritized in the identification. It was assumed that training the NLROM restoring force function using test cases near the undeformed configuration would tend toward a cubic Taylor series expansion of the FEM restoring force centered at the

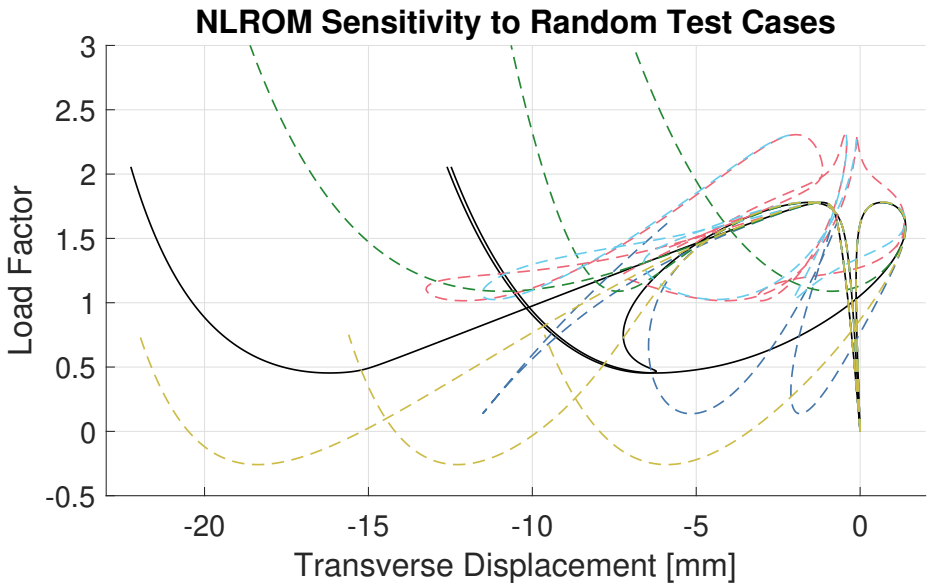

(a) SEPs of NLROMs

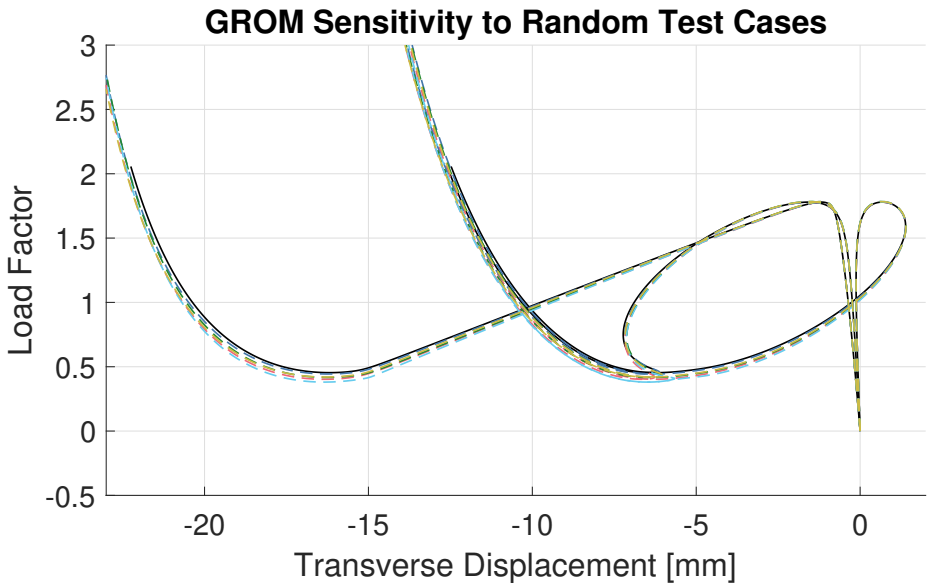

(b) SEPs of GROMs

Figure 4.3: SEPs of models non-intrusively identified using random displacements

undeformed configuration. Seeing as the NLROMs generated in this way failed to accurately capture the large-deformation behavior of the FEM, as shown in Fig. 4.3a, an analytical cubic Taylor series expansion of the FEM was desired. If the expansion were to closely or exactly approximate the FEM restoring force, then it would indicate that the FEM restoring force is strongly cubic and that the issues observed in Fig. 4.3a stem from the identification algorithm failing to approximate the cubic function numerically. If the cubic expansion were to fail to capture the large-deformation behavior of the FEM, it would appear that the FEM restoring force contains higher-order terms. A cubic Taylor series expansion of the internal force vector $\mathbf{f}^e$ of a CRT beam element (after the formulation in [21]) was computed analytically with respect to the generalized element displacement vector $\mathbf{u}^e$. The Taylor series expansion can be written as

$$\mathbf{f}^e(\mathbf{u}^e) \approx \mathbf{f}^e(\mathbf{0}) + \mathbf{f}^e_{,j}(\mathbf{0})u^e_j + \frac{1}{2}\,\mathbf{f}^e_{,jk}(\mathbf{0})u^e_j u^e_k + \frac{1}{6}\,\mathbf{f}^e_{,jkl}(\mathbf{0})u^e_j u^e_k u^e_l\,, \tag{4.6}$$

where $\mathbf{u}^e$ is the vector of nodal displacements and rotations, $\mathbf{f}^e(\mathbf{u})$ is the internal force vector of the CRT element, and a comma denotes partial derivatives with respect to the ensuing components of $\mathbf{u}^e$. Summation on repeated indices is assumed. This expansion represents the "best possible" cubic approximation of the FEM about the undeformed configuration, because it is derived analytically with respect to the nodal displacements. An NLROM identified using training data clustered solely about the undeformed configuration represents, effectively, a numerical approximation of this analytical expansion. Thus, using this Taylor series expansion as a basis for the study of the load-displacement response eliminates any possibility of numerical approximation error or training data dependency. Figures 4.4a-d compare the SEP of the Taylor series expansion to that of the FEM from which the expansion was computed for four different initial curvature heights.

The $L/100$ imperfection level yields a close fit, yet there is already a small amount of softening after snap-through. At a 2% imperfection height ($0.02L$), there is significant deviation from the truth model, but the expansion captures the important snap-through features. Between 2% and 3%, the approximation completely fails to recover any stiffening

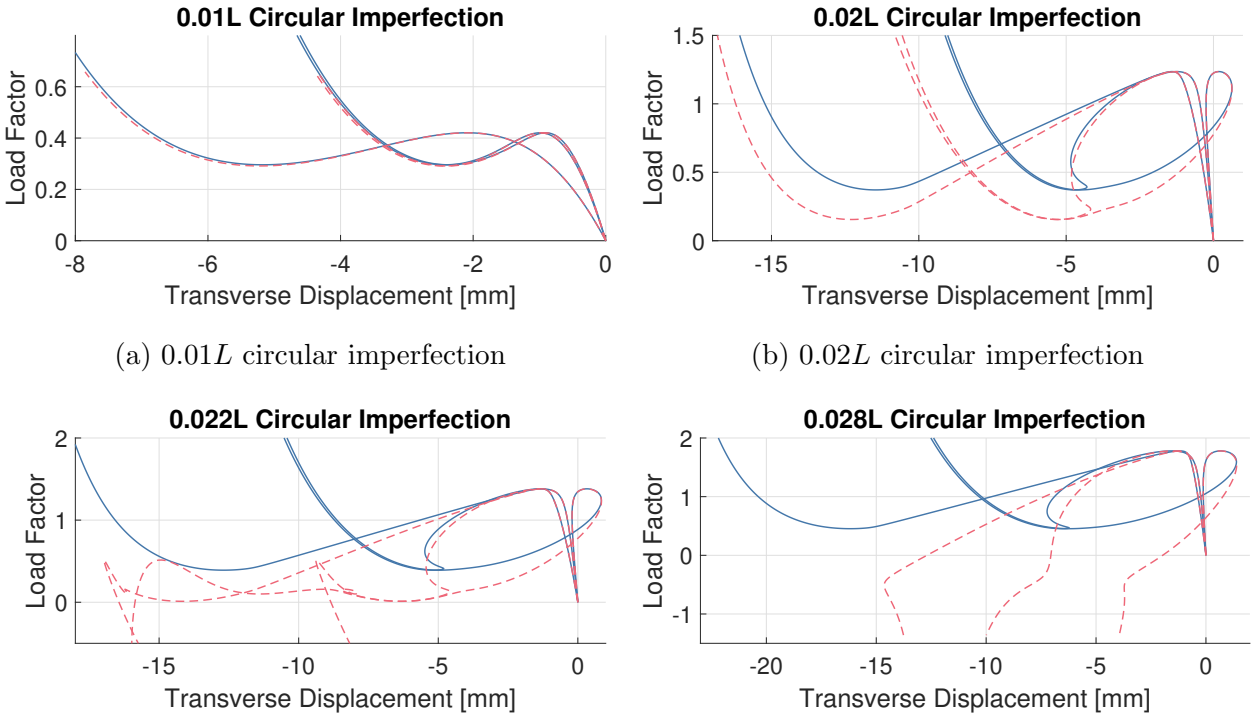

(a) $0.01L$ circular imperfection

(b) $0.02L$ circular imperfection

(c) $0.022L$ circular imperfection

(d) $0.028L$ circular imperfection

Figure 4.4: SEPs of Taylor series expansion ROMs

behavior following snap-through, and the expansion deviates from the truth model rapidly after the first limit point. This shows that, even if the derivatives of the restoring force with respect to the nodal displacements are computed exactly with no approximation error, the cubic information available in the vicinity of the undeformed configuration is insufficient to describe the large-deformation behavior. It was assumed that any discrepancies that existed in the cubic expansion would be made up for by the higher-order terms, but the coefficients of the higher-order terms still needed to be determined.

Additional terms of the Taylor series expansion were desired, but deriving the 4th and 5th-order terms analytically for a general element proved to be too intensive. The storage space required for the 5th-order coefficients of a 64-element model also would have been

prohibitively large. A simpler, 4-element co-rotational model was used for the convergence study. The equilibrium equations for the entire 4-element FEM were derived analytically, and then the coefficients of the 2nd through 5th-order terms were computed using a symbolic math engine. The 4-element mesh was very course and resulted in a stiffer model than did the 64-element mesh, but the important features of the snap-through behavior were still captured.

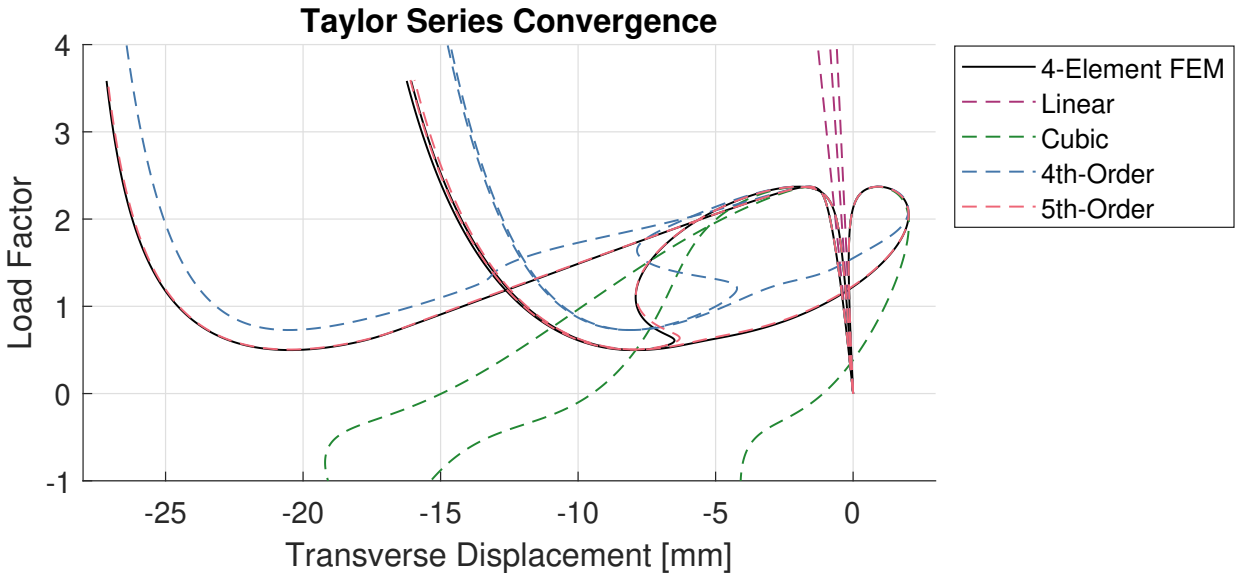

Figure 4.5: SEPs of Taylor series expansion ROMs of 4-element FEMs (0.03L)

At the L/36 imperfection height, the cubic Taylor series expansion of the 4-element FEM exhibits a similar pattern of divergence from the FEM observed with the cubic expansions of the 64-element mesh and the NLROMs generated about the undeformed configuration (as seen in Fig. 4.5). The approximation fails to stiffen after snap through, and the load factor appears to blow up to large negative values. The 4th-order expansion recovers the stiffening behavior after snap-through, but the accuracy is poor following the first limit point. The 5th-order expansion appears to be mostly converged to the FEM. Unsurprisingly, the linear expansion captures the correct initial tangency. The arc-length analysis of the quadratic

expansion failed to converge prior to reaching the first limit point.

This shows that once the imperfection height becomes large enough, the quadratic and cubic coefficients attained by centering the Taylor series expansion about the undeformed configuration fail to capture the snap-through behavior. This means that, in order to have a successful NLROM, the lack of the higher-order (4th and higher) terms in the large-deformation regime must be compensated for by the linear, quadratic, and cubic coefficients. Since the cubic information available locally about the undeformed configuration cannot be guaranteed to capture the large-deformation behavior, the identification must consider test cases in displacement configurations deeper into the nonlinear regime.

Note that if the FEM is constructed from elements that follow a perfectly cubic force-displacement behavior, test cases about the undeformed configuration should be sufficient to identify the large-deformation behavior of the FEM. This is because the cubic Taylor series expansion of a truly cubic restoring force with respect to the nodal displacements does not depend on the configuration about which the Taylor series expansion is centered. This would be the case if the elements followed von Kármán beam theory. However, if the force-displacement behavior of the elements is not exactly cubic, such as is the case with co-rotational beam elements, there will necessarily be some error in the ROM approximation of the FEM restoring force, since the higher-order terms are not included. The beam model with an L/36 arch can be adequately captured using the shallow von Kármán beam theory, demonstrating that, even though the NLROMs in Fig. 4.3a were not able to capture the snap-through behavior, a cubic restoring force is a reasonable choice to represent such a model. Thus while a cubic restoring force function can adequately "fit" the snap-through behavior, the cubic Taylor series expansion about the undeformed configuration is likely not the closest fit.

4.4.3 Additional base configurations

Since it has been demonstrated in Subsections 4.4.1 and 4.4.2 that limiting test cases to those in the vicinity of the undeformed configuration does not reliably capture snap-through in

beams with large initial curvatures, a modified approach will be used, where additional test cases are generated about different displacement configurations. These additional configurations, which will be referred to as "base configurations", can be deeper into the nonlinear regime, including mid- and post-snap-through. This idea has been explored in [2], where the STEP was extended to include "baseline" displacement configurations in the snapped and unsnapped states. These configurations were determined by conducting a nonlinear static analysis on the finite element model, wherein a sufficient transverse load was applied to induce snap-through. The resulting full-order displacement configurations were then projected onto the modal basis.

In [2], the same set of test cases applied to the structure about its undeformed configuration was also superimposed onto the snapped configuration. A similar approach is used in this study, differing in that the displacements are only prescribed to the transverse displacment DOFs, while the rotation and axial displacement DOFs are left unrestrained, as described in Subsection 2.1.3. The displacement shapes used in the STEP consisting of combinations of one, two, or three of the mode shapes are used as "superimposed" displacements on top of a combination of base configurations. Recall that to identify an M-mode NLROM, the STEP uses $3M$ single-mode tests, $\frac{3}{2}M(M-1)$ two-mode tests, and $\frac{1}{6}M(M-1)(M-2)$ three-mode tests. For test case p of the training set, the displacement applied to the transverse DOFs of the FEM are computed as

$$\mathbf{w}^{p(i,j)} = \mathbf{\Phi}_b \left(\mathbf{q}_o^i + \mathbf{q}_s^j \right), \qquad i \in \{1, n_o\}, \quad j \in \{1, n_s\}, \tag{4.7}$$

where n_s is the number of superimposed test cases, n_o is the number of base configurations, $\mathbf{q}_o^i$ is the i-th vector of modal displacements in the base configuration set, $\mathbf{q}_s^j$ is the j-th vector of modal displacements in the superimposed configuration set, and $p(i,j) = j + (i-1)n_s$. The concept of superimposing the STEP test cases on additional base configurations is illustrated in Fig. 4.6. Since this modified identification yields training sets that have more data points than the restoring force parameters have unknowns, the parameters are computed using a least-squares approach.

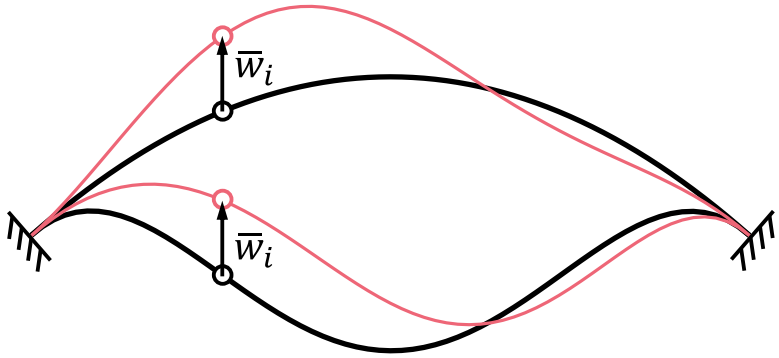

Figure 4.6: Superimposed test case, two base configurations shown

Instead of computing base configurations using a traditional nonlinear static analysis, base configurations are selected as "snapshots" of the SEP determined from arc-length analysis. This allows the study to consider mid-snap-through configurations in addition to pre- and post-snap configurations. Such snapshots could presumably be taken from a brief dynamic analysis of a beam loaded to snap-through, though that method is not explored here. Since ROM identification generates a model that, by some metric, best fits the provided training data, it is hypothesized that centering test cases about additional configurations (besides the undeformed configuration) would improve the model quality in the vicinity of those configurations.

For the purposes of this study, six base configurations (1-6) will be considered in addition to the undeformed configuration (0). These configurations are identified in Fig. 4.7, which shows the deformed shapes of the base configurations of a representative curved beam. This selection includes configurations before, during, and after snap-through. The base configurations are identified as follows. Configuration (1) occurs at the first limit point, where the structure reaches its maximum load prior to snap-through. Configuration (2) occurs after the first limit point, where the load factor decreases by one-third of the difference between the first two limit loads. Configuration (3) occurs after the first limit point, where the load decreases by one-half of the difference between the first two limit loads. Configuration (4)

occurs after the first limit point, where the load factor decreases by two-thirds of the difference between the first two limit loads. Configuration (5) occurs at the second limit point, where the structure reaches its minimum load after snap-through. Configuration (6) is the loaded snap-down configuration, which occurs when the load factor first reaches the value of the first limit load again after snap-through. For scenarios where the beam is expected to see larger loads, additional test cases could be added.

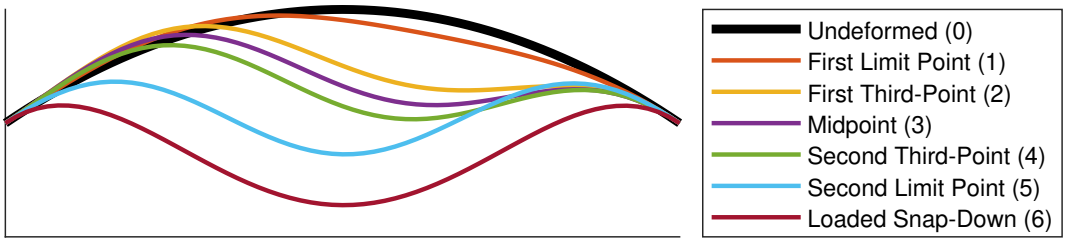

Figure 4.7: Deformed shapes of base configurations (scaled for visibility)

Figure 4.8 identifies these configurations on a plot of load factor versus midpoint deflection of a representative curved beam. The goal of the procedure is to choose the set of base configurations that results in the greatest improvement in the NLROM while adding the fewest additional test cases. The identification procedure employed will generate a ROM that

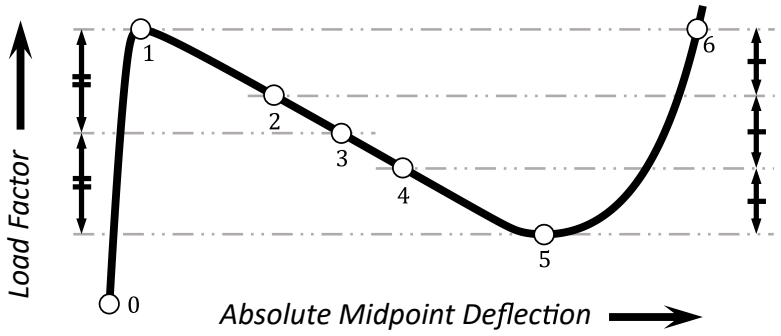

Figure 4.8: Base configurations identified on SEP

in some way satisfies the provided training data, either exactly or in a least-squares sense. Thus, enriching the training data with test cases centered about an additional configuration should improve the quality of the fit near that configuration, while potentially de-prioritizing the other configurations. A set of base configurations then should be selected to yield the greatest improvement in the ROM fit over the expected response domain of the structure.

4.4.4 Numerical study on base configurations

The base configurations defined in Subsection 4.4.3 were used in various combinations to compile a series of training data sets. For each training data set, both an NLROM and a GROM were generated. Each ROM was named according to its base configurations, with the numbers corresponding to the configurations appearing in the subscript. For example, NLROM_{135} and GROM_{135} were identified using base configurations 1, 3, and 5, corresponding to the first limit point, the snap-through midpoint, and the second limit point, respectively. The same set of superimposed test cases was used for each base configuration, with the maximum transverse displacement relative to the base configuration equaling one-half a beam thickness (1.143 mm).

An error metric was needed to characterize the goodness of fit of the restoring force of each ROM generated, and it was desired that the error be characterized for every step along the SEP. A proper error metric should yield a high value in displacement configurations where the ROM fit is poor and a low value in configurations where the fit is good. Since the ROM identification procedure minimizes the difference between the ROM restoring force and the projected FEM restoring force over the training data set, it seemed suitable to use this difference as an error metric. Let $\mathbf{q}_i$ be the modal displacement vector of the equilibrium solution at arc-length step i, let $\mathbf{f}_{FEM}$ be the transverse component of the FEM restoring force when subjected to an applied transverse displacement $\mathbf{\Phi}_b\mathbf{q}_i$, and let $\mathbf{f}_{ROM}$ be the ROM restoring force when subjected to a modal displacement of $\mathbf{q}_i$. The error ε_{ROM} in the ROM

restoring force at step i can then be expressed as

$$\varepsilon_{ROM} = \left\| \mathbf{\Phi}_b^T \, \mathbf{f}_{FEM} - \tilde{\mathbf{f}}_{ROM} \right\| , \tag{4.8}$$

which is the norm of the difference between the projected FEM restoring force and the ROM restoring force. Note that this error metric can be applied to either an NLROM or a GROM.

This error value was computed for each configuration along the SEP of the truth model, though since the displacements of the truth model's SEP are full-order, they needed to be projected onto the modal basis before a direct comparison of the restoring force could be made. The modal displacement vector $\mathbf{q}_i$ for step i in the SEP of the truth model was computed using the pseudoinverse as

$$\mathbf{q}_i = (\mathbf{\Phi}^T \mathbf{\Phi})^{-1} \mathbf{\Phi}^T \mathbf{w}_i \tag{4.9}$$

where $\mathbf{w}_i$ is the vector of transverse displacements of the truth model at step i of the SEP. Thus, both the FEM and the ROM are subjected to the projection of the truth model's SEP onto the modal basis. The evaluation procedure can be summarized as follows.

1. Compute the SEP of the FEM using the arc-length method (configurations are full-order).

2. Project the full-order SEP transverse displacements onto the modal basis using Eq. (4.9).

3. Apply the projected displacements $\mathbf{\Phi}_b \mathbf{q}_i$ to the transverse DOFs of the FEM while the rotation and axial displacement DOFs are unrestrained, and attain the transverse reaction forces $\mathbf{f}_{FEM}$.

4. Apply the modal displacements $\mathbf{q}_i$ to the ROM and attain the reaction forces $\mathbf{f}_{ROM}$.

5. Compute the error using Eq. (4.8) for all arc-length steps.

This procedure yields the error in the ROM restoring force fit for every configuration along the SEP.

Figure 4.9 shows the error curves for a subset of the ROMs generated for Model A (the L/36 curve). Figure 4.10 shows the same for Model B (the L/20 curve). Both the NLROM

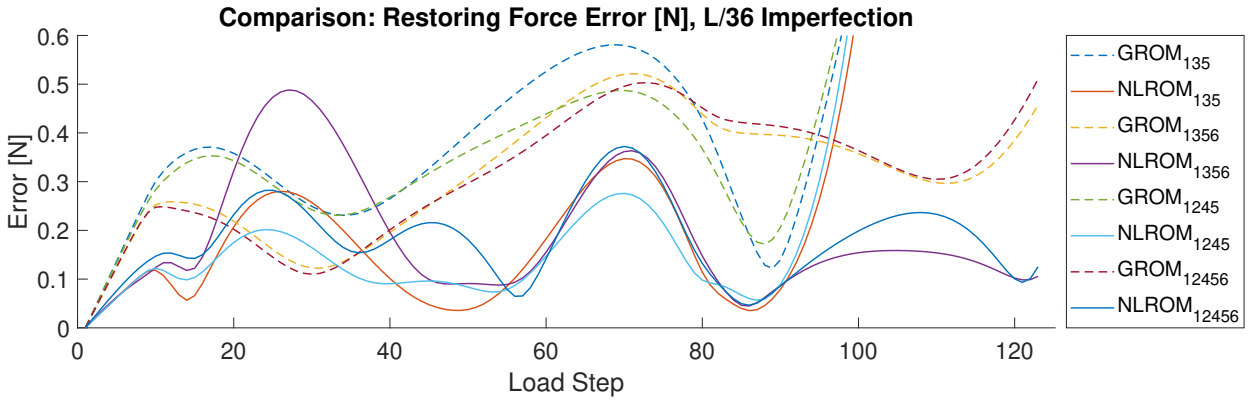

Figure 4.9: Restoring force error [N] of ROMs for Model A

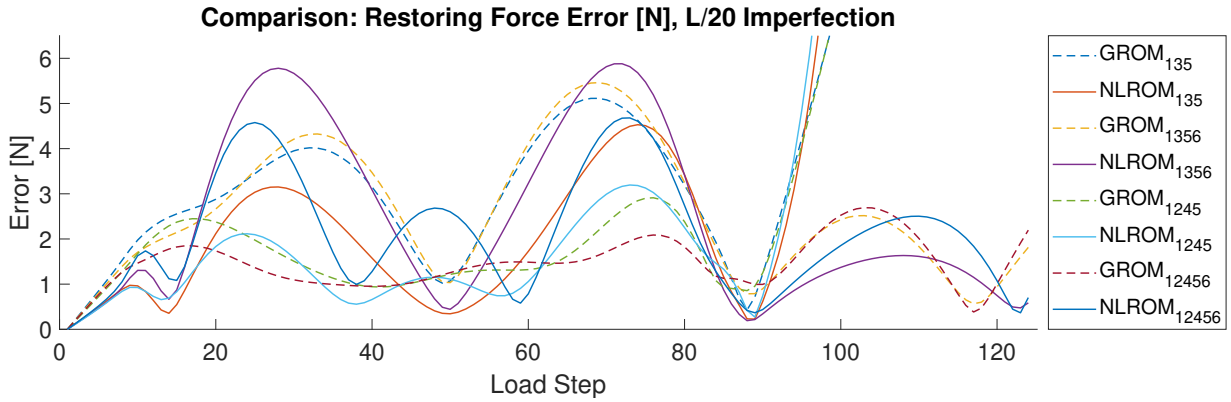

Figure 4.10: Restoring force error [N] of ROMs for Model B

and the GROM error curves responded, albeit differently, to the addition of base configurations. Additionally, both Model A and Model B experienced similar trends, so observations noted here can be assumed to apply to both models unless otherwise stated. The NLROMs exhibited strong local reductions in the error in the vicinity of the base configurations included in the training data set. NLROM_0 (not plotted), which was generated using test cases

centered about the undeformed configuration only, had the smallest error of all the ROMs near the undeformed configuration, but the error increased rapidly beyond the linear regime, reflecting the issues encountered in Section 4.4. NLROM_0 failed to capture snap-through. The addition of the second limit point (5) in the creation of NLROM_{05} and NLROM_{15} (neither plotted) allowed both models to successfully capture snap-through, providing a significant improvement over NLROM_0. The error curve for NLROM_{15} showed clear minima local near the limit points (1 and 5), with the error increasing between the limit points in the middle of the snap-through region. The addition of configuration (3), creating NLROM_{135}, resulted in the appearance of a new local error minimum near configuration (3), approximately halfway between the limit points. Replacing configuration (3) with configurations (2) and (4) had a similar effect of decreasing the error peaks in the snap-through region, though NLROM_{1245} had a slightly larger mean error than NLROM_{135}. The mean values of the error curves in Figs. 4.9 and 4.10 are reported in Table 4.2. It appears that increasing the number of base configurations distributed throughout the snap-through region "flattens" the error curve so that the disparity between maxima and minima decreases.

Table 4.2: Mean error values [N] for ROMs of Model A and Model B

	Model A L/36 Rise		Model B L/20 Rise	
Base Configurations	NLROM	GROM	NLROM	GROM
0, 5	0.2161	0.1775	4.5169	1.6616
1, 5	0.1974	0.1789	4.1805	1.7078
1, 3, 5	0.1823	0.1467	3.6383	1.2493
1, 3, 5, 6	0.0427	0.0708	0.5516	0.5857
1, 2, 4, 5	0.1983	0.1428	3.9638	1.0780
1, 2, 4, 5, 6	0.0407	0.0704	0.4779	0.3297
1, 5, 6	0.2063	0.1414	3.9701	1.5829

The GROMs also responded to the addition of base configurations, but the error curve appeared to be less sensitive to modifications in the base configuration set. For instance, in the case of Model A, the mid-snap-through region lacked strong local error minima where configurations (2)-(4) were added, but the GROMs generated with configuration (6), GROM_{1356} and GROM_{12456}, had a generally lower error in the early- to mid-snap-through region and a higher error in the vicinity of configuration (5). In the case of Model B, which had the larger L/20 curve, GROM_{135} and GROM_{1356} each showed a strong local error minimum near configuration (3). Replacing configuration (3) with (2) and (4), resulting in GROM_{1245} and GROM_{12456}, had the effect of "flattening" the error curves between the limit points without increasing the error significantly near configuration (3).

The addition of configuration (6), corresponding to the loaded snap-down position, appears to have the greatest impact on the mean error of all ROMs. The inclusion of configuration (5) results in an error minimum immediately following snap-through, but there is a sharp increase in the error beyond that point, as the snapped-down model continues to be loaded. Adding configuration (6) flattens the error between (5) and (6), significantly decreasing the mean error over the full load-displacement path. The significant stiffening beyond configuration (5) likely contributes to this sensitivity.

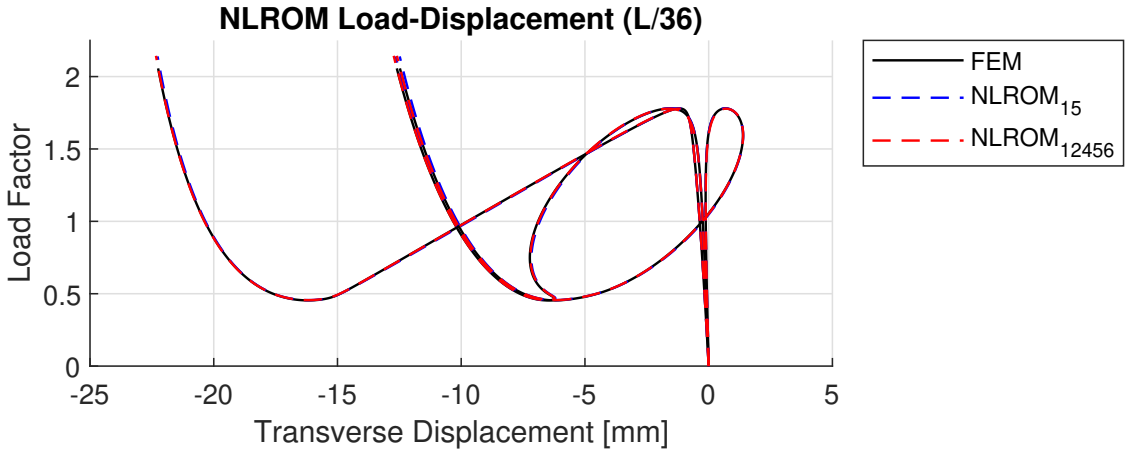

Figure 4.11: SEPs of FEM and representative NLROMs

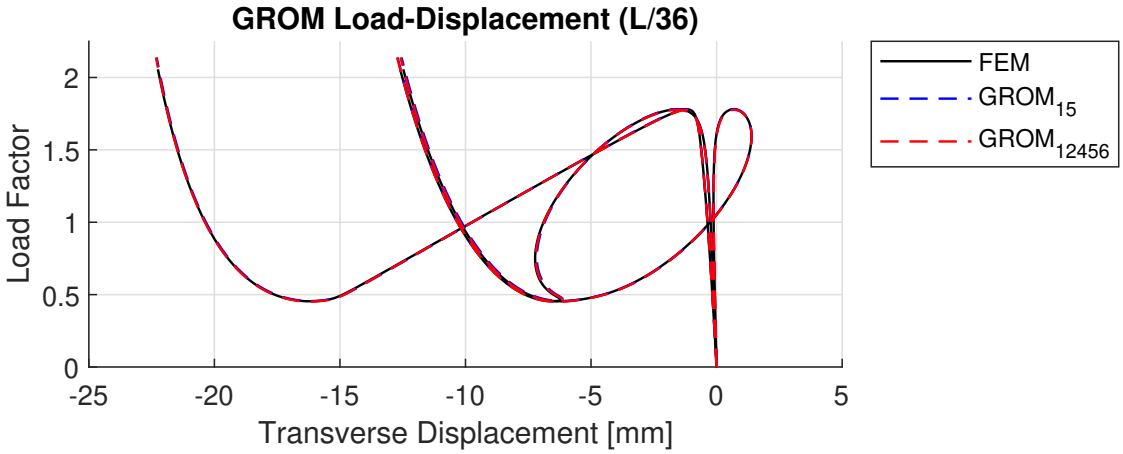

Figure 4.12: SEPs of FEM and representative GROMs

The SEP of the Model A FEM is plotted with the SEPs of two representative NLROMs, NLROM_{15} and NLROM_{12456}, in Fig. 4.11, and again with the SEPs of GROM_{15} and GROM_{12456} in Fig. 4.12. These ROMs were chosen for the comparison because they represented approximately the upper and lower bounds on the mean error of the models studied. Qualitatively, all of the models had a high-quality fit to the FEM. While the differences are small, the ROMs generated with configurations (1,2,4,5,6) had a closer fit throughout the SEP than the corresponding ROMs generated with configurations (1,5), with the most noticeable difference occuring near the end of the path in the post-snap-through stiffening phase. Due to the high-quality fit of all the ROMs studied, it appears that utilizing at least one base configuration before and after snap-through should generate a suitable ROM. Figure 4.11 reveals that NLROM_{12456} had a closer fit than NLROM_{15} in the post-snap-through stiffening region, though NLROM_{15} had a slightly closer fit in the region prior to snap-through. Likewise in Fig. 4.12, GROM_{12456} had a closer fit than GROM_{15} in the post-snap-through stiffening region, but by a smaller margin than observed with the NLROMs.

4.5 Conclusions

In this work it was demonstrated that, in beams with moderate initial curvature, a cubic Taylor series expansion centered about the undeformed configuration is insufficient to capture the snap-through behavior, and minimally a 5th-order term is required before the fit becomes acceptable. This observation provides the insight that, for beams with moderate initial curvature, training data clustered solely around the undeformed configuration is likely insufficient to identify a model that accurately captures snap-through behavior. Consequently, if a ROM with a cubic force-displacement relationship is desired, the parameters of the cubic restoring force need to be identified such that the higher-order behavior is best captured throughout the anticipated response domain.

A novel approach was proposed for the non-intrusive identification of beams with shallow curvature in the form of a GROM. The GROM was capable of accurately capturing the static force-displacement response of the beams studied, and the GROM fit was significantly more consistent than the NLROM fit when both models were identified with test cases centered around the undeformed configuration. The post-snap-through behavior of the NLROMs identified in this way was highly irregular and sensitive to the relative scaling of the modes in the test cases. The post-snap-through behavior of the GROMs, while not a perfect fit, adhered much more closely to the FEM. The fit quality of the GROM was able to be significantly improved through the addition of base configurations. In the case of Model B, which had the larger $L/20$ curve, GROM_{12456} had the smallest mean error of all the ROMs generated for that model. The number of unique parameters in a GROM is $O(M^2)$, which is significantly less than the $O(M^4)$ required for an NLROM. Despite this disparity, the GROMs were comparable to the NLROMs in fit quality.

It was determined that the targeting of specific displacement configurations in training data generation resulted in local improvements in the approximation error in the vicinity of the targeted configurations. The local minima in the error were more clearly discernible for the NLROMs, but both the NLROMs and GROMs responded to the additional configu-

rations. Adding configuration (6), corresponding to the loaded snap-down position, greatly improved the fit of the ROMs in the post-snap-through stiffening phase. The addition of the mid-snap through configurations (2-4) resulted in a notable improvement in the mid-snap-through region over ROMs where those configurations were omitted. Based on observations from the numerical studies, it appears that training sets for curved beams where snap-through is expected should include at least one configuration before snap-through and one configuration after snap-through.

Chapter 5

NONLINEAR REDUCED-ORDER MODELS WITH THICKNESS-VARYING MODES FOR SUBSTRUCTURING OF PLANE ELASTICITY FINITE ELEMENT MODELS

5.1 Introduction

Local defects and crack propagation in structures undergoing a large number of cycles is a subject of interest. Nonlinear Reduced-Order Models (NLROMs) can significantly reduce the computational burden of dynamic analyses, but they require modification to account for damage. Several prominent works have looked at using NLROMs to simulate structures with local defects [13, 30–32, 35, 51].

Modal substructuring of linear Finite Element Models (FEMs) has been accomplished using the Craig-Bampton approach [4]. The Craig-Bampton approach has more recently been extended to model geometrically nonlinear structures [17, 19], and for continuous interfaces with many DOFs using Characteristic Constraint Modes (CCMs) [16, 18, 20].

This chapter presents a substructuring technique whereby an NLROM is coupled to a plane stress FEM. The primary application that is explored is deep beams modeled with 2D plane stress elements. In such an approach, any local features or defects can be modeled with the FEM substructure, while the part of the structure that is expected to remain elastic can be modeled with the NLROM substructure. Such an approach requires that the NLROM and the FEM be constrained along the interface nodes. This task is accomplished by including certain Interface Modes (IMs) in the NLROM modal basis that describe the characteristic behavior of the FEM at the location of the interface, similar to the aforementioned CCMs. The modeling approach is developed and validated using static load cases, and the displacements and stresses of the reduced-order method are compared to those of

the full-order FEM. The approach is first demonstrated on homogeneous planar beams, and then is later applied to the simulation of a multi-layer beam with thickness-varying material properties. The multi-layer beam case study is motivated by the desire to use NLROMs to model laminated composite structures.

5.2 Reduced-order model development

5.2.1 Projection of part of the domain

Consider an N-DOF discrete finite element model with linear damping and a geometrically-nonlinear restoring force. The equation of motion for the model can be expressed as

$$\mathbf{M}\ddot{\mathbf{u}}(t) + \mathbf{C}\dot{\mathbf{u}}(t) + \mathbf{R}(\mathbf{u}(t)) = \mathbf{F}(t)\,, \tag{5.1}$$

where $\mathbf{u} \in \mathbb{R}^N$ is the vector of nodal displacements, $\mathbf{M} \in \mathbb{R}^{N\times N}$ is the mass matrix, $\mathbf{C} \in \mathbb{R}^{N\times N}$ is the damping matrix, $\mathbf{R}(\mathbf{u}) : \mathbb{R}^N \mapsto \mathbb{R}^N$ is the nonlinear internal force vector, $\mathbf{F}(t) \in \mathbb{R}^N$ is the time-varying external force vector, and $t \in \mathbb{R}$ is time. Let the vector of

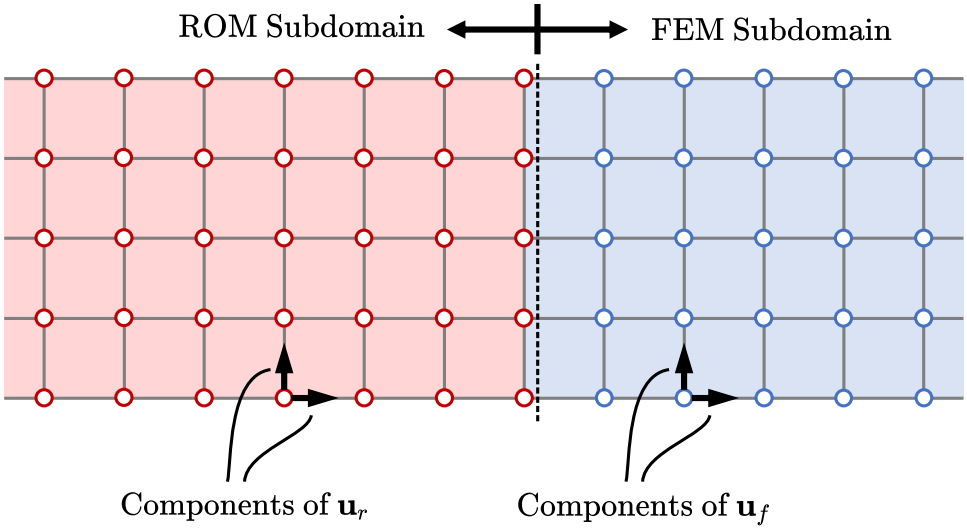

Figure 5.1: Subdomains of the substructuring problem

displacements be partitioned into two components as

$$\mathbf{u} = \begin{Bmatrix} \mathbf{u}_f \\ \mathbf{u}_r \end{Bmatrix}, \tag{5.2}$$

where $\mathbf{u}_f \in \mathbb{R}^{N_f}$ contains the displacements that remain full-order, and $\mathbf{u}_r \in \mathbb{R}^{N_r}$ contains the displacements which will be represented as a function of a smaller vector of M modal coordinates $\mathbf{q} \in \mathbb{R}^M$. This partitioning is illustrated in Fig. 5.1. Time dependency is omitted for brevity. The partitioned system of equations takes the form

$$\begin{bmatrix} \mathbf{M}_{ff} & \mathbf{M}_{fr} \\ \mathbf{M}_{rf} & \mathbf{M}_{rr} \end{bmatrix} \begin{Bmatrix} \ddot{\mathbf{u}}_f \\ \ddot{\mathbf{u}}_r \end{Bmatrix} + \begin{bmatrix} \mathbf{C}_{ff} & \mathbf{C}_{fr} \\ \mathbf{C}_{rf} & \mathbf{C}_{rr} \end{bmatrix} \begin{Bmatrix} \dot{\mathbf{u}}_f \\ \dot{\mathbf{u}}_r \end{Bmatrix} + \begin{Bmatrix} \mathbf{R}_f(\mathbf{u}_f, \mathbf{u}_r) \\ \mathbf{R}_r(\mathbf{u}_f, \mathbf{u}_r) \end{Bmatrix} = \begin{Bmatrix} \mathbf{F}_f \\ \mathbf{F}_r \end{Bmatrix}. \tag{5.3}$$

Let $\mathbf{\Gamma}(\mathbf{u}_f, \mathbf{q}) : \mathbb{R}^{N_f+M} \mapsto \mathbb{R}^N$ be a nonlinear map from the reduced-order DOFs to the full-order DOFs. Considering that the displacements in $\mathbf{u}_f$ remain full-order, the map can be partitioned as

$$\mathbf{\Gamma}(\mathbf{u}_f, \mathbf{q}) = \begin{Bmatrix} \mathbf{u}_f \\ \mathbf{\Gamma}_r(\mathbf{q}) \end{Bmatrix}, \tag{5.4}$$

where $\mathbf{\Gamma}_r(\mathbf{q}) : \mathbb{R}^M \mapsto \mathbb{R}^{N_r}$ is a function that maps the modal coordinates $\mathbf{q}$ to the full-order displacements $\mathbf{u}_r$, and $\mathbf{u}_f$ simply maps to itself. It is demonstrated in [14,40] using a Galerkin projection that the reduced-order equation of motion, given a nonlinear mapping between reduced-order and full-order displacements, can be expressed as

$$\mathbf{P}_\Gamma^T \left[\mathbf{M}\, \ddot{\mathbf{\Gamma}}(\mathbf{u}_f, \mathbf{q}) + \mathbf{C}\, \dot{\mathbf{\Gamma}}(\mathbf{u}_f, \mathbf{q}) + \mathbf{R}(\mathbf{\Gamma}(\mathbf{u}_f, \mathbf{q})) \right] = \mathbf{P}_\Gamma^T\, \mathbf{F}\,, \tag{5.5}$$

where $\mathbf{P}_\Gamma$ is defined in terms of the differential of $\mathbf{\Gamma}$ as

$$\mathbf{P}_\Gamma \cdot \begin{Bmatrix} d\mathbf{u}_f \\ d\mathbf{q} \end{Bmatrix} = d\,\mathbf{\Gamma}\,. \tag{5.6}$$

Computing the differential of $\mathbf{\Gamma}(\mathbf{u}_f, \mathbf{q})$ and using the definition in Eq. (5.6) yields

$$\mathbf{P}_\Gamma = \begin{bmatrix} \mathbf{I}_{N_f} & \mathbf{0} \\ \mathbf{0} & \mathbf{P}_r \end{bmatrix}. \tag{5.7}$$

where $\mathbf{P}_r \cdot d\mathbf{q} = d\,\mathbf{\Gamma}_r$. The equation of motion of the projected system can then be written as

$$\begin{bmatrix} \mathbf{M}_{ff} & \mathbf{M}_{fr}\mathbf{P}_r \\ \mathbf{P}_r^T\mathbf{M}_{rf} & \mathbf{P}_r^T\mathbf{M}_{rr}\mathbf{P}_r \end{bmatrix} \begin{Bmatrix} \ddot{\mathbf{u}}_f \\ \ddot{\mathbf{q}} \end{Bmatrix} + \begin{bmatrix} \mathbf{C}_{ff} & \mathbf{C}_{fr}\mathbf{P}_r \\ \mathbf{P}_r^T\mathbf{C}_{rf} & \mathbf{P}_r^T\mathbf{C}_{rr}\mathbf{P}_r \end{bmatrix} \begin{Bmatrix} \dot{\mathbf{u}}_f \\ \dot{\mathbf{q}} \end{Bmatrix} + \begin{Bmatrix} \mathbf{M}_{fr}\dot{\mathbf{P}}_r\dot{\mathbf{q}} \\ \mathbf{P}_r^T\mathbf{M}_{fr}\dot{\mathbf{P}}_r\dot{\mathbf{q}} \end{Bmatrix} + \begin{Bmatrix} \mathbf{R}_f(\mathbf{u}_f, \mathbf{u}_r) \\ \mathbf{P}_r^T\mathbf{R}_r(\mathbf{u}_f, \mathbf{\Gamma}_r(\mathbf{q})) \end{Bmatrix} = \begin{Bmatrix} \mathbf{F}_f \\ \mathbf{P}_r^T\mathbf{F}_r \end{Bmatrix}. \tag{5.8}$$

The function $\mathbf{\Gamma}_r(\mathbf{q})$ employed in this study will be taken to be a cubic function of $\mathbf{q}$

$$\mathbf{\Gamma}_r(\mathbf{q}) = \mathbf{\Phi}^{(1)}\mathbf{q} + \mathbf{\Phi}^{(2)}\mathbf{q}^{(2)} + \mathbf{\Phi}^{(3)}\mathbf{q}^{(3)} \tag{5.9}$$

where $\mathbf{q}^{(2)} \in \mathbb{R}^{M^{(2)}}$ is every unique product of two components of $\mathbf{q}$, summarized as

$$\begin{aligned} \mathbf{q}^{(2)} = [\, q_1^2 \quad q_1\,q_2 \quad q_1\,q_3 \quad \ldots \quad q_1\,q_M \quad q_2^2 \quad q_2\,q_3 \quad \ldots \quad q_2\,q_M \\ \ldots \quad q_{M-1}^2 \quad q_{M-1}\,q_M \quad q_M^2\,]^T, \end{aligned} \tag{5.10}$$

and $\mathbf{q}^{(3)} \in \mathbb{R}^{M^{(3)}}$ is every unique product of three components of $\mathbf{q}$, summarized as

$$\begin{aligned} \mathbf{q}^{(3)} = [\, q_1^3 \quad q_1^2\,q_2 \quad q_1^2\,q_3 \quad \ldots \quad q_1^2\,q_M \quad q_1\,q_2^2 \quad q_1\,q_2\,q_3 \quad \ldots \quad q_1\,q_M^2 \quad q_2^3 \quad q_2^2\,q_3 \\ \ldots \quad q_{M-1}^3 \quad q_{M-1}^2\,q_M \quad q_{M-1}\,q_M^2 \quad q_M^3\,]^T. \end{aligned} \tag{5.11}$$

The lengths of $\mathbf{q}^{(2)}$ and $\mathbf{q}^{(3)}$ are $M^{(2)} = \frac{1}{2}M(M+1)$ and $M^{(3)} = \frac{1}{6}M(M+1)(M+2)$, respectively. Matrices $\mathbf{\Phi}^{(1)} \in \mathbb{R}^{N_r \times M}$, $\mathbf{\Phi}^{(2)} \in \mathbb{R}^{N_r \times M^{(2)}}$, $\mathbf{\Phi}^{(3)} \in \mathbb{R}^{N_r \times M^{(3)}}$ are coefficients of the linear, quadratic, and cubic terms of $\mathbf{\Gamma}_r(\mathbf{q})$. This is a similar form to that used in [11] to expand the membrane displacements in the Implicit Condensation and Expansion (ICE) procedure. Now, $\mathbf{P}_r(\mathbf{q})$ can be expressed as

$$\mathbf{P}_r(\mathbf{q}) = \mathbf{\Phi}^{(1)} + \mathbf{\Phi}^{(2)}\mathbf{q}^{(2)}_{,\mathbf{q}} + \mathbf{\Phi}^{(3)}\mathbf{q}^{(3)}_{,\mathbf{q}}, \tag{5.12}$$

where

$$(\mathbf{q}^{(2)}_{,\mathbf{q}})_{ij} = \frac{\partial q_i^{(2)}}{\partial q_j}, \tag{5.13}$$

and

$$(\mathbf{q}^{(3)}_{,\mathbf{q}})_{ij} = \frac{\partial q_i^{(3)}}{\partial q_j}. \tag{5.14}$$

5.2.2 Non-intrusive identification

Consider the static case of Eq. (5.8), where $\ddot{\mathbf{u}}_f = \mathbf{0}$, $\dot{\mathbf{u}}_f = \mathbf{0}$, $\ddot{\mathbf{q}} = \mathbf{0}$, and $\dot{\mathbf{q}} = \mathbf{0}$. Static equilibrium is satisfied when

$$\begin{Bmatrix} \mathbf{R}_f(\mathbf{u}_f, \mathbf{u}_r) \\ \mathbf{P}_r^T \mathbf{R}_r(\mathbf{u}_f, \mathbf{\Gamma}_r(\mathbf{q})) \end{Bmatrix} = \begin{Bmatrix} \mathbf{F}_f \\ \mathbf{P}_r^T \mathbf{F}_r \end{Bmatrix}. \tag{5.15}$$

In the construction of an NLROM, all or part of the "projected internal force", which in this case is the term $\mathbf{P}_r^T \mathbf{R}_r(\mathbf{u}_f, \mathbf{\Gamma}_r(\mathbf{q}))$, is replaced by an identified function $\tilde{\mathbf{R}}(\mathbf{q}) : \mathbb{R}^M \mapsto \mathbb{R}^M$ with an assumed form. Because there are elements that connect DOFs in $\mathbf{u}_f$ to DOFs in $\mathbf{u}_r$, the projected internal force is not purely a function of $\mathbf{q}$. Thus, only the part of $\mathbf{P}_r^T \mathbf{R}_r(\mathbf{u}_f, \mathbf{\Gamma}_r(\mathbf{q}))$ that is purely a function of $\mathbf{q}$ can be approximated by $\tilde{\mathbf{R}}(\mathbf{q})$. In order to accomplish this, the restoring force $\mathbf{R}_r(\mathbf{u}_f, \mathbf{\Gamma}_r(\mathbf{q}))$ is expressed as the sum of $\mathbf{R}_r^{FEM}(\mathbf{u}_f, \mathbf{\Gamma}_r(\mathbf{q}))$, which is the contribution from the elements in the FEM subdomain, and $\mathbf{R}_r^{ROM}(\mathbf{\Gamma}_r(\mathbf{q}))$, which is the contribution from the elements in the ROM subdomain. The elements contributing to $\mathbf{R}_r^{FEM}(\mathbf{u}_f, \mathbf{\Gamma}_r(\mathbf{q}))$ and $\mathbf{R}_r^{ROM}(\mathbf{\Gamma}_r(\mathbf{q}))$ are shown in Fig. 5.2.

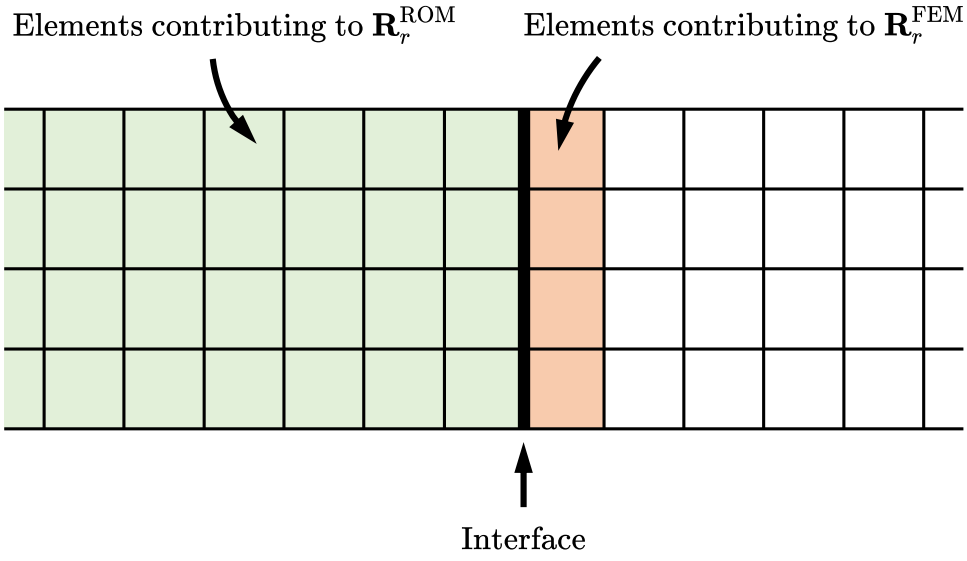

Figure 5.2: Division of elements contributing to $\mathbf{R}_r^{FEM}$ and $\mathbf{R}_r^{ROM}$

Now, because $\mathbf{R}_r^{ROM}$ is purely a function of $\mathbf{q}$ and not of $\mathbf{u}_f$, a non-intrusive technique can be employed which approximates $\mathbf{P}_r^T\mathbf{R}_r^{ROM} \approx \tilde{\mathbf{R}}(\mathbf{q})$, with

$$\tilde{R}_i = \sum_{j=1}^{M} \tilde{K}_{ij}^{(1)} q_j + \sum_{j=1}^{M}\sum_{k=1}^{M} \tilde{K}_{ijk}^{(2)} q_k q_j + \sum_{j=1}^{M}\sum_{k=1}^{M}\sum_{l=1}^{M} \tilde{K}_{ijkl}^{(3)} q_l q_k q_j \,, \tag{5.16}$$

and the parameters $\tilde{K}_{ij}^{(1)}$, $\tilde{K}_{ijk}^{(2)}$, and $\tilde{K}_{ijkl}^{(3)}$ are identified from the ROM subdomain of the full FEM. Thus, the element assembly procedure to generate $\mathbf{R}_r^{ROM}(\mathbf{\Gamma}_r(\mathbf{q}))$ is replaced by a single evaluation of Eq. (5.16). The STiffness Evaluation Procedure (STEP), introduced in [28] and elaborated on in [26], involves applying displacements to the FEM in the shape of modal combinations of one, two, and three modes at a time. The resulting external forces required to maintain those configurations are then queried from the model, and the parameters of Eq. (5.16) are identified from the force-displacement data. A modification of the STEP has been used in [48, 49, 51], with [48] referring to the method as M-STEP, where displacements are applied to a subset of the FEM DOFs ("lead" DOFs) while the remaining DOFs ("follower" DOFs) are left unrestrained. Thus, the behavior of the follower DOFs is implicitly condensed into the lead DOFs. A similar approach is used in this study, with some modifications. For the specific beam problem considered in this study, the lead and follower DOFs are classified as shown in Fig. 5.3.

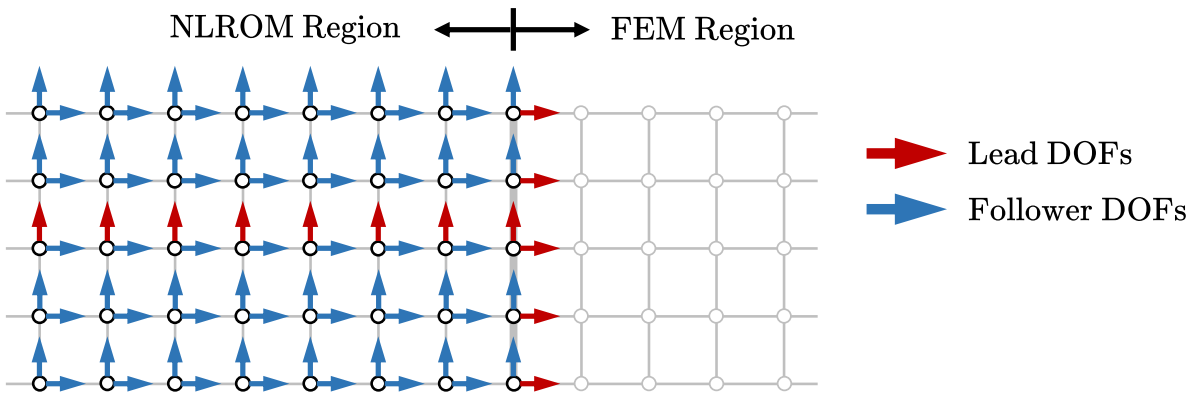

Figure 5.3: DOF classification for substructured model with no transition zone

Within the ROM subdomain, the global-Y (vertical) displacements on the beam midline and the global-X (horizontal) displacements on the interface are chosen to be the lead DOFs. All remaining DOFs in the ROM subdomain, including those on the interface, are chosen to be the follower displacements. The vertical midline displacements are expressed as a linear combination of "transverse modes", and the horizontal interface displacements are expressed as a linear combination of Interface Modes (IMs). Let the number of vertical DOFs on the midline be N_{mid}, and let the number of horizontal DOFs on the interface be N_{int}. Recall that all of the projected DOFs are expanded as $\mathbf{\Gamma}_r(\mathbf{q})$, defined in Eq. (5.9), including those classified as lead DOFs here. Let the matrices $\mathbf{\Phi}^{(1)}$, $\mathbf{\Phi}^{(3)}$, and $\mathbf{\Phi}^{(3)}$ in Eq. (5.9), be partitioned into N_m lead DOFs (subscript m) and N_s follower DOFs (subscript s) as

$$\mathbf{\Phi}^{(1)} = \begin{bmatrix} \mathbf{\Phi}_m^{(1)} \\ \mathbf{\Phi}_s^{(1)} \end{bmatrix}, \qquad \mathbf{\Phi}^{(2)} = \begin{bmatrix} \mathbf{\Phi}_m^{(2)} \\ \mathbf{\Phi}_s^{(2)} \end{bmatrix}, \qquad \mathbf{\Phi}^{(3)} = \begin{bmatrix} \mathbf{\Phi}_m^{(3)} \\ \mathbf{\Phi}_s^{(3)} \end{bmatrix} \tag{5.17}$$

Because the lead DOFs are expressed as a linear function of $\mathbf{q}$, $\mathbf{\Phi}_m^{(2)}$ and $\mathbf{\Phi}_m^{(3)}$ are zero. The transverse modes are chosen to be a combination of Fixed-Interface Modes (FIMs) and Transverse-Constraint Modes (TCMs), which will be subsequently characterized in this subsection. Let the modal basis for the lead DOFs be defined as

$$\mathbf{\Phi}_m^{(1)} = \begin{bmatrix} \mathbf{\Phi}_{FI} & \mathbf{\Phi}_{TC} & \mathbf{0} \\ \mathbf{0} & \mathbf{0} & \mathbf{\Phi}_{IM} \end{bmatrix}, \tag{5.18}$$

where $\mathbf{\Phi}_{FI}$ contains the FIMs, $\mathbf{\Phi}_{TC}$ contains the TCMs, and $\mathbf{\Phi}_{IM}$ contains the IMs. Thus, the transverse modes are nonzero only for the vertical DOFs on the midline, and the interface modes are nonzero only for the horizontal DOFs on the interface. The modal amplitudes $\mathbf{q}$ can be partitioned in a similar way as

$$\mathbf{q} = \begin{Bmatrix} \mathbf{q}_{FI} \\ \mathbf{q}_{TC} \\ \mathbf{q}_{IM} \end{Bmatrix}, \tag{5.19}$$

where $\mathbf{q}_{FI}$, $\mathbf{q}_{TC}$, and $\mathbf{q}_{IM}$ are the modal amplitudes corresponding to $\mathbf{\Phi}_{FI}$, $\mathbf{\Phi}_{TC}$, and $\mathbf{\Phi}_{IM}$, respectively.

Three interface modes, shown in Fig. 5.4, are used in this study for homogeneous beams. A uniform shape $\boldsymbol{\phi}_{\text{const}}$ has a value of one for every element, and it represents a unit horizontal displacement of the interface. A linear shape $\boldsymbol{\phi}_{\text{lin}}$ varies linearly with thickness, and it approximately represents a unit rotation of the cross section. A cubic shape $\boldsymbol{\phi}_{\text{third}}$ approximates the response of the beam to transverse shear force.

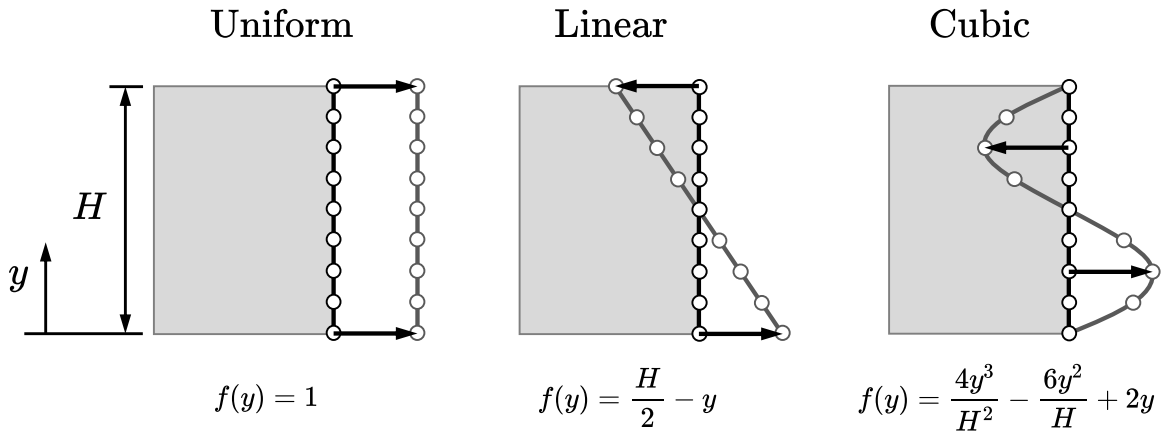

Figure 5.4: Over-thickness interface modes (IMs)

Characterizing the interface in this way does not create a true finite rotation model, due to the interface modes only applying to the horizontal DOFs. Including only the uniform and linear IMs in the basis, such that $\boldsymbol{\Phi}_{\text{lin}} = [\boldsymbol{\phi}_{\text{const}},\ \boldsymbol{\phi}_{\text{lin}}]$, will be referred to as the "Timoshenko" case. Note that this constraint does not identically follow the traditional Timoshenko kinematic assumption because it allows for extension in the through-thickness direction and because the nodes are not required to be co-linear (though they are close to co-linear). Including the uniform, linear, and cubic IMs, such that $\boldsymbol{\Phi}_{\text{third}} = [\boldsymbol{\phi}_{\text{const}},\ \boldsymbol{\phi}_{\text{lin}},\ \boldsymbol{\phi}_{\text{third}}]$, will be referred to as the third-order case. So, the interface modal basis $\boldsymbol{\Phi}_{\text{IM}}$ can be set to either $\boldsymbol{\Phi}_{\text{lin}}$ for the Timoshenko case and $\boldsymbol{\Phi}_{\text{third}}$ for the third-order case. The vector modal amplitudes $\mathbf{q}_{IM}$ for the IMs can take the form $[\,q_{\text{const}}\ \ q_{\text{lin}}]^T$ for the Timoshenko case and $[q_{\text{const}}\ \ q_{\text{lin}}\ \ q_{\text{third}}\,]^T$ for the third-order case.

Fixed-interface modes are modes attained while the displacements of the interface are

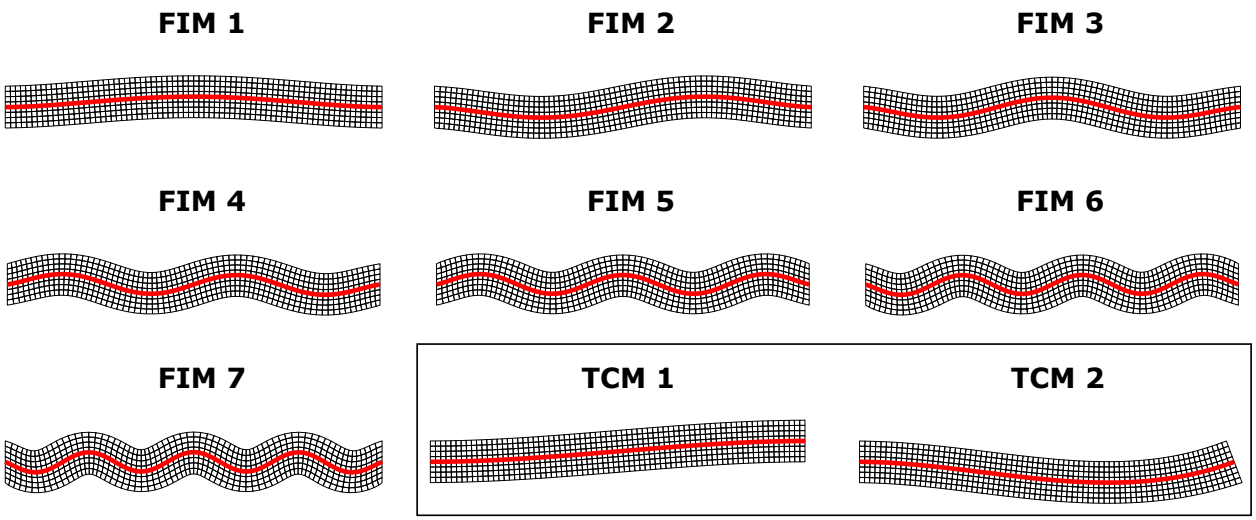

Figure 5.5: First 7 fixed-interface modes, and transverse constraint modes (boxed)

restrained. The linear vibration mode shapes of the FEM of the substructure are computed, and the FIMs are taken to be the vertical displacements of the midline for each of the vibration mode shapes. The transverse constraint modes represent the vertical displacements of the midline when the linear FEM is subjected to (i) unit vertical displacement of all nodes on the interface (TCM 1), and (ii) a unit rotation applied to the nodes on the interface (TCM 2). Because the shapes are computed from a linear FEM, the applied rotation is linearized, equivalent to a unit displacement in the shape of $\boldsymbol{\phi}_{\text{lin}}$. The FIMs and the TCMs are shown for a representative mesh (coarser than is used in the numerical study) in Fig. 5.5, with the midline highlighted in red.

A "test case" will be defined as a single static equilibrium solution of the FEM used for the identification of modal parameters. The modal amplitudes used to generate the test cases are determined using the STEP, which prescribes displacements to the structure in the shape of one, two, and three modes at a time to yield a total of $n_T = \frac{11}{6}M + M^2 + \frac{1}{6}M^3$ test cases. A good overview of this procedure is provided in [26]. Let the modal amplitudes determined using the STEP for test $p \in \{1, n_T\}$ be called $\mathbf{q}_p^{\text{STEP}}$. For the identification of

the beam models in this study, the modal amplitudes $\mathbf{q}_p^{\text{STEP}}$ are superimposed on a "base configuration" $\mathbf{q}_p^o$, so that the displacement field induced by $\mathbf{q}_p^{\text{STEP}}$ is applied relative to the displacement field determined by $\mathbf{q}_p^o$. Thus, the modal displacements $\mathbf{q}_p$ applied to the FEM during test case p is computed as

$$\mathbf{q}_p = \mathbf{q}_p^o + \mathbf{q}_p^{\text{STEP}}\,, \qquad p \in \{1,\, n_T\}\,. \tag{5.20}$$

The base configuration $\mathbf{q}_p^o$ is selected to ensure that the change in angle between the midline and the interface at the cross section is physically reasonable during the test cases. This is accomplished by requiring that the rotation of the cross section, controlled by the scaling of the linear IM $\boldsymbol{\phi}_{\text{lin}}$, is within some specified range of the slope of the midline at the interface, controlled by the scaling of TCM 2. Let the vector of modal amplitudes of the TCMs for test case p be

$$(\mathbf{q}_{TC})_p = \begin{Bmatrix} (v_{TC})_p \\ (\theta_{TC})_p \end{Bmatrix}\,. \tag{5.21}$$

Then, the base modal amplitudes $\mathbf{q}_p^o$ for the test case p are

$$\mathbf{q}_p^o = \begin{Bmatrix} \mathbf{0} \\ \mathbf{0} \\ (\mathbf{q}_{\text{IM}}^o)_p \end{Bmatrix}\,, \tag{5.22}$$

where

$$(\mathbf{q}_{\text{IM}}^o)_p = \begin{Bmatrix} 0 \\ (\theta_{\text{TC}})_p \\ \vdots \end{Bmatrix}\,, \tag{5.23}$$

and the third element of the vector $(\mathbf{q}_{\text{IM}}^o)_p$ is either empty (for the Timoshenko case) or zero (for the third-order case). Thus, when the test cases are generated, the modal amplitudes of the IMs are dependent on the modal amplitudes of the TCMs.

As done in the M-STEP and similar approaches [48, 49, 51], the test case displacements are applied only to the lead DOFs, while the follower DOFs are left unrestrained. The

displacement field $\overline{\mathbf{u}}_m^p$ prescribed to the lead DOFs for test case p is computed as

$$(\overline{\mathbf{u}}_m)_p = \mathbf{\Phi}_m^{(1)} \mathbf{q}_p \,. \tag{5.24}$$

When the displacements $(\overline{\mathbf{u}}_m)_p$ are prescribed to the lead DOFs, the equilibrium follower displacements $(\mathbf{u}_s)_p$ are stored. Because the follower DOFs are unrestrained during the test cases, it should be apparent that the displacements $(\mathbf{u}_s)_p$ were not required to exactly equal $\mathbf{\Gamma}_s(\mathbf{q}_p)$. In fact, the parameters $\mathbf{\Phi}_m^{(1)}$, $\mathbf{\Phi}_m^{(2)}$, and $\mathbf{\Phi}_m^{(3)}$ of $\mathbf{\Gamma}_m(\mathbf{q})$ are unknown when the test cases are generated. These parameters are computed following the generation of the test cases to best approximate the follower displacements $(\mathbf{u}_s)_p$ that were observed during the test cases. Once a complete set of test cases is generated, the parameters $\mathbf{\Phi}^{(1)}$, $\mathbf{\Phi}^{(2)}$, and $\mathbf{\Phi}^{(3)}$ in Eq. (5.9) are computed using a least squares approach as

$$\begin{bmatrix} \mathbf{\Phi}^{(1)} & \mathbf{\Phi}^{(2)} & \mathbf{\Phi}^{(3)} \end{bmatrix} = \mathbf{U}\mathbf{Q}^T \left(\mathbf{Q}\mathbf{Q}^T \right)^{-1} , \tag{5.25}$$

where $\mathbf{q}_p$, $\mathbf{q}_p^{(2)}$, and $\mathbf{q}_p^{(3)}$ for all tests p are stored in the matrix $\mathbf{Q}$ as

$$\mathbf{Q} = \begin{bmatrix} \mathbf{q}_1 & \mathbf{q}_2 & \cdots & \mathbf{q}_{n_T} \\ \mathbf{q}_1^{(2)} & \mathbf{q}_2^{(2)} & \cdots & \mathbf{q}_{n_T}^{(2)} \\ \mathbf{q}_1^{(3)} & \mathbf{q}_2^{(3)} & \cdots & \mathbf{q}_{n_T}^{(3)} \end{bmatrix} , \tag{5.26}$$

and the displacements $(\mathbf{u}_r)_p$ are stored in $\mathbf{U}$ as

$$\mathbf{U} = \begin{bmatrix} (\mathbf{u}_r)_1 & (\mathbf{u}_r)_2 & \cdots & (\mathbf{u}_r)_T \end{bmatrix} . \tag{5.27}$$

Note that, because the test case displacements $(\mathbf{u}_r)_p$ include both lead and follower DOFs, the parameters $\mathbf{\Phi}^{(1)}$, $\mathbf{\Phi}^{(2)}$, and $\mathbf{\Phi}^{(3)}$ computed using Eq. (5.25) include both the lead and follower components. It can be verified that $\mathbf{\Phi}_m^{(2)}$ and $\mathbf{\Phi}_m^{(3)}$ are both zero, and that $\mathbf{\Phi}_m^{(1)}$ is as defined in Eq. (5.18).

Now that a description of $\mathbf{\Gamma}_r(\mathbf{q})$ has been attained, $\mathbf{P}_r(\mathbf{q})$ can be computed using Eq. (5.12), and the external force acting on the ROM substructure, $\mathbf{F}_r^{\mathrm{ROM}}$, can be projected as $\mathbf{P}_r^T(\mathbf{q})\mathbf{F}_r^{\mathrm{ROM}}$. The identification procedure used herein makes the following approximation in the calculation of the projected external force. Because the follower displacements $(\mathbf{u}_s)_p$ attained during

the test cases are not identically $\mathbf{\Gamma}_s(\mathbf{q}_p)$, the external force $(\mathbf{F}_r^{\text{ROM}})_p$ for test p is not identical to the internal force $\mathbf{R}_r^{\text{ROM}}(\mathbf{\Gamma}(\mathbf{q}_p))$. Nevertheless, if $\mathbf{\Gamma}_s(\mathbf{q}_p)$ is assumed to be a satisfactory approximation of $(\mathbf{u}_s)_p$, then $\mathbf{R}_r^{\text{ROM}}(\mathbf{\Gamma}(\mathbf{q}_p)) \approx (\mathbf{F}_r^{\text{ROM}})_p$. The least-squares minimization problem used to non-intrusively identify the parameters from Eq. (5.16) can be expressed as

$$\begin{aligned} \underset{\tilde{\mathbf{K}}^{(1)},\tilde{\mathbf{K}}^{(2)},\tilde{\mathbf{K}}^{(3)}}{\text{minimize}} \quad & \sum_{p=1}^{n_T} \left\| \tilde{\mathbf{R}}(\mathbf{q}_p) - \mathbf{P}_r^T(\mathbf{q}_p)(\mathbf{F}_r^{\text{ROM}})_p \right\|^2 \\ \text{subject to} \quad & \tilde{K}_{ijk}^{(2)} = \tilde{K}_{ikj}^{(2)} \\ & \tilde{K}_{ijkl}^{(3)} = \tilde{K}_{ijlk}^{(3)} = \tilde{K}_{ikjl}^{(3)} = \tilde{K}_{iklj}^{(3)} = \tilde{K}_{iljk}^{(3)} = \tilde{K}_{ilkj}^{(3)} \,. \end{aligned} \tag{5.28}$$

Solving Eq. (5.28) yields the optimal parameters to the NLROM restoring force function $\tilde{\mathbf{R}}(\mathbf{q})$. The equation of motion in Eq. (5.8) can then be modified be replacing the projected internal force term $\mathbf{P}_r^T\mathbf{R}_r(\mathbf{u}_f, \mathbf{\Gamma}_r(\mathbf{q}))$ with the identified version as

$$\mathbf{P}_r^T\mathbf{R}_r(\mathbf{u}_f, \mathbf{\Gamma}_r(\mathbf{q})) \approx \tilde{\mathbf{R}}(\mathbf{q}) + \mathbf{P}_r^T\mathbf{R}_r^{\text{FEM}}(\mathbf{u}_f, \mathbf{\Gamma}_r(\mathbf{q}))\,, \tag{5.29}$$

yielding the equation of motion for the substructured system

$$\begin{aligned} &\begin{bmatrix} \mathbf{M}_{ff} & \mathbf{M}_{fr}\mathbf{P}_r \\ \mathbf{P}_r^T\mathbf{M}_{rf} & \mathbf{P}_r^T\mathbf{M}_{rr}\mathbf{P}_r \end{bmatrix} \begin{Bmatrix} \ddot{\mathbf{u}}_f \\ \ddot{\mathbf{q}}_r \end{Bmatrix} + \begin{bmatrix} \mathbf{C}_{ff} & \mathbf{C}_{fr}\mathbf{P}_r \\ \mathbf{P}_r^T\mathbf{C}_{rf} & \mathbf{P}_r^T\mathbf{C}_{rr}\mathbf{P}_r \end{bmatrix} \begin{Bmatrix} \dot{\mathbf{u}}_f \\ \dot{\mathbf{q}}_r \end{Bmatrix} + \begin{Bmatrix} \mathbf{M}_{fr}\dot{\mathbf{P}}_r\dot{\mathbf{q}} \\ \mathbf{P}_r^T\mathbf{M}_{fr}\dot{\mathbf{P}}_r\dot{\mathbf{q}} \end{Bmatrix} \\ &\qquad + \begin{Bmatrix} \mathbf{R}_f(\mathbf{u}_f, \mathbf{u}_r) \\ \tilde{\mathbf{R}}(\mathbf{q}) + \mathbf{P}_r^T\mathbf{R}_r^{\text{FEM}}(\mathbf{u}_f, \mathbf{\Gamma}_r(\mathbf{q})) \end{Bmatrix} = \begin{Bmatrix} \mathbf{F}_f \\ \mathbf{P}_r^T\mathbf{F}_r \end{Bmatrix} . \end{aligned} \tag{5.30}$$

5.2.3 Adding a transition zone

The assumption that the follower displacements can be expanded purely as a function of $\mathbf{q}$ disregards the coupling that exists between $\mathbf{u}_f$ and $\mathbf{u}_s$ on the interface. This is plainly observable in the case where $\mathbf{q}$ is held constant at zero and a transverse shear force is applied to a cross section in the FEM substructure close to the interface. This scenario is illustrated in Fig. 5.6. If the follower DOFs remained full-order, then they would displace in response to the prescribed displacement on the FEM side of the boundary. However, since the follower displacements are assumed to be a function of only $\mathbf{q}$, the substructured model would exhibit zero displacement of the follower DOFs.

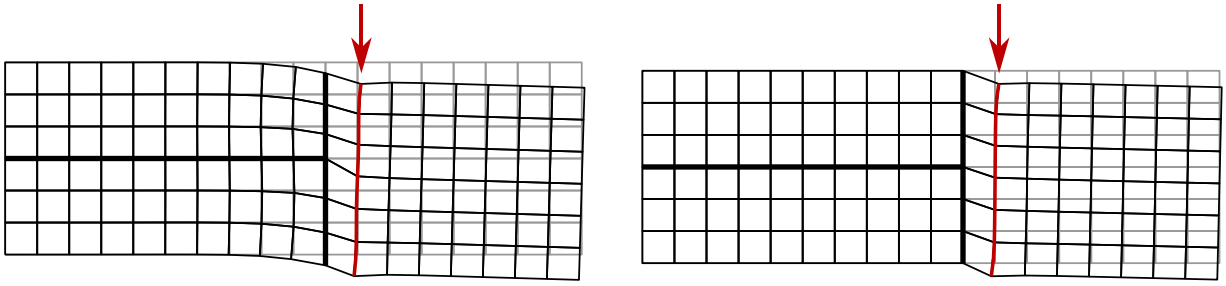

(a) Follower DOFs replaced with full-order DOFs (b) Follower DOFs expanded as $\mathbf{\Gamma}_s(\mathbf{q})$

Figure 5.6: Load case demonstrating the coupling between the follower DOFs and the DOFs in the FEM substructure

To mitigate this issue, a "transition zone" is added between the NLROM and FEM substructures which replaces some of the follower DOFs with full-order DOFs. The transition zone should be long enough that the sensitivity of the follower DOFs in the remaining NLROM substructure is acceptably small. The lead and follower DOFs are reclassified as shown in Fig. 5.7. Note that all of the original lead DOFs are retained, and they are still expanded as $\mathbf{\Phi}_m^{(1)}\mathbf{q}$.

Because the follower DOFs in the transition region are converted to full-order DOFs, the elements contributing to $\mathbf{R}_r^{FEM}(\mathbf{u}_f, \mathbf{\Gamma}_r(\mathbf{q}))$ and $\mathbf{R}_r^{ROM}(\mathbf{\Gamma}_r(\mathbf{q}))$ are different than what

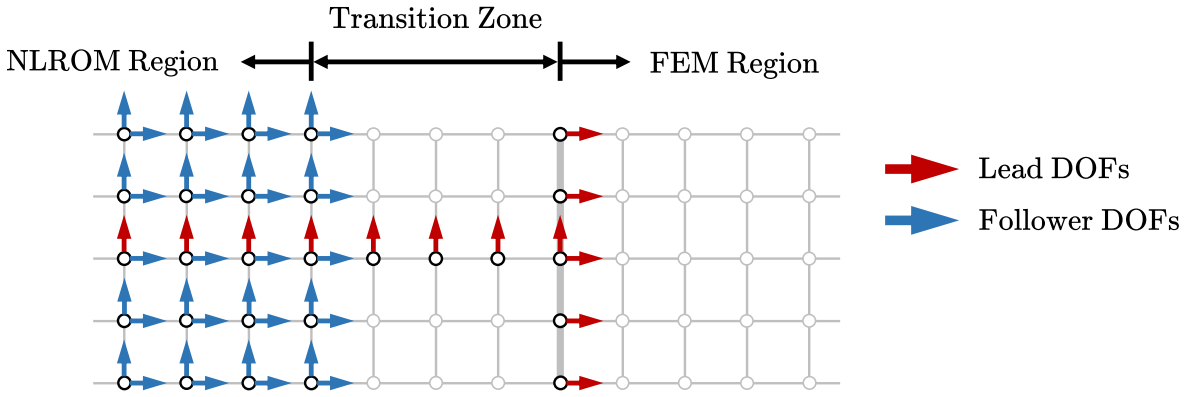

Figure 5.7: DOF classification for substructured model with transition zone

is shown in Fig. 5.2. Because the vertical displacements on the midline and the horizontal displacements on the interface are still a function of $\mathbf{q}$, the elements contacting the midline in the transition zone contribute stiffness to both the $\mathbf{u}_f$ and $\mathbf{q}$ components. When the transition zone is added, the elements are classified as shown in Fig. 5.8.

So, the NLROM restoring force is generated to only replace the $\mathbf{R}_r^{ROM}(\mathbf{\Gamma}_r(\mathbf{q}))$ part of the internal force (the green region in Fig. 5.8). When the test case displacements $(\overline{\mathbf{u}}_m)_p$ from Eq. (5.24) are applied to the lead DOFs, the elements in the transition zone are included in the model. When the parameters of Eq. (5.16) are identified, the elements in the transition region are disregarded, such that only the NLROM region contributes to the internal force.

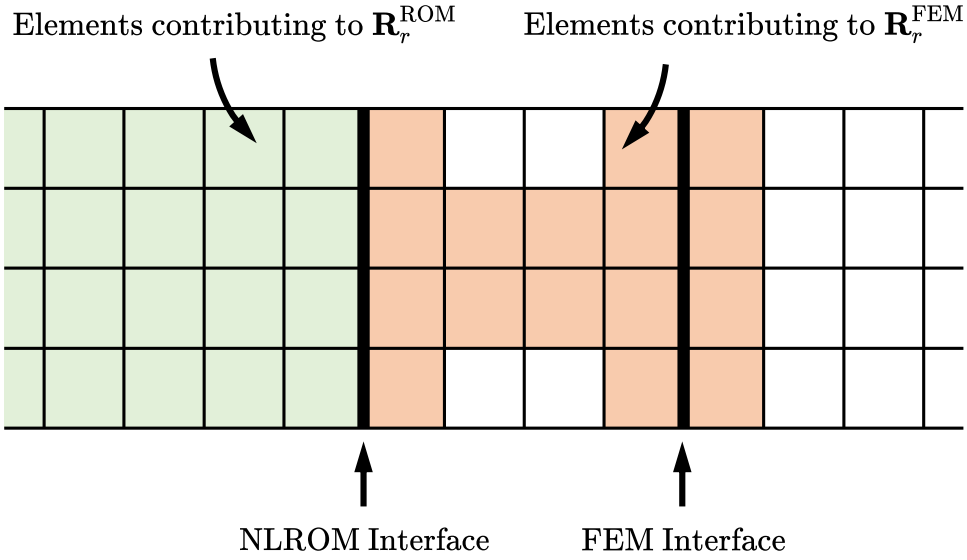

Figure 5.8: Division of elements contributing to $\mathbf{R}_r^{FEM}$ and $\mathbf{R}_r^{ROM}$, with transition

5.2.4 Physical models

This study evaluates three physical beam models, each with a different depth. All three beams have a length $L = 121.92$ cm, a thickness $b = 5.08$ cm, a Young's modulus $E = 9.653$ GPa, and a Poisson's ratio $\nu = 0.35$. The intermediate depth beam (Model A) has a depth of $H_A = 10.16$ cm ($L/H = 12$), the shallow depth beam (Model B) has a depth of $H_B = 5.08$

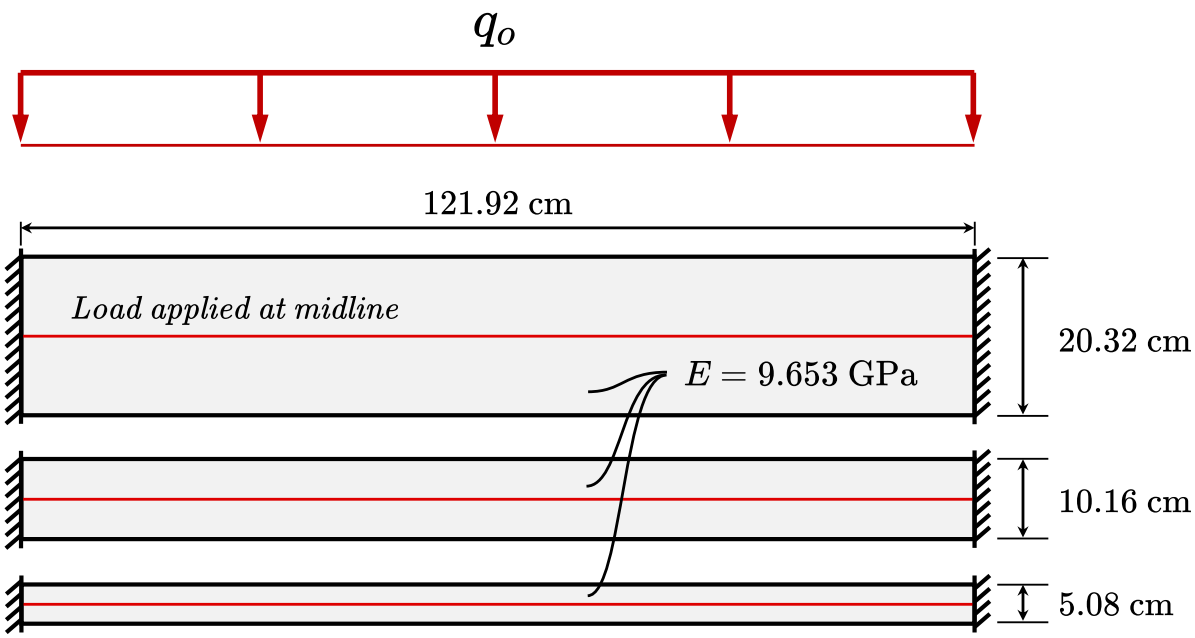

Figure 5.9: Physical parameters of homogeneous beams

cm ($L/H = 24$), and the large depth beam (Model C) has a depth of $H_B = 20.32$ cm ($L/H = 6$). A uniform force per unit length q_o is applied to the midline of the beams. Each beam has a different load intensity, selected to induce a maximum midline displacement of approximately $L/100 \approx 1.22$ cm. The load intensity is 847.0 N/cm for Model A, 116.1 N/cm for Model B, and 5412.1 N/cm for Model C. The physical models are illustrated in Fig. 5.9.

5.2.5 Finite element models

Finite element models were constructed using 9-node Lagrangian plane stress elements following the total Lagrangian formulation in [1]. A Saint Venant-Kirchhoff material model was used.

The beams in Subsection 5.2.4 were each meshed using 0.847 cm-by-0.847 cm square elements. A mesh refinement study was conducted to find a satisfactory element size. The loads were prescribed to the midlines of the beams, and the maximum midline deflection was recorded for several meshes. Reducing the element size from 1.69 cm-by-1.69 cm to 0.847

cm-by-0.847 cm (halving the side length) resulted in a 0.038% increase in midline deflection for Model A, a 0.049% increase for Model B, and a 0.028% increase for Model C.

5.3 Numerical studies

5.3.1 Effect of interface basis selection

Model A, corresponding to the intermediate-depth beam, is used as the primary example problem for the upcoming numerical studies on basis selection and transition zone width. The FEM for Model A (FEM A) is considered the truth model, and the response quantities of the substructured models will be compared with those of the truth model. As a baseline, the stress distributions of FEM A, given the loading defined in Subsection 5.2.4, are displayed in Figs. 5.10-5.12.

Figure 5.10 shows the normal stress in the longitudinal direction (hereinafter "longitudinal stress"). The solution yielded a maximum longitudinal stress of 117.15 MPa in the top element at the support and a minimum longitudinal stress of -112.07 MPa in the bottom element at the support. Unless otherwise specified, the phrase "in the element" will herein refer to the center of the element. All stresses reported in this study refer to stresses queried at the center of the element. In the interface region, defined as the two columns of elements bordering the interface at (undeformed) $X = 91.44$ cm, the maximum absolute value of the

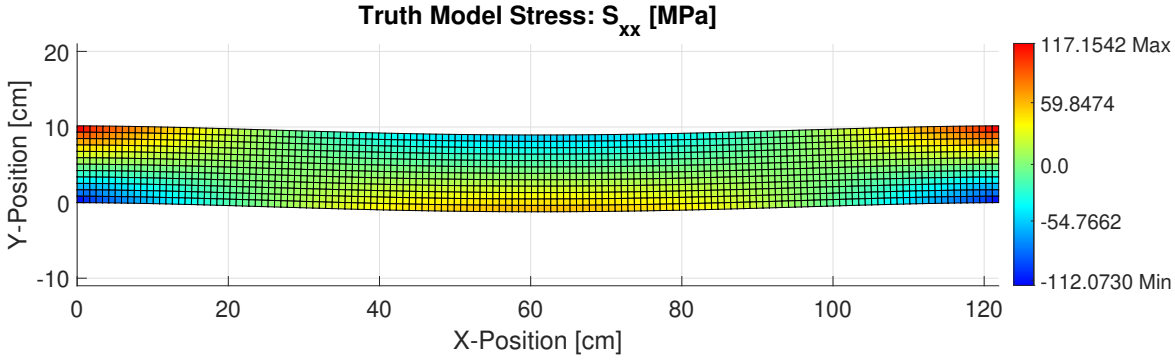

Figure 5.10: Longitudinal stress (S_{xx}) in FEM A, truth model

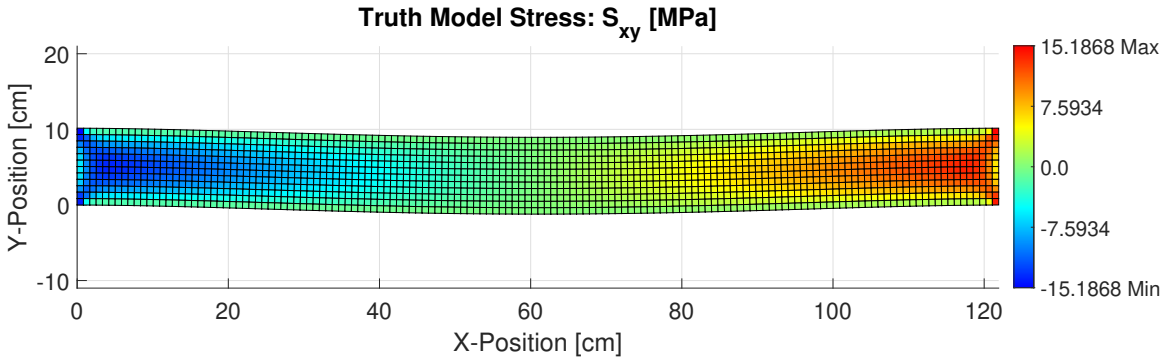

Figure 5.11: Shear stress (S_{xy}) in FEM A, truth model

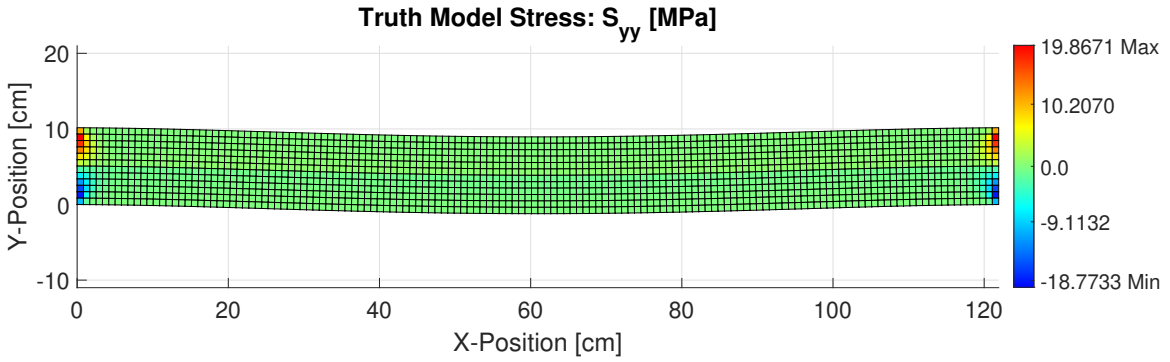

Figure 5.12: Pinching stress (S_{yy}) in FEM A, truth model

longitudinal stress was 17.33 MPa. Figure 5.11 shows the transverse shear stress (hereinafter "shear stress"). The maximum shear stress was 15.19 MPa and occured at the supports. The maximum shear stress in the interface region was 7.45 MPa. Figure 5.12 shows the normal stress in the transverse direction (hereinafter "pinching stress"). In the interface region, the maximum pinching stress was 0.719 MPa, and the minimum pinching stress was -0.745 MPa. These values were relatively constant along the length of the beam.

Interface modes are selected to allow for the best possible approximation of the full-order FEM displacements at the location of the interface, with a reduced number of DOFs. Recall that the the full-order displacements on the interface are related to the modal coordinates

using a linear modal expansion. In order to evaluate the suitability of the Timoshenko versus third-order interface, the FEM response was computed with the displacements of the interface and the midline of the ROM subdomain projected onto each of the modal bases (one for Timoshenko, one for third-order). Note that this is equivalent to using a transition zone that is the full width of the ROM subdomain. This response represents the "best possible" result with the interface and the midline constrained to respond within the provided basis. This allows for the recognition of which errors in the response are caused purely by the choice of modal basis, and it eliminates any potential NLROM parameter identification errors from consideration.

Figures 5.13, 5.15, and 5.17 show the absolute error in the longitudinal stress, shear stress, and pinching stress, respectively, when the Timoshenko constraint is enforced. With all three stress measures, the error was primarily concentrated along the interface. The magnitude of the error was relatively large, especially when compared to the stresses in the truth model in the vicinity of the interface. Figures 5.14, 5.16, and 5.18 show the absolute error in the stresses when the third-order constraint is enforced.

Based on these observations of the stress in the projected model, NLROMs in the ensuing tests will, unless otherwise specified, be generated using a higher-order IM beyond just the uniform and linear IMs.

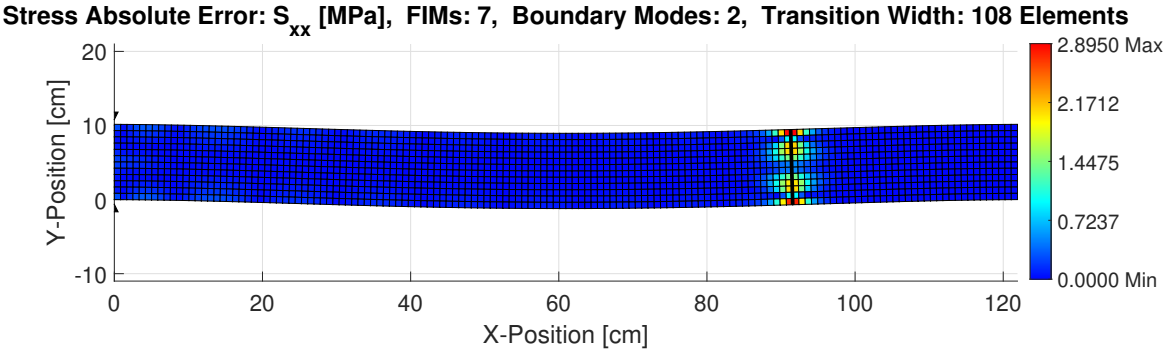

Figure 5.13: Longitudinal stress absolute error of projected FEM with 7 FIMs and Timoshenko interface.

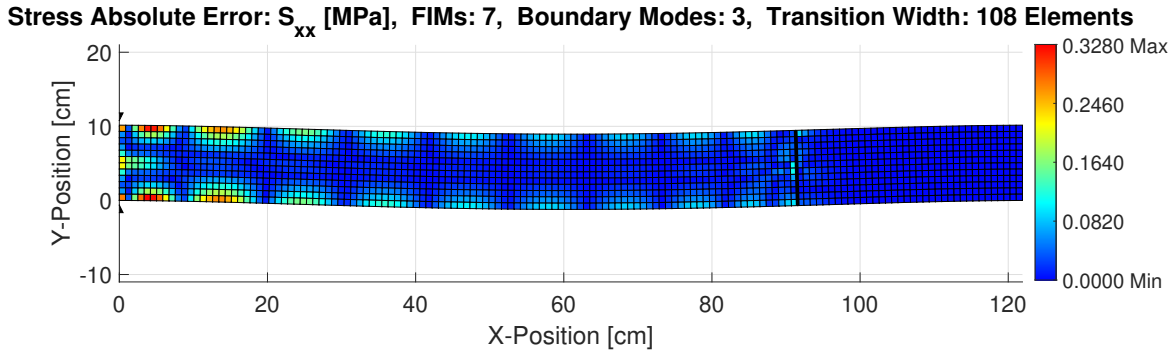

Figure 5.14: Longitudinal stress absolute error of projected FEM with 7 FIMs and third-order interface.

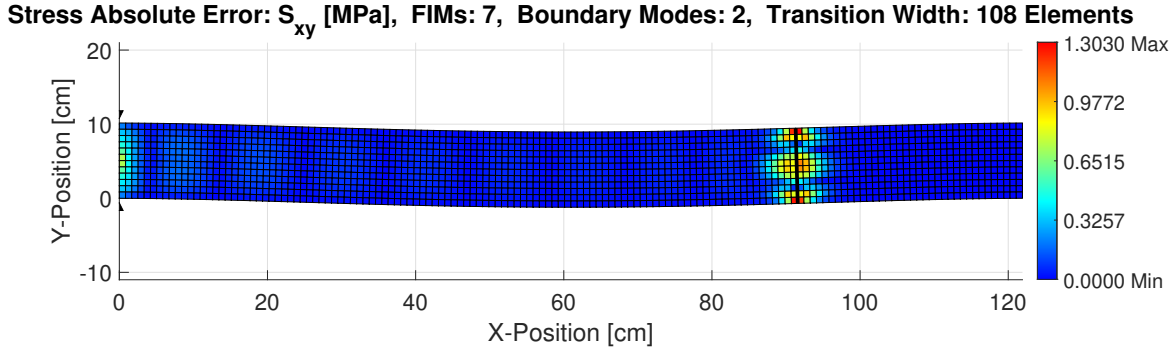

Figure 5.15: Shear stress absolute error of projected FEM with 7 FIMs and Timoshenko interface.

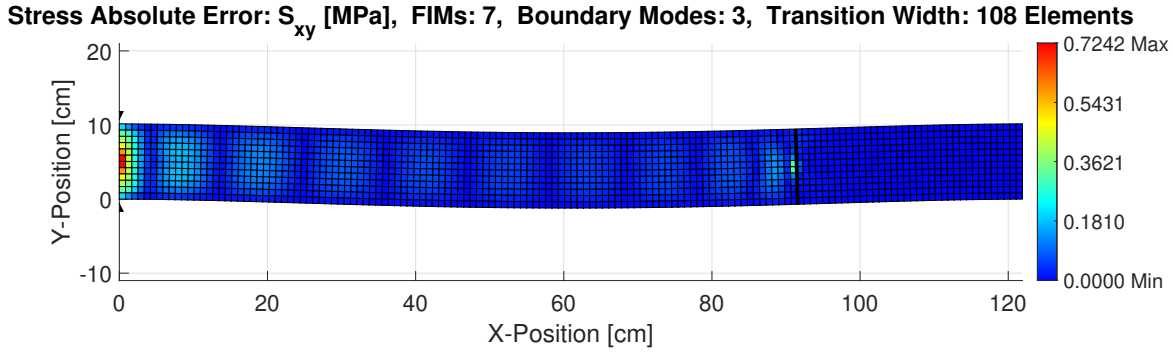

Figure 5.16: Shear stress absolute error of projected FEM with 7 FIMs and third-order interface.

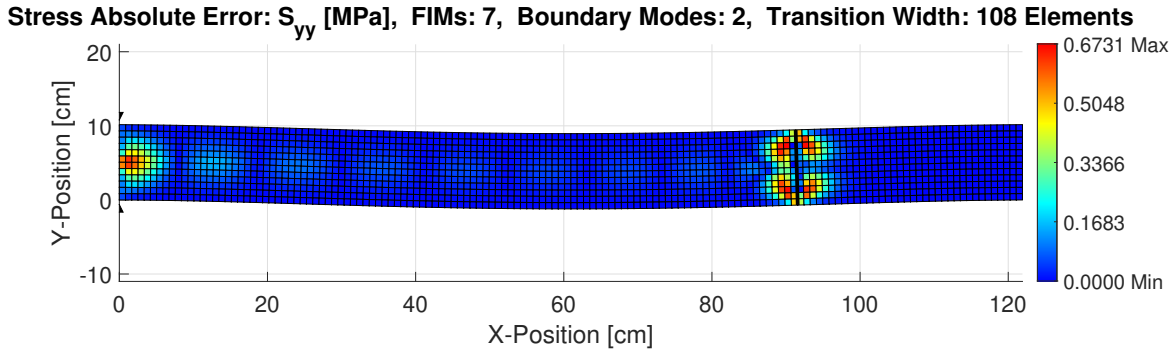

Figure 5.17: Pinching stress absolute error of projected FEM with 7 FIMs and Timoshenko interface.

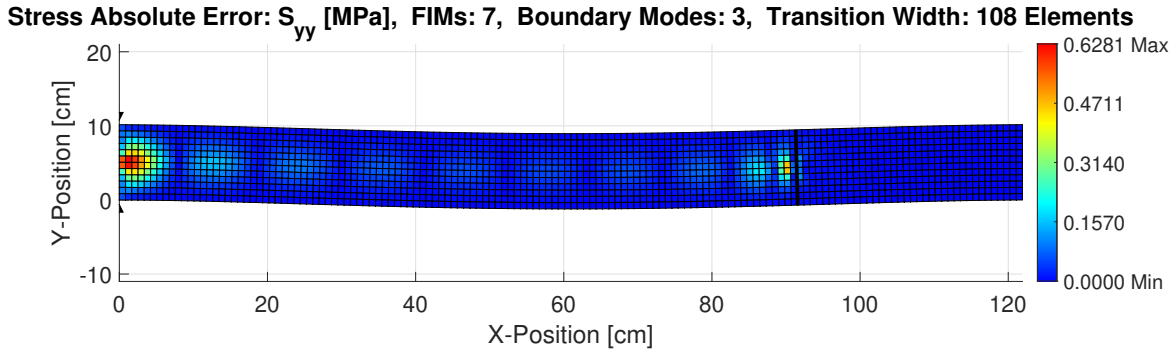

Figure 5.18: Pinching stress absolute error of projected FEM with 7 FIMs and third-order interface.

5.3.2 Substructured model with no transition zone

Substructured models were generated for the intermediate-depth beam using the first 3, 5, and 7 FIMs and interface modes up to and including the cubic mode. These models did not have a transition zone, and so the NLROM subdomain was coupled directly to the FEM subdomain. Testing of the substructured model revealed good matching for both the midline deflection and axial displacement. Figure 5.19 shows the convergence of the midline displacements as the number of FIMs is increased for (a) the transverse deflection and (b) the axial displacement. The error values plotted in Fig. 5.19a are computed as $(v(X) - \overline{v}(X))\,/|v|_{\max}$,

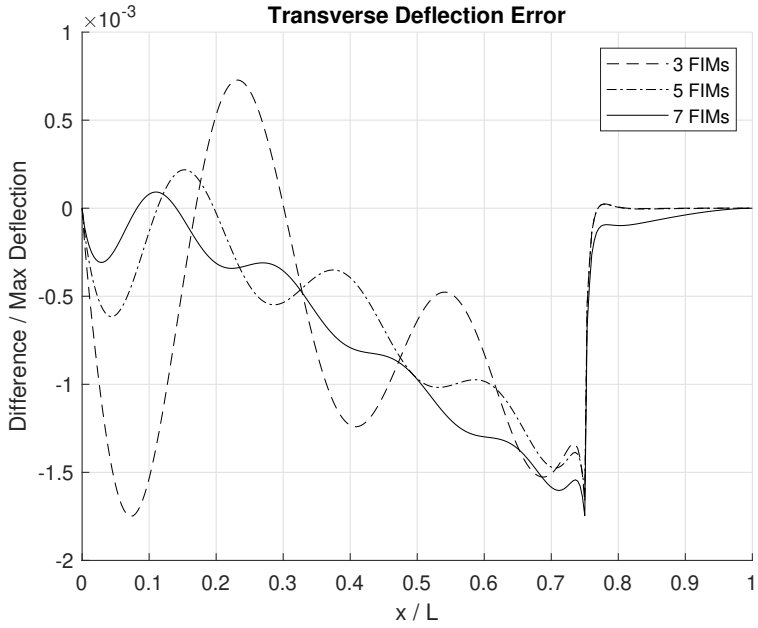

(a) Transverse deflection convergence

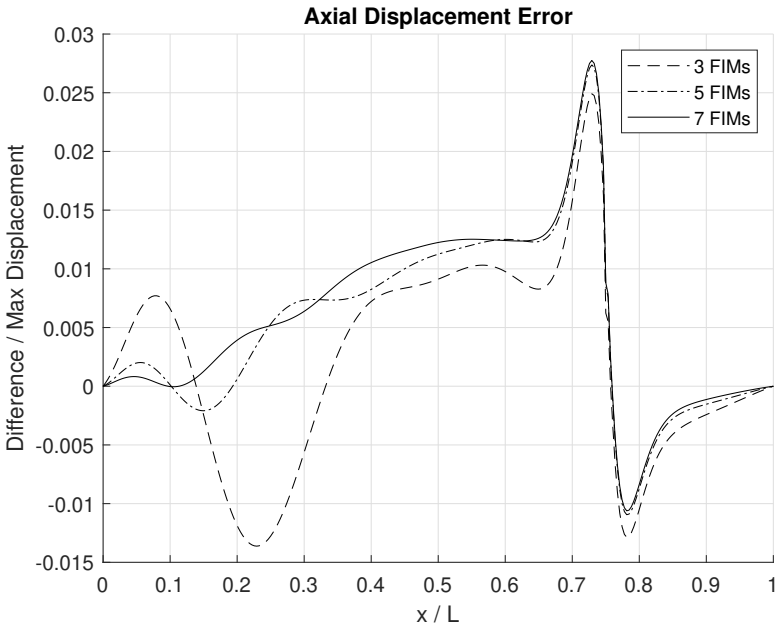

(b) Axial displacement convergence

Figure 5.19: Convergence of transverse and axial displacements with FIM enrichment

where X is the undeformed horizontal position on the midline, $v(X)$ is the midline deflection of the truth model at X (downward positive), $\overline{v}(X)$ is the midline deflection of the substructured model at X (downward positive), and $|v|_{\max}$ is the maximum absolute value of the deflection of the truth model. The error values in Fig. 5.19b are computed in an analogous way for the axial displacements. While increasing the number of FIMs did improve the approximation of the midline displacements primarily in the left half of the beam, there remained an abrupt increase in the error at the interface. Enrichment of the FIM basis did not improve this anomaly, and the midline displacements converged to an erroneous result. The 7 FIM model yielded a 0.17% maximum error in the transverse deflection versus the maximum deflection of the truth model. The same model yielded a 2.77% maximum error in the axial displacement versus the maximum axial displacement of the truth model.

The stresses of the substructured model were investigated to verify that the expansion of the follower displacements provided an acceptable result. Figures 5.20-5.22 show the longitudinal, shear, and pinching stresses of the substructured model with no transition zone. These plots closely resemble the corresponding plots of the truth model in Figs. 5.10-5.12. In this particular case, local anomalies in the stress near the interface are visually discernible in the shear and pinching stress plots, and less so in the longitudinal stress plot.

The plots of the absolute error in the longitudinal, shear, and pinching stress, as shown

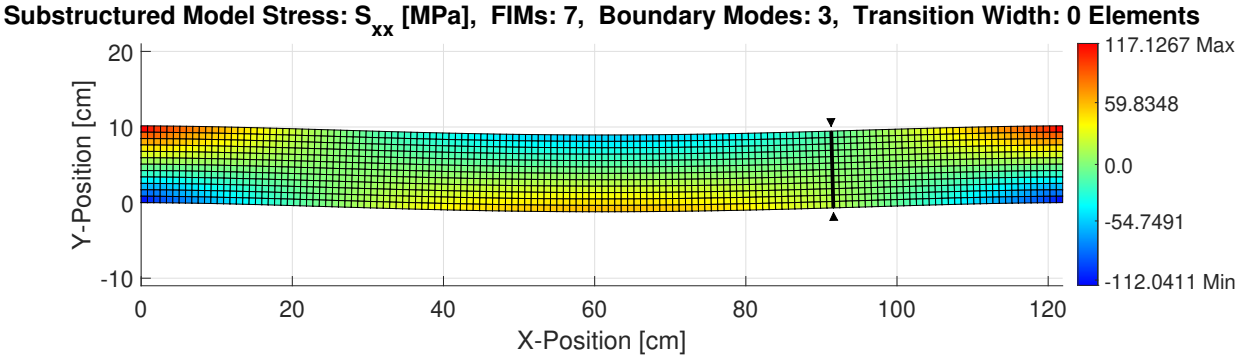

Figure 5.20: Longitudinal stress (S_{xx}) of the substructured model, no transition zone

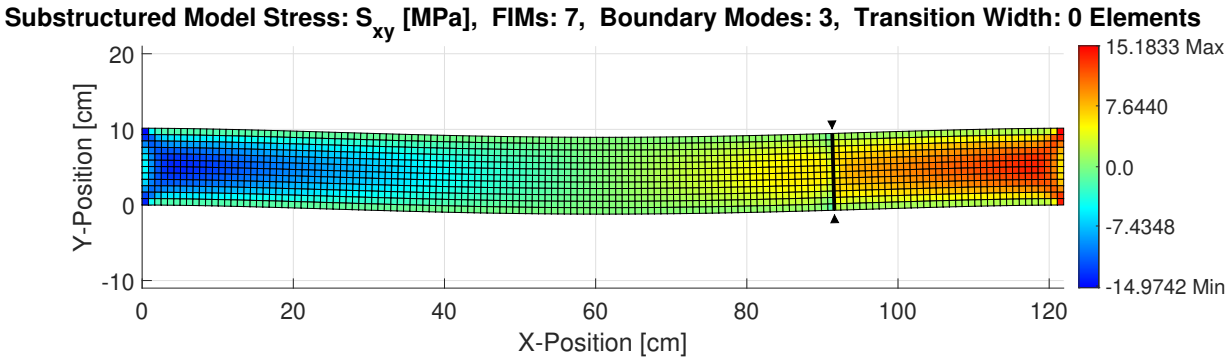

Figure 5.21: Shear stress (S_{xy}) of the substructured model, no transition zone

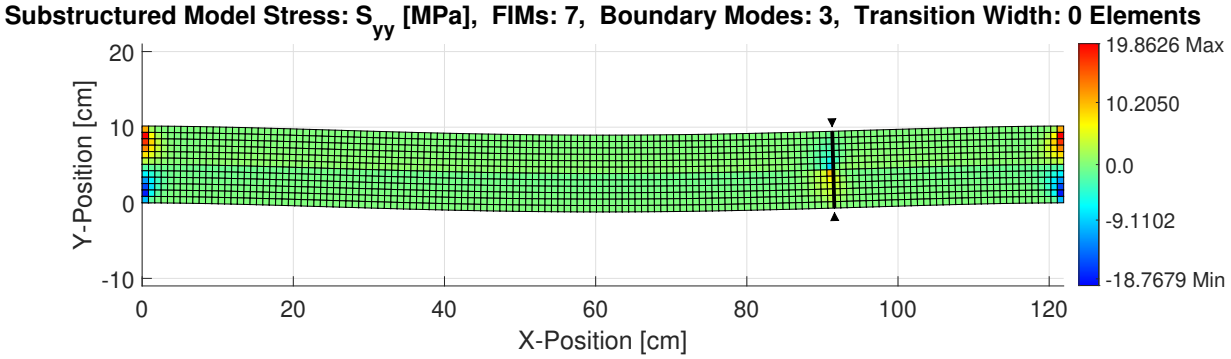

Figure 5.22: Pinching stress (S_{yy}) of the substructured model, no transition zone

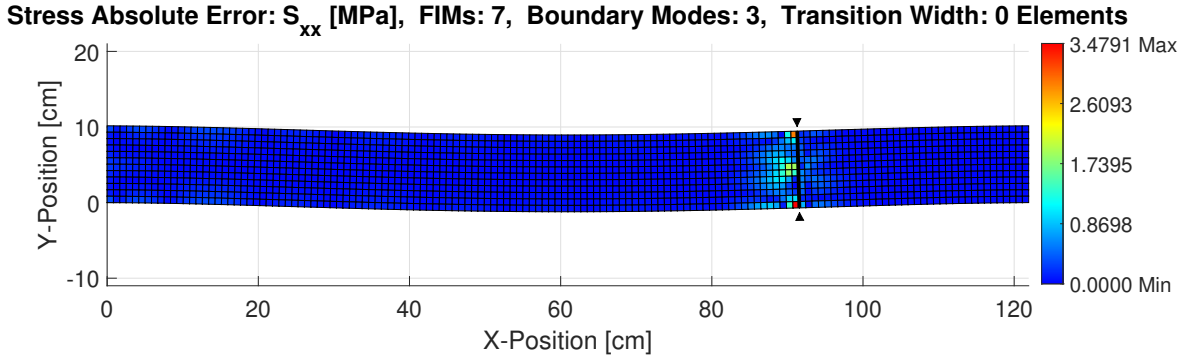

Figure 5.23: Absolute error in longitudinal stress (S_{xx}) of the substructured model

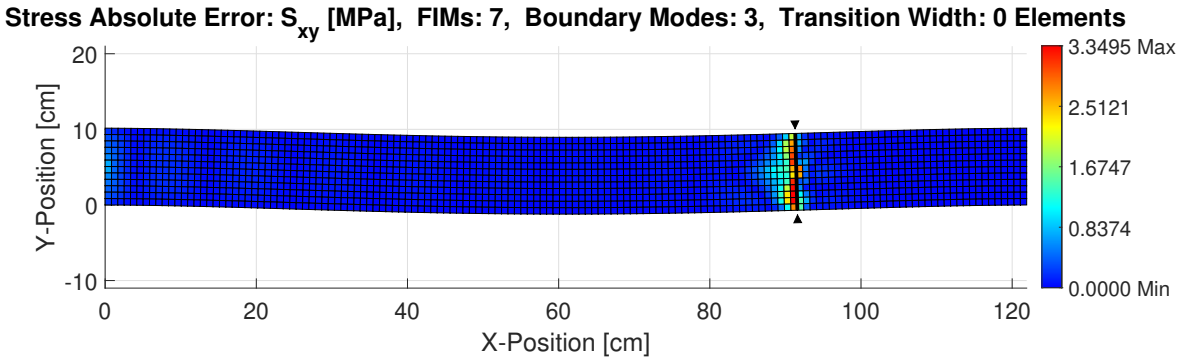

Figure 5.24: Absolute error in shear stress (S_{xy}) of the substructured model

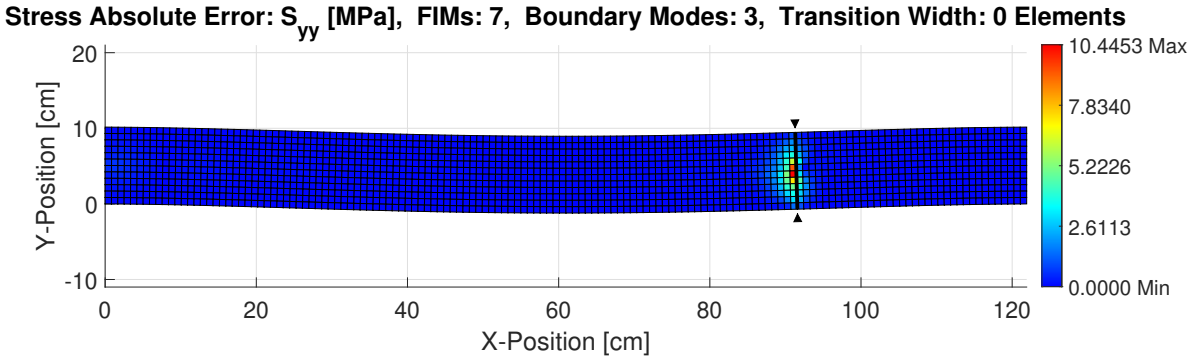

Figure 5.25: Absolute error in pinching stress (S_{yy}) of the substructured model

in Figs. 5.23-5.25, more clearly illustrate the stress anomalies near the interface. In all three cases, the error appears to be more heavily concentrated on the ROM side than the FEM side. The longitudinal stress had a maximum error of 3.48 MPa, located near the extreme bottom fiber at the interface. Though this error is relatively small compared with the maximum longitudinal stress of 117.13 MPa in the beam, the interface is near the location of zero bending moment, and consequently the longitudinal stress error is even larger in comparison with the stresses in the vicinity of the interface. The shear stress had a maximum error of 3.35 MPa, distributed along the interface, versus a maximum shear stress of 15.18 MPa in the beam. The pinching stress had a maximum error of 10.45 MPa near the midline

of the interface versus a maximum pinching stress of 19.86 MPa near the beam supports. The pinching stress error is perhaps the most notable since the pinching stress should be effectively zero in the interior of the beam.

5.3.3 Substructured model with a transition zone

In order to mitigate the stress anomalies on the interface, a transition zone was added between the NLROM subdomain and the FEM subdomain. Recall that Figs. 5.14, 5.16, and 5.18 were generated using a third-order interface and a transition zone that was the entire length of the ROM subdomain. Thus, the response in those figures represents the "best possible" response given the transverse midline and longitudinal interface constraints. In this subsection, the width of the transition zone is increased until the error values (in stress and midline displacement) are acceptably close to those of the model in Figs. 5.14, 5.16, and 5.18. This process is documented in Figs. 5.26-5.28, which show the error in the stress measures as the width of the transition region is increased.

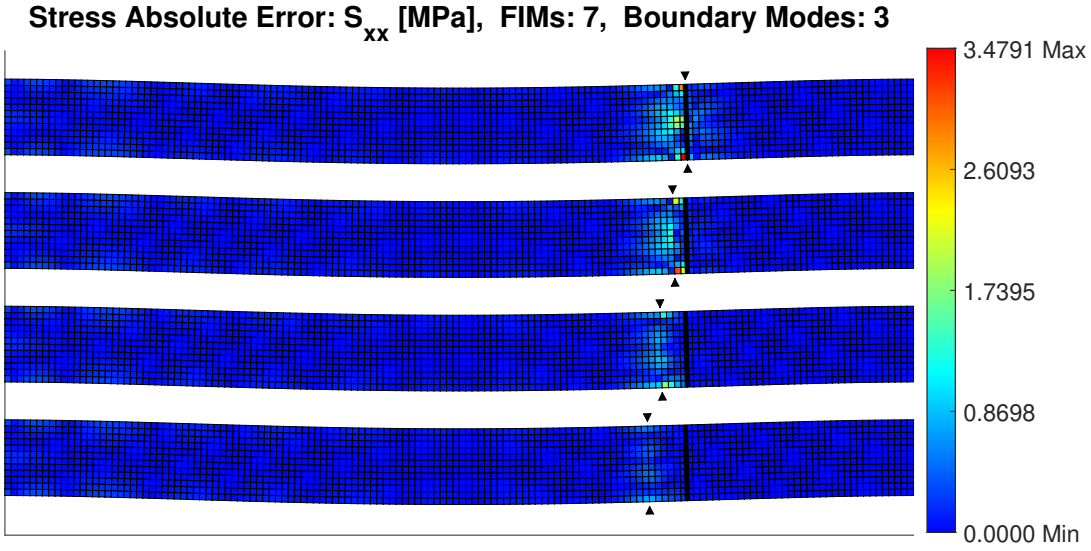

Figure 5.26: Longitudinal stress error, transition widths of 0, 2, 4, and 6 elements (top-to-bottom)

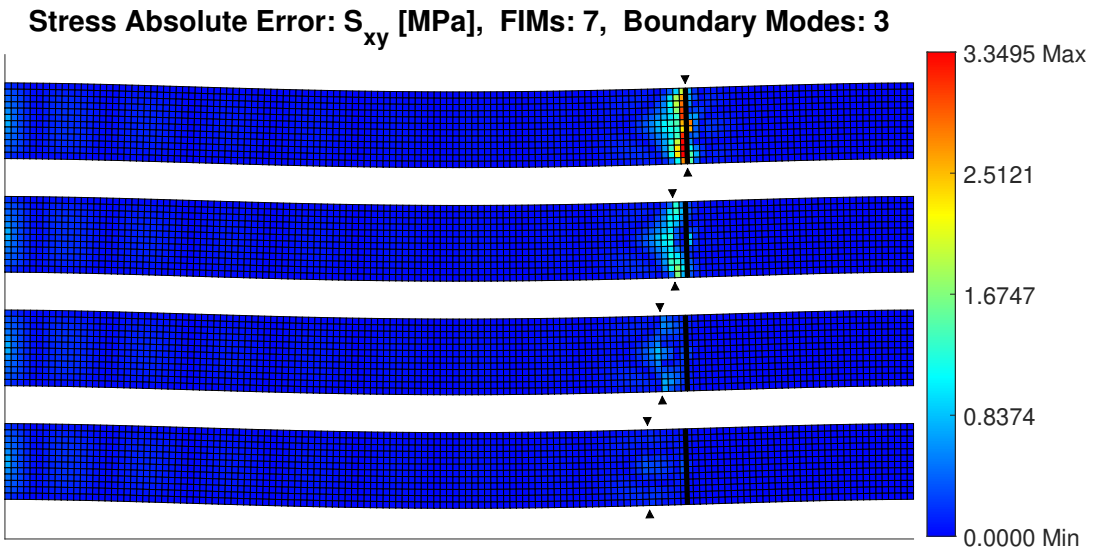

Figure 5.27: Shear stress error, transition widths of 0, 2, 4, and 6 elements (top-to-bottom)

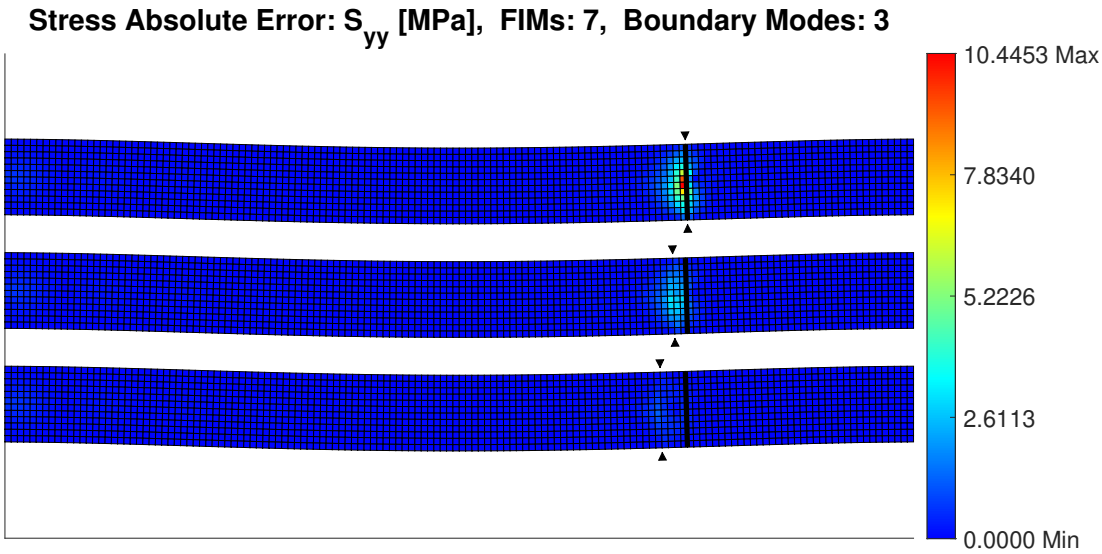

Figure 5.28: Pinching stress error, transition widths of 0, 2, and 4 elements (top-to-bottom)

Different transition widths were tested up to 12 elements (1 beam depth), and a subset of those tests is displayed. On the ROM side of the interface, increasing the width of the transition region from 0 to 6 elements decreased the maximum error in the longitudinal stress from 3.50 MPa to 0.73 MPa, the maximum error in the shear stress from 3.35 MPa to 0.36 MPa, and the maximum error in the pinching stress from 10.44 MPa to 0.44 MPa. Increasing the transition width further to 12 elements decreases the error in the longitudinal stress to 0.11 MPa. The shear and pinching stresses were not significantly affected by this increase.

After studying a range of transition zone widths, it was determined that, for this beam depth, a transition zone width of 12 elements is able to reduce most of the stress anomalies

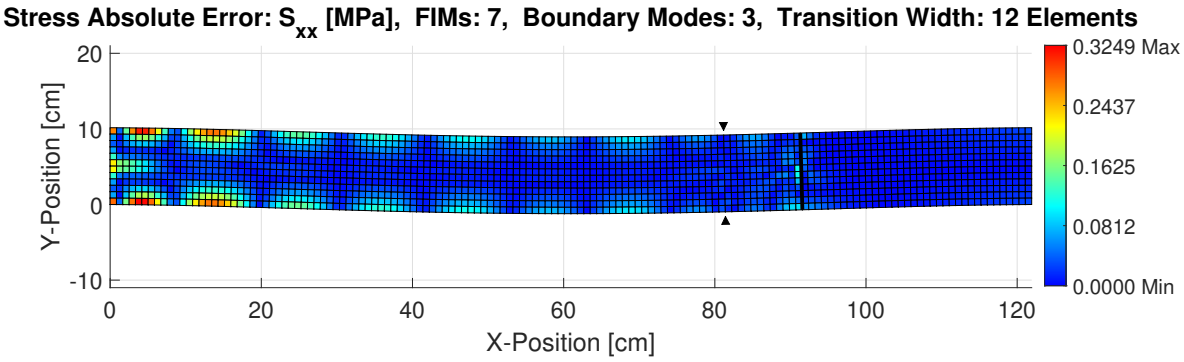

Figure 5.29: Longitudinal stress error in beam with 12-element transition width

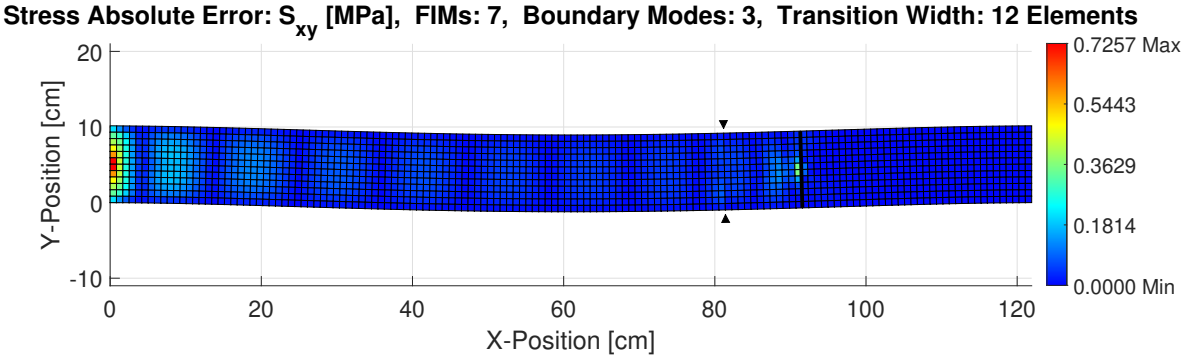

Figure 5.30: Shear stress error in beam with 12-element transition width

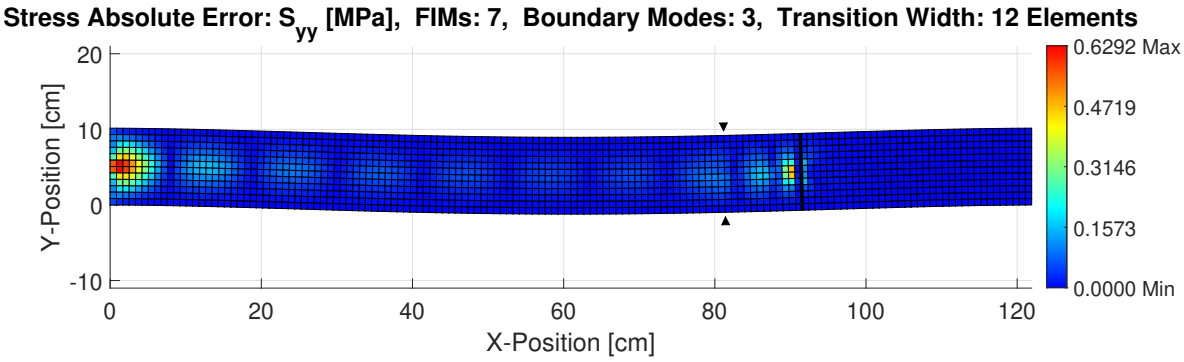

Figure 5.31: Pinching stress error in beam with 12-element transition width

that resulted from the near-interface follower DOF approximation. At a transition width of 12 elements, the stress error is comparable to that of the 7-FIM projected FEM presented in Figs. 5.14, 5.16, and 5.18. Figures 5.29-5.31 show the absolute error in the stresses for a 12-element transition zone width.

The effect of the transition zone width on the midline displacements was also investigated. In Fig. 5.32, the (a) midline deflection and (b) axial displacement error is shown for four transition widths of 0, 2, 6 and 12 elements. The projected FEM with the third-order interface, shown in Fig. 5.14, is also shown as a baseline, as it isolates the error that arises solely from the choice of modal basis for the midline and the interface. The anomalous "spike" in the error at the interface, originally observed in Fig. 5.19, is reduced rapidly as the transition zone width is increased. A transition zone width of 12 elements appears to be sufficient, for both the deflection and axial displacement, to reduce the error enough that the primary contributor to the error is the transverse midline basis.

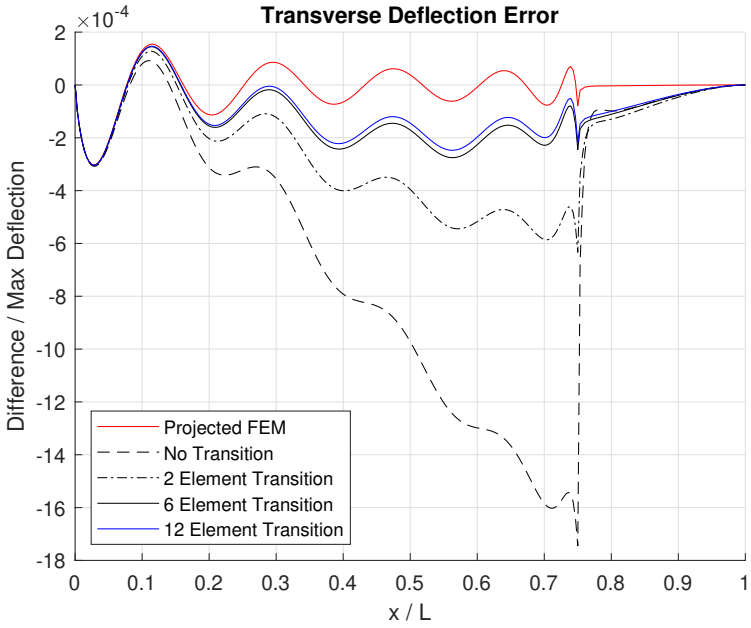

(a) Transverse deflection convergence

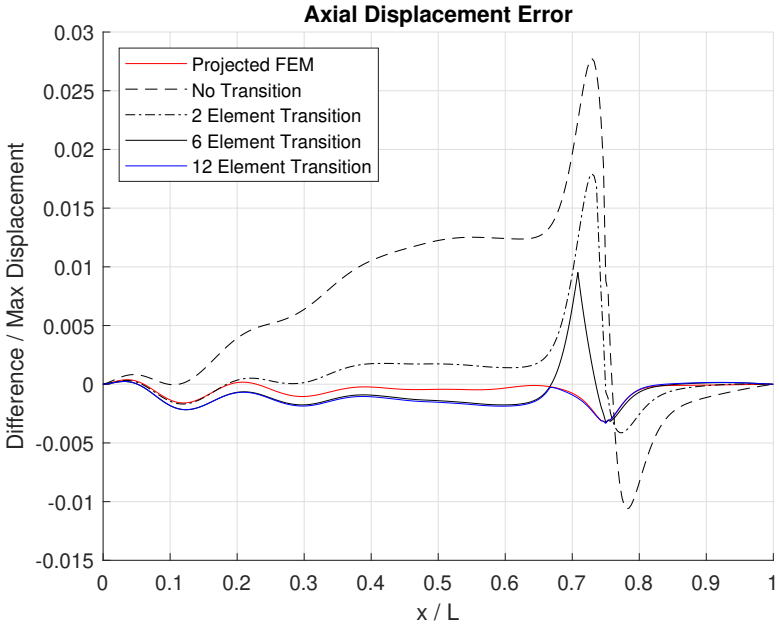

(b) Axial displacement convergence

Figure 5.32: Convergence of transverse and axial displacements with transition width

5.3.4 Multi-layer beam example

As an additional test case, a beam is considered which has a Young's modulus that varies over the height of the cross section. This case study is motivated by composite beams and panels whose physical properties vary over the depth of the structure. The dimensions and properties are identical to to intermediate-depth beam (Model A) studied in the previous sections, except the central 50% of the cross section is a soft core that has a Young's modulus that is half of the value used in the homogeneous Model A. The top and bottom layers, each comprising 25% of the cross section depth, have the same Young's modulus a Model A. The multi-layer model is illustrated in Fig. 5.33.

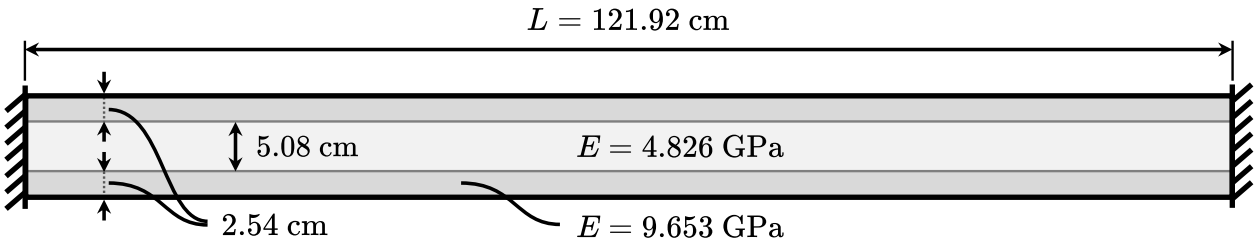

Figure 5.33: Physical parameters for the multi-layer beam

Substructured models were generated for the multi-layer beam using the Timoshenko and third-order IMs, as well as a new set of IMs that includes a shape identified from a static solution of an FEM of the multi-layer beam. This identified set of IMs contains (i) the uniform shape from Fig. 5.4, (ii) the linear shape from Fig. 5.4, and (iii) a higher-order shape

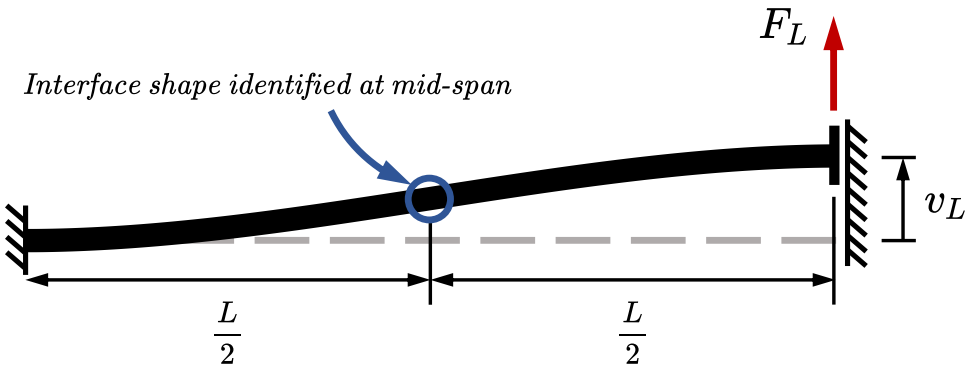

Figure 5.34: Load case for identifying higher-order IM

consisting of the "remaining" longitudinal displacement of a sample cross section (attained during the static solution) after the contributions of (i) and (ii) have been subtracted out. The static solution used to identify this higher-order shape was attained by applying a small transverse displacement to the right end of the beam, while the rotations of both ends are fixed. The longitudinal displacements (global X) of the cross-section at the midpoint of the beam were queried. Note that a linearized FEM solution was attained, so the resulting displacements are proportional to the applied end deflection. Figure 5.34 illustrates the loading and boundary conditions of the aforementioned test problem.

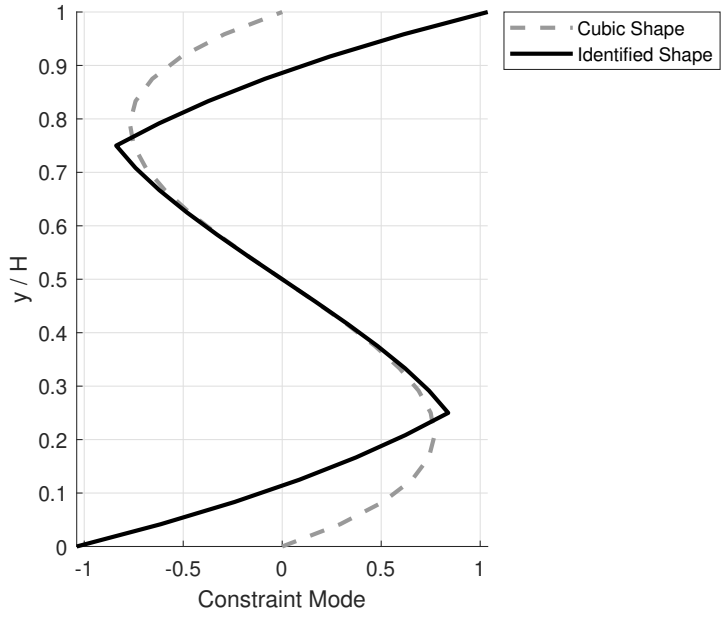

Figure 5.35: Identified IM for multi-layer beam vs. the cubic IM

The global X displacements were queried for all of the nodes in the cross section at mid-span. Let this vector of displacements be $\mathbf{u}_x^{\text{mid}}$. In the load case of Fig. 5.34, this represents the location of zero bending moment. If $\mathbf{\Phi}_{\text{lin}} = [\boldsymbol{\phi}_{\text{const}}, \boldsymbol{\phi}_{\text{lin}}]$ is the matrix containing the constant and linear mode shapes (the Timoshenko interface), then the identified higher-order

shape $\boldsymbol{\phi}_{\text{id}}$ for the multi-layer beam can be computed using the pseudoinverse as

$$\boldsymbol{\phi}_{\text{id}} = \left(\mathbf{I} - \boldsymbol{\Phi}_{\text{lin}}(\boldsymbol{\Phi}_{\text{lin}}^T\boldsymbol{\Phi}_{\text{lin}})^{-1}\boldsymbol{\Phi}_{\text{lin}}^T\right)\,\mathbf{u}_x^{\text{mid}}\,. \tag{5.31}$$

This identified shape was then normalized to yield a slope of -1.0 at the midline with respect to Y, i.e. $d\phi_{\text{id}}(Y)/dY = -1.0$. Recall that $\boldsymbol{\phi}_{\text{id}}$ is a vector, so the slope was computed using the central difference method using the central three nodes at the midline. Figure 5.35 shows the identified shape $\boldsymbol{\phi}_{\text{id}}$, with the aforementioned normalization applied, plotted with the cubic shape used in the homogeneous beams.

The FEM for the multi-layer beam was analyzed using the same load intensity as was used with the homogeneous intermediate-depth beam (Model A). Figures 5.36 and 5.37 show the longitudinal and shear stress, respectively, in the multi-layer beam under these loading conditions. The solution yielded a maximum longitudinal stress of 130.60 MPa in the top element at the support, a 13.45 MPa increase over its homogeneous counterpart. In the interface region, the maximum absolute value of the longitudinal stress was 19.21 MPa. The maximum shear stress was 16.57 MPa and occured at the supports. The maximum shear stress in the interface region was 6.98 MPa.

The substructured models each used a transition zone width of 12 elements, or 1 depth of the beam. It was determined that the error in the shear stress provided the clearest picture

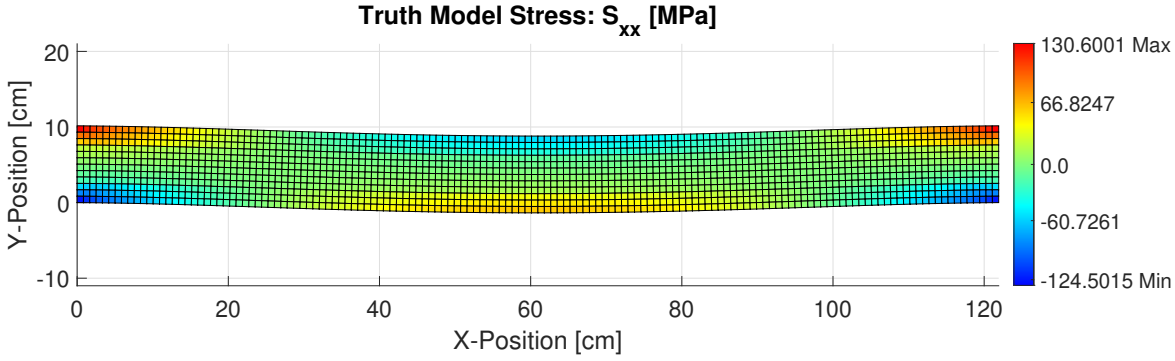

Figure 5.36: Longitudinal stress (S_{xx}) in multi-layer beam, truth model

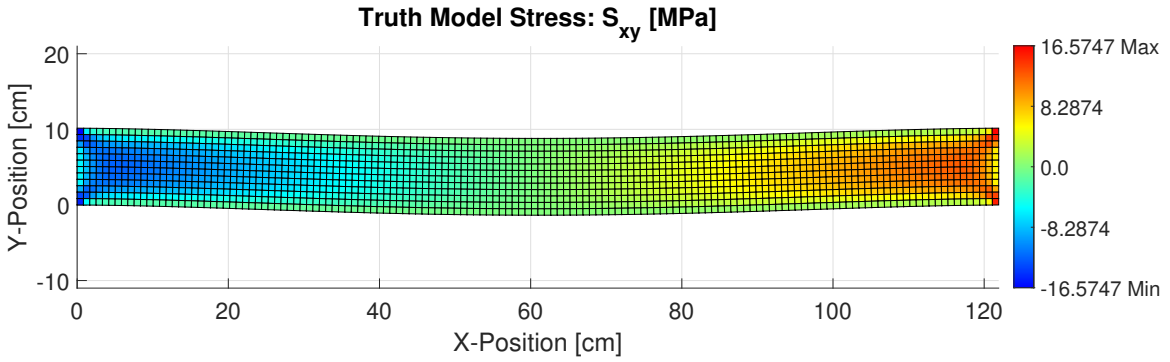

Figure 5.37: Shear stress (S_{xy}) in multi-layer beam, truth model

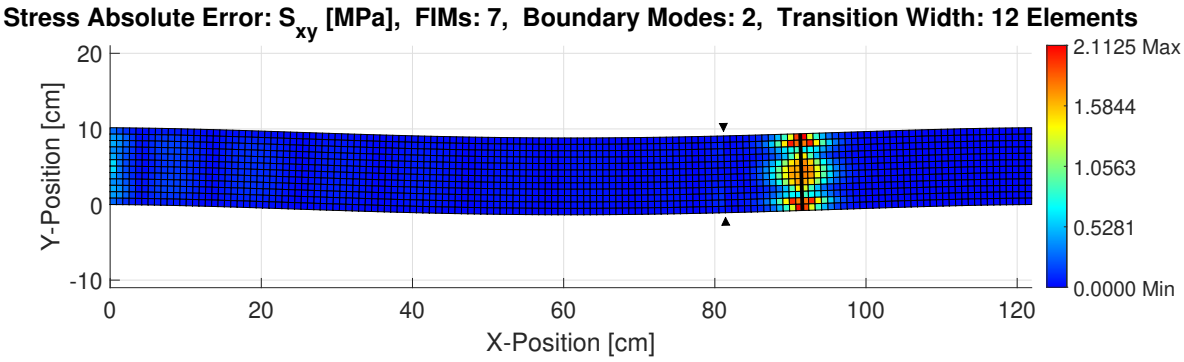

Figure 5.38: Absolute error in shear stress (S_{xy}) in multi-layer beam, Timoshenko interface

of the effects of IM selection on the response. Figures 5.38-5.40 show the absolute error in the shear stress for the Timoshenko interface, third-order interface, and identified interface, respectively.

The Timoshenko interface in Fig. 5.38 yielded large errors in the shear stress on both sides of the interface. The error is distributed along the whole beam depth, but it is largest near the extreme fibers in the stiffer layers. The distribution of the error was similar to how it was in the homogeneous beam in Fig. 5.15, but the max error was larger in proportion to the max shear stress at the interface in the multi-layer beam than it was in the homogeneous beam. In the multi-layer beam, the maximum error was 30.3% of the maximum shear stress at the

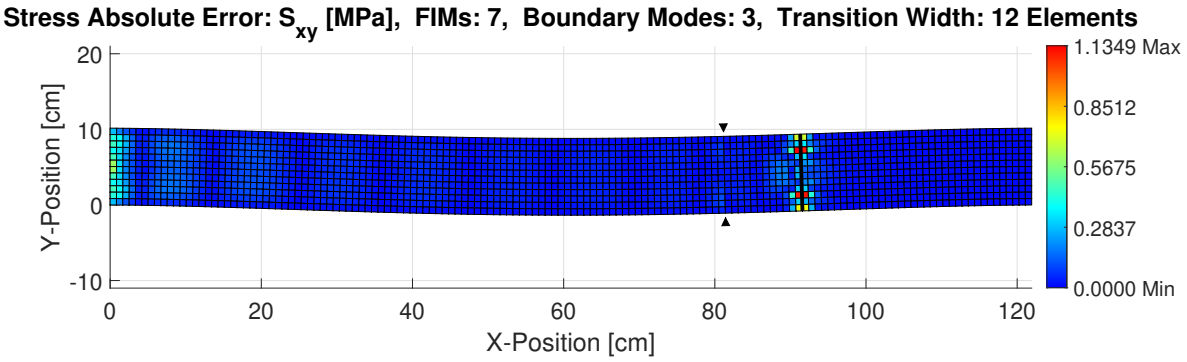

Figure 5.39: Absolute error in shear stress (S_{xy}) in multi-layer beam, third-order interface

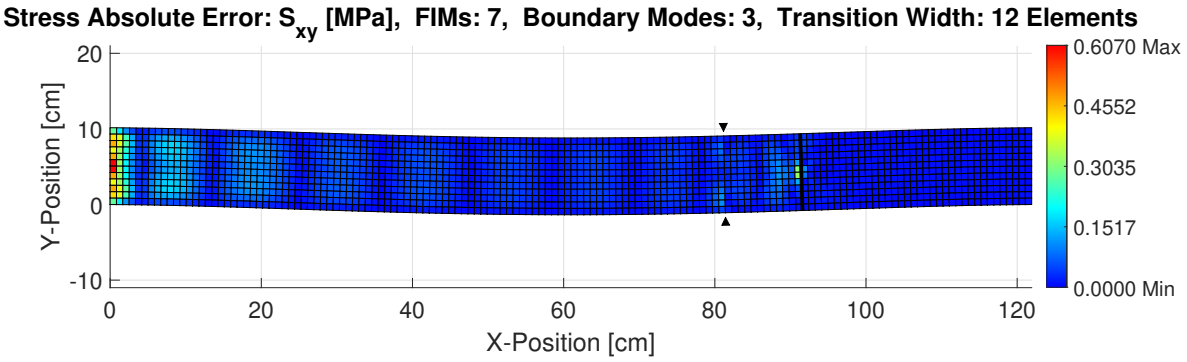

Figure 5.40: Absolute error in shear stress (S_{xy}) in multi-layer beam, identified interface

interface. In the homogeneous beam, the maximum error was only 17.5% of the maximum shear stress at the interface.

The third-order interface in Fig. 5.39 yielded error values that were significantly reduced from those in the Timoshenko case. However, there remained concentrations in the error immediately adjacent to the boundary between the beam layers, on the outer, stiffer side. The maximum error in the shear stress was 16.3% of the maximum shear stress at the interface. The identified interface in Fig. 5.40 yielded error values that were even more significantly reduced. The maximum error in the shear stress at the interface was 4.6% of the maximum shear stress at the interface. This percentage was very similar to that of

the homogeneous beam with a third-order interface. This demonstrates that the selection of over-thickness IMs in composite structures should be motivated by the thickness-varying material properties.

5.4 Conclusions

In this chapter, a plane elasticity FEM was represented by a smaller FEM substructure coupled to an NLROM substructure. The coupling of the substructures was achieved using interface modes intended to capture the characteristic response of the interface. While coupling the NLROM substructure directly to the FEM substructure resulted in good matching of stresses in the FEM substructure, reconstructing the near-interface follower DOFs as a cubic function of the NLROM DOFs generally resulted in spurious stresses on the NLROM side of the interface, especially in the pinching stresses. A transition zone was added between the FEM and NLROM substructures in order to mitigate this issue. It was determined that a transition zone of approximately one beam depth was sufficient to reduce the near-interface stress errors to acceptable levels. When a multi-layer beam with a thickness-varying Young's modulus was modeled, the third-order interface shape that had been used successfully with the homogeneous beam resulted in heightened stress errors near the interface. In response to this observation, a higher-order interface shape was identified from a single static solution of the multi-layer beam FEM. The NLROM of the multi-layer beam was then constructed using this identified shape in place of the third-order interface mode, significantly decreasing the stress errors in the validation.

Chapter 6

SUMMARY AND FUTURE WORK

6.1 Guided reduced-order models

In Chapter 2, the governing equation of a shallow von Kármán beam was derived, and a Galerkin method was used to generate an approximate form of the equilibrium equation in terms of matrix and vector parameters. While these parameters can be derived analytically using the physical properties and dimensions of the beam, a new approach was proposed by which the parameters were identified from an FEM of the equivalent structure. The full identification of the parameters was achieved using two static equilibrium configurations of the FEM. The first of these configurations is the undeformed configuration, for which the transverse displacements and rotations are zero. The second configuration is that which results from an axial displacement being applied to one of the end nodes of the beam FEM, with the remaining axial DOFs being unrestrained and the transverse displacement and rotation DOFs being restrained to zero. In each of these two configurations, the tangent stiffness matrix and external force vector are queried from the FEM, and the parameters of the governing equation are computed. This identification approach was validated using models with no initial curvature, which showed high-quality fitting with the FEM used for the identification.

In Chapter 3, a least-squares identification procedure for the GROM parameters was introduced and evaluated. The least-squares procedure allows for the inclusion of additional base configurations in the training data and thus is conducive to a higher-quality fit for beams with large initial curvatures. Even when generated with test cases generated about the undeformed configuration, the GROM showed much more predictable post-snap-through response, as compared with an NLROM generated using the same training data.

6.2 Curved beam identification

In Chapter 3, problems with the identification of NLROMs of curved beams were diagnosed and solved. It was first demonstrated that the large-deformation response of the NLROM was highly sensitive to changes in the test cases, when such test cases were centered about the undeformed configuration. In beams with moderate initial curvature, the snapped configuration was not able to be captured by the NLROMs identified in this way.

A cubic Taylor expansion of the restoring force of the FEM representing the curved beam, with respect to the nodal displacements, was computed. The cubic expansion was insufficient to accurately capture the snapped state for initial curve heights as small as $L/50$. For initial curve heights slightly less than $L/30$, and larger, a snapped state was not predicted by the Taylor expansion. This failure to adequately capture the snapped state demonstrated that the cubic expansion of the restoring force of the FEM of a moderately curved beam was not sufficient to capture the snapped response and that higher-order terms would be necessary. A 4-element FEM representing a beam with a curve height of $L/36$ was then generated. In order to assess the contribution from higher-order terms, Taylor expansions of the restoring force up to 5th-order were generated for the 4-element FEM, and the SEPs were computed for each expansion order. With the 4th-order expansion, the second limit point in the SEP was recaptured (after being absent from the 3rd-order expansion), though the SEP still had significant error beyond the first limit point. With the 5th-order expansion, the snapped state was accurately captured. From this investigation it was concluded that a cubic NLROM for a moderately curved beam would need to consider training data in configurations other than the undeformed configuration.

The DBIC approach, where the transverse displacements are prescribed while the rotations and axial displacements are left unrestrained, was successful at identifying ROMs of curved beams using a transverse-only basis. The fit quality of ROMs for curved beams was able to be significantly improved by adding base configurations in the large deformation regime to enrich the training data. The improvement was greater for the NLROMs than it

was for the GROMs. The fit quality was evaluated at individual configurations along the SEP by comparing the projected internal force of the ROM to that of the corresponding FEM in an equivalent configuration. An error metric was proposed based on this difference in projected restoring force. The error was shown to be smaller in the vicinity of the base configurations used to enrich the training data. The greatest improvement in the fit quality of the snap-through response was attained by adding one additional base configuration (besides the undeformed configuration) near the snapped configuration. Minor additional improvements to the were able to be made by adding base configurations in the mid-snap-through region (beyond just the undeformed and snapped configurations), but a qualitative assessment of the SEP fit-quality was not significantly changed. It is recommended that the training data set contain at least one unsnapped base configuration (near the undeformed configuration), and at least one snapped configuration.

6.3 Substructuring of plane-elasticity finite element models

In Chapter 4, NLROMs were constructed for part of a planar beam modeled with 2D plane stress finite elements. The plane stress FEM used to represent the beam was divided into two substructures—one to be represented by an NLROM and one to be represented by an FEM. The behavior of the interface between the NLROM and FEM substructures was described using interface modes, which capture the characteristic response of the interface. The modal DOFs governing the interface modes were directly included in the NLROM restoring force. For the homogeneous beams, uniform, linear, and cubic interface modes were considered. Truncating the interface basis after the linear mode (resembling a Timoshenko assumption) resulted in notable stress errors on the interface. When the substructured models were analyzed under static loading, the transverse midline displacements had good matching with the truth model. The slave displacements had good matching with the corresponding displacements of the truth model over most of the NLROM subdomain, but stress anomalies were observed near the interface, even when including the cubic interface mode.

A transition zone was introduced to the substructured model to mitigate the issues that

arose from disregarding the coupling between the slave DOFs in the NLROM substructure and the full order DOFs in the FEM substructure. Adding the transition zone significantly reduced the near-interface stress errors. For the homogeneous beam models studied, a transition zone width of one beam depth was sufficient to reduce the stress errors to an acceptable level.

A substructured model was also generated for a multi-layer beam with thickness-varying material properties. Using a transition zone width of one beam depth and a third-order interface, the displacements and stresses matched well with the truth model, but concentrations in the shear stress error were observed on the interface. An interface mode was then identified from a single static solution of the multi-layer beam FEM, and this identified mode was used instead of the cubic mode in the third-order interface. Using the identified mode instead of the cubic mode reduced the stress error on the interface to levels similar to those observed in the case of the homogeneous beam with the third-order interface.

6.4 Future work

In the process of doctoral research, questions naturally arise that cannot be fully investigated during the degree program. The research comprising this dissertation has given rise to several notable topics of future study.

- The restoring force function of the GROM presented in Chapters 2 and 3 takes its form from a statically-condensed shallow von Kármán beam. This form provides the advantage over an NLROM of having fewer independent parameters for the same number of modes. Furthermore, the GROM parameters can be identified using only two static solutions of an FEM. This idea may be extensible to shallow shells, which are used extensively in aerospace structures. An efficient identification procedure for shells, similar to that demonstrated in Chapter 2 for shallow beams, would prove valuable due to the decreased computational burden in identifying the model parameters.

- It was observed in Chapter 4 that a transition zone width of approximately one beam

depth reduced the near-interface stress errors to acceptable levels. The transition zone width is selected so that the slave DOFs that are retained in the NLROM substructure are insensitive to changes in the full-order DOFs in the FEM subdomain. It would be informative to construct an NLROM for the plane stress beam without the interface modes and then to determine the required transition zone width. Presumably the required transition zone would be wider without the interface modes, and the required width could be determined with further study.

- Because the interface in Chapter 4 was described using a linear modal expansion in the global X-direction and not a true rotation of the cross section, the NLROMs were not equipped for finite rotations. If a rotation angle were to be included as one of the NLROM DOFs, a similar substructured system which handles finite rotations could be generated. This can likely be accomplished with minimal modification to the Chapter 4 theory. A finite rotation model could be of more use in a cantilevered application.

BIBLIOGRAPHY

[1] T. Belytschko, W.K. Liu, B. Moran, and K.I. Elkhodary. *Nonlinear Finite Elements for Continua and Structures*. Wiley, 2nd edition, January 2014.

[2] Y.-W. Chang, X.Q. Wang, E. Capiez-Lernout, M.P. Mignolet, and C. Soize. Reduced order modelling for the nonlinear geometric response of some curved structures. In *International Forum on Aeroelasticity and Structural Dynamics, IFASD 2011*, pages 1–19, Paris, France, June 2011.

[3] R. Courant and D. Hilbert. *Methods of Mathematical Physics, Vol 1*. Wiley, 1989.

[4] R.R. Craig and M.C.C. Bampton. Coupling of substructures for dynamic analyses. *AIAA Journal*, 6(7):1313–1319, 1968.

[5] R.W. Gordon and J.J. Hollkamp. Reduced-order modeling of random response of curved beams using implicit condensation. In *47th AIAA/ASME/ASCE/AHS/ASC Structures, Structural Dynamics, and Materials Conference*, AIAA-2006-1926, Newport, Rhode Island, May 2006.

[6] R.W. Gordon and J.J. Hollkamp. Reduced-order models for acoustic response prediction. Technical Report AFRL-RB-WP-TR-2011-3040, Air Force Research Laboratory, July 2011.

[7] X. Guo, Y.-Y Lee, and C. Mei. Non-linear random response of laminated composite shallow shells using finite element modal method. *International Journal for Numerical Methods in Engineering*, 67(10):1467–1489, 2006.

[8] X. Guo, A. Przekop, and C. Mei. Nonlinear random response of shallow shells at elevated temperatures using finite element modal method. In *45th AIAA/ASME/ASCE/AHS/ASC Structures, Structural Dynamics and Materials Conference*, AIAA-2004-1558, Palm Springs, California, April 2004.

[9] A.M.A. van der Heijden. *W.T. Koiter's Elastic Stability of Solids and Structures*. Cambridge University Press, 2008.

[10] J.J. Hollkamp and R.W. Gordon. Modeling membrane displacements in the sonic fatigue response prediction problem. In *46th AIAA/ASME/ASCE/AHS/ASC Structures,*

Structural Dynamics and Materials Conference, AIAA-2005-2095, Austin, Texas, April 2005.

[11] J.J. Hollkamp and R.W. Gordon. Reduced-order models for nonlinear response prediction: Implicit condensation and expansion. *Journal of Sound and Vibration*, 318(4):1139–1153, 2008.

[12] J.J. Hollkamp, R.W. Gordon, and S.M. Spottswood. Nonlinear modal models for sonic fatigue response prediction: a comparison of methods. *Journal of Sound and Vibration*, 284(3):1145–1163, 2005.

[13] J.J. Hollkamp and P.J. O'Hara. Modeling damage within a reduced-order model framework: An application. In *54th AIAA/ASME/ASCE/AHS/ASC Structures, Structural Dynamics, and Materials Conference*, AIAA-2013-1518, Boston, Massachusetts, April 2013.

[14] S. Jain, P. Tiso, J.B. Rutzmoser, and D.J. Rixen. A quadratic manifold for model order reduction of nonlinear structural dynamics. *Computers and Structures*, 188:80–94, 2017.

[15] K. Kim, A.G. Radu, X.Q. Wang, and M.P. Mignolet. Nonlinear reduced order modeling of isotropic and functionally graded plates. *International Journal of Non-Linear Mechanics*, 49:100–110, 2013.

[16] D. Krattiger, L. Wu, M. Zacharczuk, M. Buck, R.J. Kuether, M.S. Allen, P. Tiso, and M.R.W. Brake. Interface reduction for hurty/craig-bampton substructured models: Review and improvements. *Mechanical Systems and Signal Processing*, 114:579–603, 2019.

[17] R.J. Kuether and M.S. Allen. Craig-bampton substructuring for geometrically nonlinear subcomponents. In *Dynamics of Coupled Structures, Volume 1*, pages 167–178. Springer International Publishing, 2014.

[18] R.J. Kuether and M.S. Allen. Substructuring with nonlinear reduced order models and interface reduction with characteristic constraint modes. In *55th AIAA/ASME/ASCE/AHS/ASC Structures, Structural Dynamics, and Materials Conference*, AIAA-2014-1518, National Harbor, Maryland, January 2014.

[19] R.J. Kuether, M.S. Allen, and J.J. Hollkamp. Modal substructuring of geometrically nonlinear finite-element models. *AIAA Journal*, 54(2):691–702, 2016.

[20] R.J. Kuether, M.S. Allen, and J.J. Hollkamp. Modal substructuring of geometrically nonlinear finite element models with interface reduction. *AIAA Journal*, 55(5):1695–1706, 2017.

[21] T.-N. Le, J.-M. Battini, and M. Hjiaj. Efficient formulation for dynamics of corotational 2d beams. *Computational Mechanics*, 48(2):153–161, 2011.

[22] J. Lee. Large-Amplitude Plate Vibration in an Elevated Thermal Environment. *Applied Mechanics Reviews*, 46(11S):S242–S254, 1993.

[23] R. Lewandowski. Application of the ritz method to the analysis of non-linear free vibrations of beams. *Journal of Sound and Vibration*, 114(1):91–101, 1987.

[24] M.I. McEwan, J.R. Wright, J.E. Cooper, and A.Y.T. Leung. A combined modal/finite element analysis technique for the dynamic response of a non-linear beam to harmonic excitation. *Journal of Sound and Vibration*, 243(4):601–624, 2001.

[25] C. Mei, J.M. Dhainaut, B. Duan, S.M. Spottswood, and H.F. Wolfe. Nonlinear random response of composite panels in an elevated thermal environment. Technical Report AFRL-VA-WP-TR-2000-3049, Air Force Research Laboratory, October 2000.

[26] M.P. Mignolet, A. Przekop, S.A. Rizzi, and S.M. Spottswood. A review of indirect/non-intrusive reduced order modeling of nonlinear geometric structures. *Journal of Sound and Vibration*, 332(10):2437–2460, 2013.

[27] M.P. Mignolet and C. Soize. Stochastic reduced order models for uncertain geometrically nonlinear dynamical systems. *Computer Methods in Applied Mechanics and Engineering*, 197(45):3951–3963, 2008.

[28] A.A. Muravyov and S.A. Rizzi. Determination of nonlinear stiffness with application to random vibration of geometrically nonlinear structures. *Computers and Structures*, 81(15):1513–1523, 2003.

[29] M. Nash. *Nonlinear Structural Dynamics by Finite Element Modal Synthesis*. PhD thesis, Imperial College, The University of London, September 1977.

[30] P.J. O'Hara and J.J. Hollkamp. A coupled approach for modeling damage within a reduced-order model framework. In *54th AIAA/ASME/ASCE/AHS/ASC Structures, Structural Dynamics, and Materials Conference*, AIAA-2013-1517, Boston, Massachusetts, April 2013.

[31] P.J. O'Hara and J.J. Hollkamp. Modeling crack propagation within a reduced- order model framework. In *55th AIAA/ASME/ASCE/AHS/ASC Structures, Structural Dynamics, and Materials Conference*, AIAA-2014-0150, National Harbor, Maryland, January 2014.

[32] P.J. O'Hara and J.J. Hollkamp. Modeling vibratory damage with reduced-order models and the generalized finite element method. *Journal of Sound and Vibration*, 333(24):6637–6650, 2014.

[33] H. Parandvar and M. Farid. Nonlinear reduced order modeling of functionally graded plates subjected to random load in thermal environment. *Composite Structures*, 126:174–183, 2015.

[34] R.A. Perez, X.Q. Wang, and M.P. Mignolet. Nonintrusive structural dynamic reduced order modeling for large deformations: Enhancements for complex structures. *Journal of Computational and Nonlinear Dynamics*, 9(3):031008, 2014.

[35] R.A. Perez, X.Q. Wang, and M.P. Mignolet. Prediction of displacement and stress fields of a notched panel with geometric nonlinearity by reduced order modeling. *Journal of Sound and Vibration*, 333(24):6572–6589, 2014.

[36] A. Przekop, M.S. Azzouz, X. Guo, C. Mei, and L. Azrar. Finite element multiple-mode approach to nonlinear free vibrations of shallow shells. *AIAA Journal*, 42(11):2373–2381, 2004.

[37] A. Przekop and S.A. Rizzi. Nonlinear reduced order random response analysis of structures with shallow curvature. *AIAA Journal*, 44(8):1767–1778, 2006.

[38] A. Przekop and S.A. Rizzi. Dynamic snap-through of thin-walled structures by a reduced-order method. *AIAA Journal*, 45(10):2510–2519, 2007.

[39] E. Riks. An incremental approach to the solution of snapping and buckling problems. *International Journal of Solids and Structures*, 15(7):529–551, 1979.

[40] J.B. Rutzmoser, D.J. Rixen, P. Tiso, and S. Jain. Generalization of quadratic manifolds for reduced order modeling of nonlinear structural dynamics. *Computers and Structures*, 192:196–209, 2017.

[41] J.M. Seawright, R. Wiebe, and R.A. Perez. Guided identification of nonlinear reduced-order models via the incorporation of von Kármán beam theory. *International Journal of Non-Linear Mechanics*, 150:104348, 2023.

[42] Y. Shi and C. Mei. A finite element time domain modal formulation for large amplitude free vibrations of beams and plates. *Journal of Sound and Vibration*, 193(2):453–464, 1996.

[43] S.M. Spottswood, J.J. Hollkamp, and T.G. Eason. Reduced-order models for a shallow curved beam under combined loading. *AIAA Journal*, 48(1):47–55, 2010.

[44] S.M. Spottswood, B.P. Smarslok, R.A. Perez, T.J. Beberniss, B.J. Hagen, Z.B. Riley, K.R. Brouwer, and D.A. Ehrhardt. Supersonic aerothermoelastic experiments of aerospace structures. *AIAA Journal*, 59(12):5029–5048, 2021.

[45] R. Vaicaitis. Time domain approach for nonlinear response and sonic fatigue of NASP thermal protection systems. In *32nd Structures, Structural Dynamics, and Materials Conference*, AIAA-91-1177-CP, Baltimore, Maryland, April 1991.

[46] C.I. Van Damme, M.S. Allen, and J.J. Hollkamp. Evaluating reduced order models of curved beams for random response prediction using static equilibrium paths. *Journal of Sound and Vibration*, 468:115018, 2020.

[47] C.I. Van Damme, A. Madrid, M.S. Allen, and J.J. Hollkamp. Simultaneous regression and selection in nonlinear modal model identification. *Vibration*, 4(1):232–247, 2021.

[48] A. Vizzaccaro, A. Givois, P. Longobardi, Y. Shen, J.-F. Deü, L. Salles, C. Touzé, and O. Thomas. Non-intrusive reduced order modelling for the dynamics of geometrically nonlinear flat structures using three-dimensional finite elements. *Computational Mechanics*, 66(6):1293–1319, 2020.

[49] X.Q. Wang, V. Khanna, K. Kim, and M.P. Mignolet. Nonlinear reduced-order modeling of flat cantilevered structures: Identification challenges and remedies. *Journal of Aerospace Engineering*, 34(6):04021085, 2021.

[50] X.Q. Wang, M.P. Mignolet, T.G. Eason, and S.M. Spottswood. Nonlinear reduced order modeling of curved beams: A comparison of methods. In *50th AIAA/ASME/ASCE/AHS/ASC Structures, Structural Dynamics, and Materials Conference*, AIAA-2009-2433, Palm Springs, California, May 2009.

[51] X.Q. Wang, P.J. O'Hara, M.P. Mignolet, and J.J. Hollkamp. Reduced order modeling with local enrichment for the nonlinear geometric response of a cracked panel. *AIAA Journal*, 57(1):421–436, 2019.

[52] X.Q. Wang, G.P. Phlipot, R.A. Perez, and M.P. Mignolet. Locally enhanced reduced order modeling for the nonlinear geometric response of structures with defects. *International Journal of Non-Linear Mechanics*, 101:1–7, 2018.

[53] R. Wiebe and L.N. Virgin. On the experimental identification of unstable static equilibria. *Proceedings of the Royal Society A: Mathematical, Physical and Engineering Sciences*, 472(2190):20160172, 2016.